A NACELLE DESIGN METHOD FOR TURBOFAN ENGINES

An Aerodynamic Perspective

M.M. Otting
Master Flight Performance and Propulsion,
Faculty of Aerospace Engineering

August 18, 2020

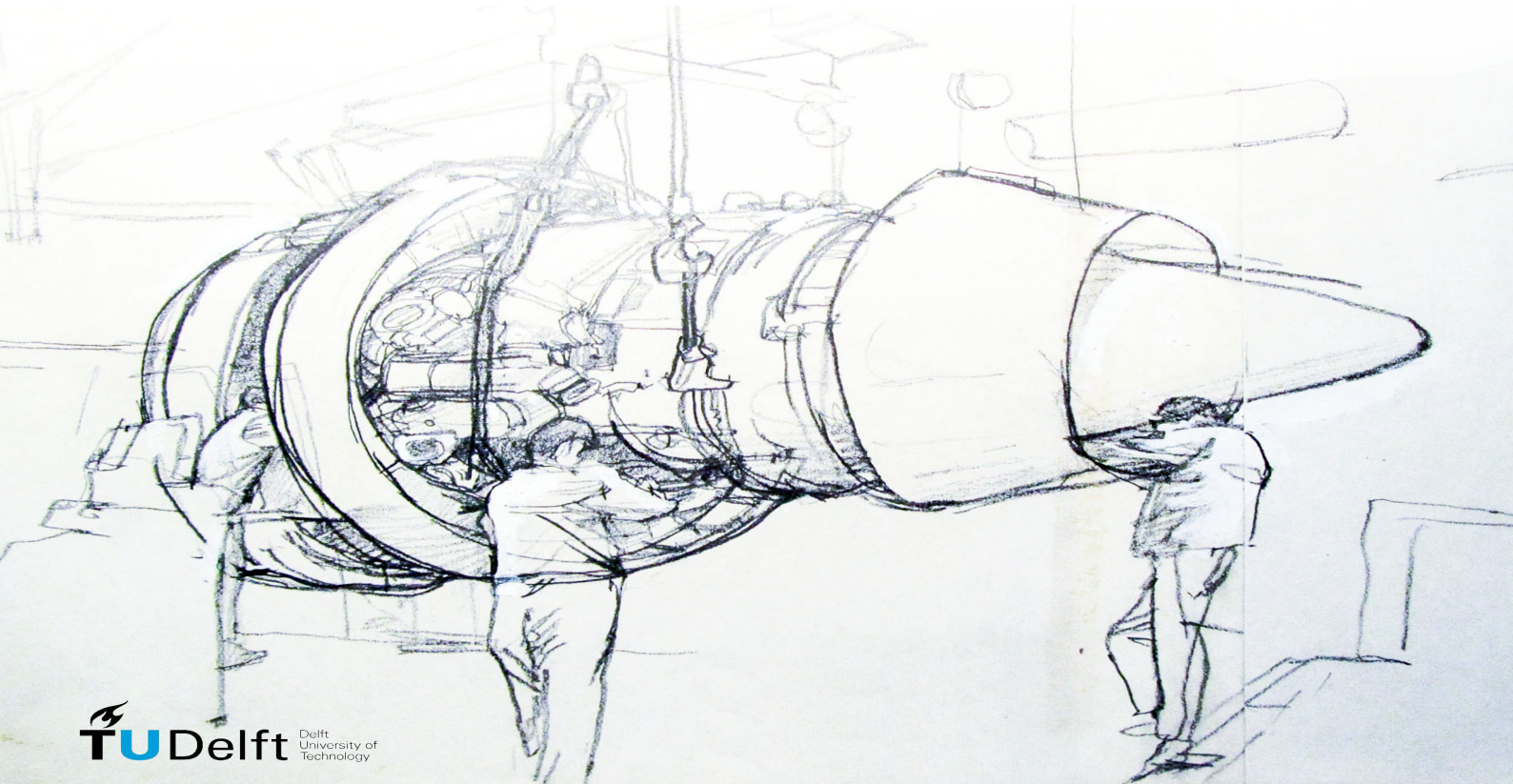

TU Delft Delft University of Technology

A NACELLE DESIGN METHOD FOR TURBOFAN ENGINES

An Aerodynamic Perspective
Master thesis

M.M. Otting

In fulfilment of the requirements
for the degree of

Master of Science
Aerospace Engineering,
Flight Performance and Propulsion

at the Delft University of Technology

To be defended publicly on
Tuesday September 8, 2020 at 1:00 PM

August 18, 2020

Maria Magdalena Otting
Student number: 4276027

Thesis committee, Supervisor
Flight Performance and Propulsion
Dr. Ir. R. Vos

Thesis committee
Aerodynamics
Dr. R.P. Dwight

Thesis committee
Flight Performance and Propulsion
Dr. Arvind G. Rao

PREFACE

This master thesis is part of the graduation project for the Master Aerospace Engineering at the Technical University of Delft. I have always liked drawing and giving shape to new objects. It is something that I recognise in the conceptual design process. The opportunity to start from scratch and to see a design taking shape is something enjoyable. It was therefore without reservation that I chose for the master Track Flight Performance and Propulsion. The project's subject, to develop a new aerodynamic nacelle design method for turbofans, lies directly within the areas of expertise of my master. It allows me to learn more about aerodynamics in the conceptual design and to use it in practice. The topic remained difficult but challenging, as it tries to develop something new. I hope that this research and the upcoming thesis will be of use to others when they are designing their engines.

This report contains the master thesis graduation project which is divided into four phases: research on existing theory, defining the design method, model development and results analysis. The focus of this report is on the last three project phases. The first phase has been discussed in a previous literature review. Chapter 2 summarises the relevant terminology from this literature review. A summary of the method is included in Chapter 3. Readers who are particularly interested in the results can find this in Chapter 6 of the report.

I would like to thank my supervisor, Roelof Vos, for giving me the opportunity to work on this project. It has occurred more than once that I had to change the planning and the deliverables due to my recurring health problems but I'm grateful for the understanding and support you kept showing me.

M.M. OTTING

Delft, Netherlands
August 18, 2020

SUMMARY

The aerodynamic nacelle design is often not analysed with extensive CFD until the last project stages. This limits the changes that can be made to the nacelle contour. A preliminary design method using CFD is developed in this report to counter this problem. A nacelle contour is created with several polynomials. The contour is restricted by multiple linear and non-linear constraints to meet the safety, engine, structural and internal spacing requirements. The contour is optimised with respect to two objectives: the net propulsive force in cruise ($M = 0.8, h = 10670m$) and the net propulsive force in take-off. The take-off condition was varied in several cases to determine the influence of the off-design point on the nacelle geometry. The multi-objective NSGA-II algorithm is used to search for the optimum nacelle geometries on the Pareto front. This gives the designer more freedom and insight into the nacelle contour.

Furthermore, the CFD analysis is limited to a 2D axisymmetric Euler analysis on a structured grid to reduce computational time. The viscous drag is computed separately from an empirical equation using the dynamic pressure at the wall from the CFD analysis. Every case analysed 700 nacelle geometries within 2 days. The case for the hot and high take-off condition showed the largest improvement in the cruise objectives compared to the sea-level take-off condition with Mach number 0.1 or 0.2. However, this case converged to a local Pareto front. The other two take-off conditions might give better results if the program runs longer. The last case analysed a long-ducted nacelle. This case is limited to free-mixer configurations as the effect of the mixing flow on the thrust cannot be analysed in an inviscid solver. The improvement in net propulsive force in take-off and cruise is similar to the optimised short-ducted nacelle.

The resulting geometries were as expected from the literature study. Lowering the MFR and $\frac{a}{b}$ and increasing the CR would create a rounder lip and improve the take-off conditions. The opposite occurred to optimise the cruise condition. The influence of the nozzle variables is harder to estimate as they are interdependent. A larger and more forward maximum diameter was observed for very short fan cowls. This reduced the shock's strength over the fan cowl. The core cowl was flattened by reducing the offset and boattail angle to lower the shock strength over the core cowl. However, an unchoked convergent-divergent bypass duct increased the net propulsive force even more. The lower exhaust velocity decreases the shock's strength and pressure drag to the extent that it overcame the loss in gross thrust. A convergent-divergent duct also improved take-off performance. Although, this was accompanied by a large and steep core cowl to reduce the pressure drag in take-off whereas this would increase the pressure drag in cruise.

CONTENTS

LIST OF FIGURES

LIST OF TABLES

ACRONYMS

CD	Convergent-Divergent
CFD	Computational Fluid Dynamics
CST	Class-Shape Transformation
EA	Evolution Algorithms
FAR	Federal Aviation Regulations
GA	Genetic Algorithm
ICAO	International Civil Aviation Organization
ISA	International Standard Atmosphere
LPT	Low Pressure Turbine
NSGA	Nondominated Sorting Genetic Algorithm
SFC	Specific Fuel Consumption
UHB	Ultra High Bypass engines

SYMBOLS

Greek symbols

α	Wall angle	$^\circ$
β	Boattail angle	$^\circ$
β_{cr}	Crossover spread factor	–
β_m	Mutation spread factor	–
ϵ_{crit}	Critical nozzle pressure ratio	–
η	Efficiency	–
η_{n}	Isentropic nozzle expansion efficiency	–
η_m	Mutation distribution index	–
η_{cr}	Crossover distribution index	–
γ	Specific heat ratio	–
μ	Dynamic viscosity	$\frac{kg}{ms}$
ϕ	Fluid force vectors	N
ϕ_i	Maximum inlet inclination angle	$^\circ$
ρ	Density	$\frac{kg}{m^3}$
θ	Cone angle	$^\circ$

Symbols

$\dot{m}$	Mass flow	$\frac{kg}{s}$
A	Area	m^2
a	Ellipse semi-major axis	m
b	Ellipse semi-minor axis	m
BPR	Bypass ratio	–
C_{p}	Specific heat coefficient	$\frac{kJ}{kgK}$
C_D	Drag or Discharge coefficient	–
C_t	Thrust coefficient	–
C_v	Velocity coefficient	–
C_a	Angularity loss coefficient	$\frac{kJ}{kgK}$
C_F	Skin friction coefficient	–
C_p	Pressure coefficient	–
CR	Contraction ratio	–
D	Drag or diameter	*N or m*
F_{G}	Gross thrust	N
FF	Form factor	–
FPR	Fan pressure ratio	–
G	Number of generations	–
h	Altitude	m
L	Length	m
l/d	Slenderness ratio	–
M	Mach number	–
MFR	Mass flow ratio	–
N	Population size	–
n	Super-ellipse exponent	–
n_x	Normal vector	–
NPF	Net propulsive force	N
NPR	Nozzle pressure ratio	–
P_{i}	Point of inflection	–
P_{s}	Static pressure	Pa
P_{t}	Total pressure	Pa
PR	Pressure ratio	–
q	Dynamic pressure	Pa
R	Universal gas constant or radius	– or m
Re	Reynolds number	–
S_{wet}	External wetted area	m^2
T	Thrust	N
t	Thickness	m
T_{s}	Static temperature	K
T_{t}	Total temperature	K
u	Axial velocity component	$\frac{m}{s}$
V	Velocity	$\frac{m}{s}$
x	Horizontal coordinates	m
y	Vertical coordinates	m

Subscripts

∞	Freestream
AB	afterbody
b	bypass

c	Core
CB	centerbody
cc	Core cowl
clr	clearance
corr	Corrected
CR	Cruise
crit	critical
diff	Diffuser
eng	Core Engine
ex	Exit
exi	Exit inner
exo	Exit outer
f	Fan
fc	Fan cowl
HL	Highlight
init	Initial
int	Intrinsic
max	Maximum
mxd	Mixed
nac	Nacelle
p	Plug
TH	Throat
ti	Turbine inner
tm	Turbine mount
TO	Take-off
to	Turbine outer

1 INTRODUCTION

This master thesis is a part of the graduation project for the master Aerospace Engineering at the Technical University of Delft. The purpose of this report is to develop a quick preliminary aerodynamic turbofan nacelle design method. This chapter introduces the subject and problems faced in this expertise and will summarise the approach and research questions used during this project.

1.1 Problem Statement

The nacelle is a development that people often overlook when discussing an engine. It fulfils many functions, not in the least protecting the engine from outside hazards and the aircraft structure from most engine failures. Its aerodynamically designed contour guides the flow into the engine and the excess air around the engine and wing with the least drag. The nacelle is, therefore, prepared for a specific engine and aircraft. An example is the ALF502 turbofan engine [2]. This engine has been used on both the Bombardier CL-600 and the BAe 146 aircraft, but they look entirely different as can be seen in Figure 1.1 and 1.2. This is due to the different operating conditions of the aircraft; the bombardier flies higher and faster than the BAe 146. The nacelle is adjusted for the air, mass flow and position requirements.

In recent years the nacelle design has regained new interest. In 2015 the first conference deal was made in Paris to opt for climate change by reducing greenhouse gasses [5]. As stated by the International Civil Aviation Organization (ICAO), the aviation sector is responsible for 2% of the global CO_2 emissions, which grows exponentially every year [6]. One proposed mitigation measure lies in an increased fuel efficiency of the engines. Turbofans can achieve this by an increased pressure ratio, combustion temperature and larger bypass ratio. Torenbeek stated in [7] that the specific fuel consumption lowers with increasing bypass ratio. A bypass ratio higher than 20 can reach fuel savings of up to 15%. However, the current design methods and materials are reaching a limit. Research has started on Ultra High bypass ratio turbofan engines which can attain a bypass ratio up to 12 [8]. Increasing the bypass ratio would also imply a larger and heavier engine. Shortening the cowling is not enough to counter this, as the flow should be able to follow the cowls curvature. [7] has shown that a bypass ratio of 10-12 has the most influence on the drag. Careful design of the nacelle should ensure that the weight and drag do not counteract the benefits.

Obert and Torenbeek describe some of the current nacelle design methods [7, 9, 10]. TsAGI's Propulsion Department performed a parametric study to show that about twenty geometric parameters of the nacelle are needed to determine the effective thrust [8]. Earlier studies have been done by [11] and [12]. These describe several flow effects with experimental data and design rules based on previous experience. Currently, the use of Computational Fluid Dynamics gives a fast understanding of the flow around a geometry. More and more, this is used to optimise the preliminary design of an engine. Examples are [8, 13, 14]. In [8], the CFD analysis is incorporated into an optimisation algorithm, such that the initial design is varied until it reaches an optimum. A change in the effective

Figure 1.1 Bombardier CL-600 with ALF502 engine [3]

Figure 1.2 ALF502 engine on a BAe 146 aircraft [4]

thrust losses of 6.5% is achieved for this design case. Optimisation techniques are promising tools to improve the engine efficiencies.

It can be concluded that for both current and future engine technology, the aerodynamic design of the engine has become paramount.Current development projects apply extensive CFD in the last stages, which only allows for small adaptions. Embedding a part of the aerodynamic design into earlier project stages can increase the design possibilities of a nacelle.

1.2 Research Aim and Questions

There is a problem in assessing the impact of the nacelle geometry on the performance during the preliminary design phases. This is striking, as a better aerodynamic performance is one of the main goals during the design of a nacelle. Nowadays, it is mostly assessed through extensive CFD research in one of the final design stages. It is the aim of this project to contribute to the solution of this problem. The main objective is therefore formulated as:

> "The project objective is to contribute to the development of a preliminary design method of an engine nacelle, focusing on the inlet, bypass and exhaust section and evaluating the impact of the resulting nacelle shape on the engine performance by parameterisation of the engine parameters and coupling the nacelle configuration to a CFD solver."

The objective is two-folded and therefore split into two sub-goals. These two sub-goals lead to further research questions to consider:

– To gain knowledge on the existing nacelle configurations and its requirements as well as a physical understanding of the engine flow phenomena.

  RQ-1 What parts and parameters characterise the existing nacelle configurations and what design steps and criteria have been used to reach these designs?

  RQ-2 What flow phenomena occur through a nacelle and what theories describe these phenomena and their impact on the engine performance?

– To progress the knowledge into a numerical design method for the aerodynamic shaping of the nacelle.

RQ-3 What parameterisation and aerodynamic analysis method are selected considering time, computational efficiency and accuracy?

RQ-4 What is the parameter sensitivity on the nacelle shape and the engine performance and how is this related to the design method and flow phenomena?

RQ-5 Are the observed flow phenomena and optimised nacelle configurations valid with those found in literature and, if not, what is the reason and how can it be improved?

RQ-6 What are the conclusions on the impact of the considered nacelle parts, separately and combined, on the performance of the engine?

1.3 Research Methodology

The two parts of the objective require a different approach. Whereas the first two questions are theoretical, the last research questions are more practical. The first two research questions are answered in the literature study which preceded this report [15]. The relevant information and terms are summarised at the beginning of this report for the understanding of the reader. The rest of this report will focus on answering the remaining research questions.

Since the aim is to develop a fast preliminary design method, the nacelle geometry is limited to a 2D axisymmetric contour. It means that no drooping, scarfing, angles of attack or different thicknesses around the nacelle can be applied. The nacelle design starts around a predefined core engine, where GasTurb 12 is used to extract the turbofan cycle data in different operating conditions. These operating conditions can be any flow condition, though this project uses the cruise and take-off conditions. These conditions are two of the most crucial flight conditions for an engine with relatively straight incoming flow. Using multiple flow conditions prevents that the nacelle only operates optimally in one flow condition and poorly in any other flow condition. Moreover, the take-off and cruise conditions have contradicting requirements, which needs an efficient compromising design.

The multiobjective optimisation uses Matlab's genetic algorithm *gamultiobj*. This command constructs a Pareto front to give the designer more freedom and insight into the different nacelle geometries. The geometry is exported from Matlab to ICEM CFD to create the grid. Fluent performs the aerodynamic analysis. Matlab then retrieves the variables of interest from Fluent, such as the drag, thrust and flow velocity.

1.4 Reading Guide

As mentioned previously in Section 1.3, the first two research questions are mostly theoretical. This will be shortly recapped from the literature survey in the first two chapters. The remaining part of the project is divided into three phases: defining the method, model development and analysing the results. The reading guide below shows which chapters are included in each phase and which chapters answer the research questions.

Phase – Theory

The aim of this part is to summarise the important terminology from previous literature report [15]. This gives a broad baseline to understand the model development.

Research Question 1

Ch. 2 Nacelle Configuration and Requirements

Phase – Method

The aim of this part is to describe the selected CFD analysis, shape parameterisation techniques and optimisation structure to ensure a fast, accurate evaluation of the design method.

Research Question 2

Ch. 3.1 Aerodynamic Flow Considerations

Research Question 3

Ch. 3.2 Shape Generation Method

Ch. 3.3 Computational Fluid Dynamics

Ch. 3.4 Optimisation Algorithm

Phase – Develop

The aim of this part is to combine the previously discussed programming techniques to develop a proper working design model. The model's interaction is discussed and verified with several test cases.

Research Question 4 & 5

Ch. 4 Model Structure

Ch. 5 Verification and Validation

Phase – Deliver

In the deliver phase the final conclusions on the model and the results are stated. Recommendations to improve the project are given.

Research Question 5 & 6

Ch. 6 Results of the Nacelle Design Method

Research Question 6

Ch. 7 Conclusions and Recommendations

2 NACELLE CONFIGURATION AND REQUIREMENTS

This chapter gives a short introduction of the possible nacelle configurations and requirements found from literature. The processes and terms explained here will be used later in the report. The content in this chapter answers the first research question; the nacelle parameters, functions and requirements.

2.1 Nacelle Configuration

The configuration of a turbofan engine varies considerably depending on the intended usage. Alternations are needed to satisfy design goals such as efficiency, reliability, comfort and noise with different levels of importance. This makes it hard to consider one definitive design approach. A common categorisation in nacelles is to classify them by geometry: the bypass ratio and exhaust type.

BPR < 2.0 Low-bypass ratio engines have a large core mass flow, similar to a jet engine. Most often it is combined with a long-ducted nacelle [7, 11, 16].

BPR > 2.0 High-bypass ratio engines have a large diameter with a larger bypass mass flow [7, 16].

Long-duct The bypass duct is extended over the entire engine length. Most often, it is combined with internal mixing of the core flow to increase the thrust and the exhaust frequency.

Short-duct The outer bypass cowling extends until after the fan to decrease weight and complexity. Drag reduces for bypass ratios above 10.

A layout of the different turbofan nacelles can be seen in Figure 2.1. Note that the core engine and fan are not considered as a part of the nacelle and are therefore not visualised. The engine's geometry and flow physics are considered to be a given and is used as a starting point for the nacelle. The nacelle includes all the external engine parts that guide the flow: the inlet, core cowl, fan cowl and plug. It is still possible to analyse the impact of many different nacelle configurations. Namely, whether the nacelle should be short- or long-duct, or whether the exhaust should be convergent or convergent-divergent, and if the plug should extend outside the core duct.

A turbofan continually experiences an angle of attack once it is installed under the wing. This angle changes during operation due to the upwash or downwash of the wings and tail. It is partly resolved by drooping and scarfing the inlet; thereby placing the inlet's centreline and the highlight under an angle to align the flow with the fan [17–20]. This, and the possible pressure distortion and swirls that arise due to flow separation, mixing and rotating parts, make the flow around the nacelle highly three-dimensional. A 2D axisymmetric nacelle cannot take the droop and scarf angles into account that are needed to improve the engine performance at higher angles of attack. But for an axisymmetric analysis, the flow inlet angle needs to remain zero, so it can therefore give a first estimate of the influence of other geometry parameters. Moreover, it reduces the computational time of any CFD calculation. It also becomes possible to analyse several geometries at different operating conditions by varying flight speed, height and mass flow. The nacelle design is therefore limited to a 2D axisymmetric geometry.

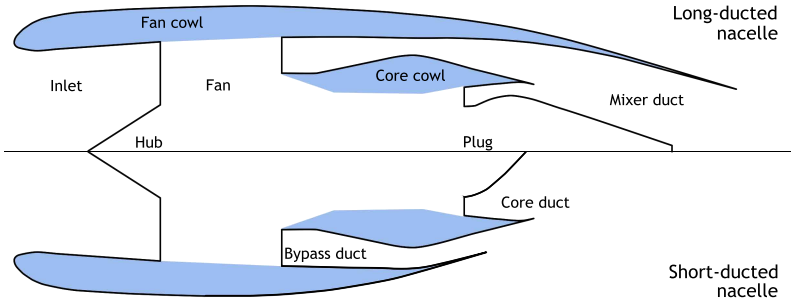

Figure 2.1 Overview of nacelle geometry

2.2 Nacelle Functions

Commonly, it is possible to divide the nacelle into three parts based on its function: the inlet, external cowling and nozzle ducts. Each part should perform their function for the entire operating range including crosswinds, stall manoeuvres and one-engine operating conditions. The functions are shortly summarised per part:

Inlet The inlet's function is to provide the required airflow as uniformly as possible to the engine by minimising the pressure losses and distortion in the entire operational range of the aircraft. The inlet guides the airflow to the fan at the required Mach number by either compressing or expanding the flow. The lip is of crucial importance as this determines the flow attachment point as well as the location of separation under various inflow angles.

Cowling The cowling's aerodynamic function is to guide the flow around the engine with the least drag. It includes boundary layer drag, separation drag, wave drag, surface drag and spillage drag. Section 3.1 explains these drag terms further. Other functions such as protection, fire containment and noise containment, are not considered in this project.

Exhaust The nozzle should provide the maximum thrust with the minimum losses. Alignment of the flow increases stability and reduce pressure losses due to swirls and incomplete mixed flow.

2.3 Nacelle Requirements

Certain requirements are necessary to ensure that the engine fulfils the previously mentioned functions in operation. These operation requirements are set on the Mach number, mass flow and flow inlet angle envelope.

- The Mach number envelope is similar to the conventional flight envelope, though less constricting. In cruise, the external nacelle is designed to reduce the supervelocities and to minimise the drag [9]. In the inlet, these supervelocities occur near the throat area. Special attention needs to be paid to the inlet geometry to prevent shock waves at the intake wall. Boundary layer separation in the inlet will not only increase the drag but have a direct influence on the performance of the engine. The pressure distortion lowers the surge limit and mass flow through the engine. A limiting average Mach number of 0.8 at the throat and 0.6 at the fan are specified to prevent shock forming or flow separation [9]. In the nozzle, the Mach number relates closely to the pressure ratio. If the total pressure is not equal to the ambient pressure, the flow is either under- or overexpanded, leading to additional shock losses. A convergent-divergent (CD) nozzle of only a few percent can be applied to balance the weight, drag and performance considerations during take-off and cruise.

- The mass flow varies considerably. The maximum mass flow ratio, MFR, is found from the flight envelope at various speeds and altitudes, but mostly occurs during take-off and climb. The minimum MFR comes from the cruise and fast climb conditions. Thus, the captured streamtube area changes depending on the operating

conditions. The lip and cowling must be designed to prevent a vast drag rise due to spillage drag or separation in these conditions. Moreover, the required mass flow might change during the development of the engine. A margin on the mass flow of 2-3% is common to prevent the redesign of the intake[9, 11].

– FAR 33.65 stipulates that inlet air distortion may not cause surge or stall from which the engine is unable to recover during any point in the flight. It means that the inlet should tolerate a large range of sideslip angles and angles of attack. This range is commonly in between -5 to 35 degrees for wing-mounted engines and -10 to 5 degrees for aft-mounted engines [11]. However, as the design is limited to axisymmetric nacelles, this requirement will not be taken into account.

Other requirements arise from safety and aviation regulations. This includes windmilling, failure containment and foreign object ingestion. The latter hardly influences the aerodynamic design and is, therefore, not considered in this project. The other two requirements will be shortly summarised below.

– Engine failure containment regulations are found in FAR 23 and FAR 25. Broken blades and fragments from the fan, compressor and turbine should be contained inside the engine to prevent structure penetration. Possible mitigation methods are using a containment ring or extending the cowling. In the latter case, the cowling should cover a fragment angle of 15° before and after the engine fan and turbine. The debris's path is also shown in Figure 2.2. This is used as a constraint on the nacelle design.

– Windmilling and locked rotors reduce the thrust and cause a roll and yaw effect. This is the most critical during take-off, as this requires the maximum thrust at low Mach numbers. The aircraft needs to remain capable of a certain climb gradient to comply with CFR 25. A mass flow rate of 0.3 and 0.15 is representative for the windmilling and locked rotor conditions [9]. Additionally, the mass flow rate increases to 2.0 at maximum thrust in low-speed operations. This causes some extreme mass flow and drag requirements.

Figure 2.2 Rotor fragment path and impact area [21]

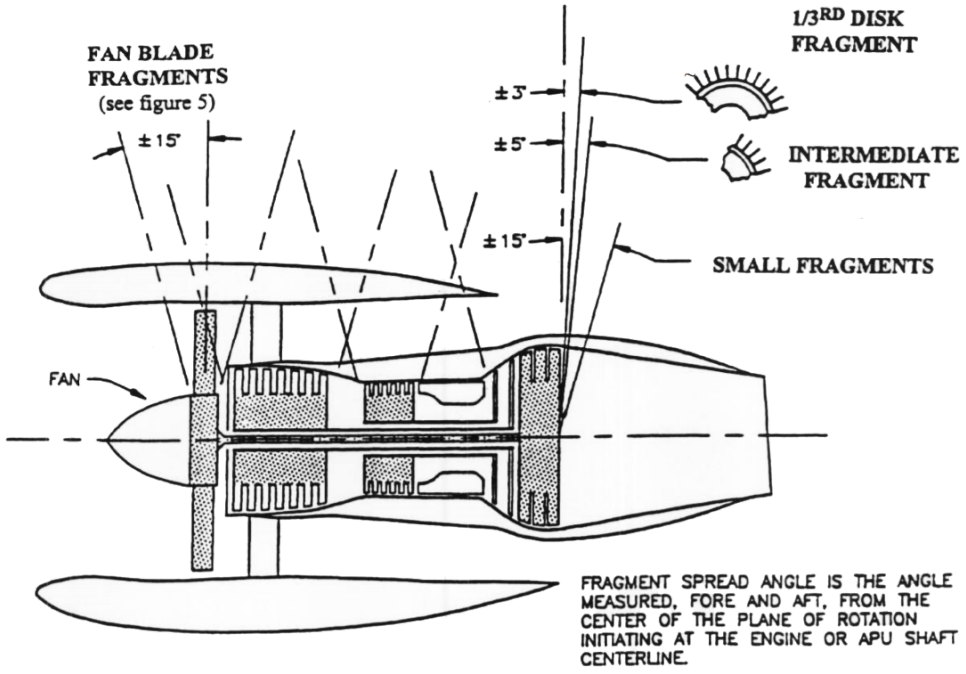

3 METHOD

There are several disciplines involved in designing a nacelle, for example, thermodynamics, structures or aerodynamics. This report mainly focuses on the aerodynamic design of a nacelle. Nonetheless, this discipline still has several steps before a nacelle can be designed. In general, it can be subdivided into three parts that interact with each other: generating the nacelle geometry, analysing the geometry in CFD and determining the thrust and drag forces from the CFD data. Together they form the background of the nacelle design method developed in this report. This chapter explains the theory, formulas and parameters used in each part in a separate section. It is a global description that applies to every nacelle. The actual parameters values and the selected test cases used for verification of this method are given in Chapter 4.

3.1 Aerodynamic Flow Considerations

The main focus of this project is to develop a nacelle geometry with the best performance in terms of thrust and drag capabilities in different flow conditions. The summation of these forces, the net propulsive force, is therefore taken as the objective of this report. The calculation of this force and how it is obtained from CFD data are found in Section 3.1.4. The Sections before this explain the theory and calculations of the different force components used for the net propulsive force.

3.1.1 Thrust Accounting Method

An engine should generate the largest propelling thrust with the least fuel and drag losses. However, the actual forward propelling force consists of different components. A bookkeeping structure becomes necessary to prevent that components are overlooked or used multiple times. This section will explain the bookkeeping structure as found in [22], but [10, 11, 23, 24] show similar examples. The basic force components around an isolated nacelle are visualised in Figure 3.1. The forces from this figure are divided in two: the thrust forces, F_{G}, that act in the cross-sectional plane and the drag forces, ϕ, that act along the surface plane. The latter is explained in more detail in the next section, Section 3.1.2. The thrust calculation is explained in this section.

The force F_G is called the gross thrust. It is calculated as the momentum increase from the freestream due to a change in flow velocity and static pressure, as shown in Equation 3.1.

$$\begin{aligned} F_{\mathrm{G}} &= \int_A (\rho V^2 + (P - P_\infty)\mathrm{d}A \\ &= \dot{m}V + A\,(P - P_0) \end{aligned} \tag{3.1}$$

The actual thrust of the engine is the change in gross thrust between the inlet and exhaust of the system. The choice on the location of these exhaust and inlet stations can vary. One option is to place these stations at the actual duct surfaces (stations 1, 19 and 9 in Figure 3.1). This is the definition of the intrinsic thrust, as shown in Equation 3.2.

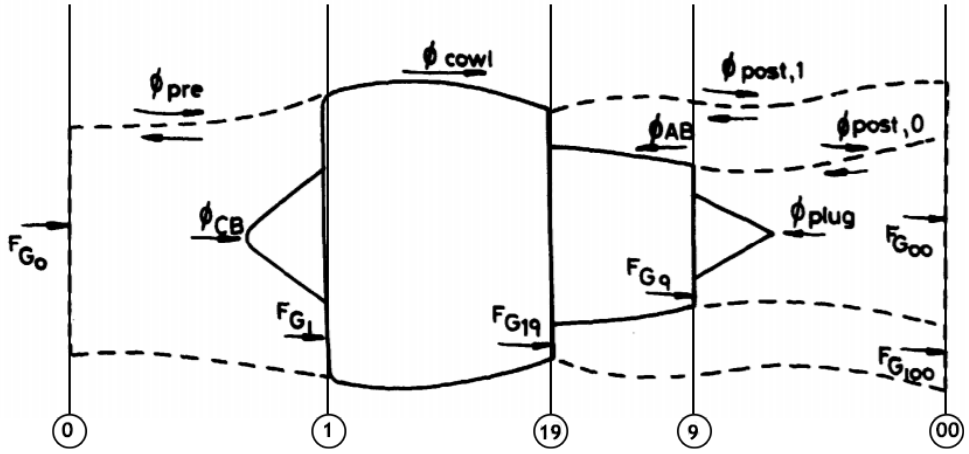

Figure 3.1 Thrust forces, F_G, acting on the cross-sectional plane and drag forces, ϕ, acting on the surface of a short nacelle configuration [Adapted from [22]]

$$T_{\text{int}} = F_{\text{G}_{19}} + F_{\text{G}_9} - F_{\text{G}_1} \tag{3.2}$$

A disadvantage of this definition is that it strongly depends on the geometry. Especially the location of station 1 is difficult to predict. This station lies at the lip's stagnation point and thus varies with the flow conditions and lip geometry. Another option is to use the definition of the net thrust. The net thrust is instead related to station 0, the captured freestream area in front of the nacelle. This term, F_{G_0}, is sometimes called the ram drag, as it is always subtracted from the thrust.

$$T_{\text{net}} = F_{\text{G}_{19}} + F_{\text{G}_9} - F_{\text{G}_0} \tag{3.3}$$

$$= \int_{A_{19}} (\rho V^2 + (P - P_\infty)\mathrm{d}A + \int_{A_9} (\rho V^2 + (P - P_\infty)\mathrm{d}A - \dot{m}V_0 \tag{3.4}$$

3.1.2 Drag Accounting Method

The symbols ϕ in Figure 3.1 indicate the forces along a surface. These foces only act on the external surface: there is a split between the internal and external drag. This split is commonly used by engineers to design several engine parts in parallel during the engine's development. The duct determines where this split occurs: the forces outside of the duct are treated as drag, while the aerodynamic losses within the duct are treated as a loss in thrust [25]. This section will focus on the drag while Section 3.1.5 explains the duct losses.

For the bookkeeping of the external surface forces ϕ, a division into three parts can be made: pre-entry, nacelle and post-exit forces. The nacelle drag is defined as the summation of these forces:

$$D_{\text{nac}} = \phi_{\text{pre}} + \phi_{\text{nac}} + \phi_{\text{post}} \qquad [22] \tag{3.5}$$

The pre-entry and post-exit forces are the forces acting along the streamtube surfaces as visualised in Figure 3.1. Finding or predicting this boundary line is a difficult and expensive task. Instead, Newton's second law can be used to express the idealised streamtube forces in terms of the gross thrust components:

$$\phi_{\text{tube}} = \int_{S_{\text{tube}}} P_{\text{s}}\mathrm{d}S \tag{3.6}$$

$$\phi_{\text{pre}} = F_{\text{G}_1} - F_{\text{G}_0} + \phi_{\text{CB}} \tag{3.7}$$

$$\phi_{\text{post},0} = F_{\text{G}_\infty} - F_{\text{G}_9} + \phi_{\text{p}} \tag{3.8}$$

$$\phi_{\text{post},1} = F_{\text{G}_{1,\infty}} - F_{\text{G}_{19}} + \phi_{\text{AB}} + \phi_{\text{post},0} \tag{3.9}$$

The nacelle surface forces shown in Figure 3.1 are ϕ_{CB}, ϕ_{cowl}, ϕ_{AB} and ϕ_{p}. These surface forces are generated by different aerodynamic phenomena, such as pressure differences, viscous and interference effects. Their force is calculated using the near-field method. Rather than calculating the different flow forces, their counteracting force on the nacelle surface is calculated. This can be done by integrating the pressure and shear forces as shown in Equation 3.10.

$$\phi_{\text{nac}} = \int_{S_{\text{nac}}} n_x \left(P - P_0\right) + \tau \mathrm{d}A \tag{3.10}$$

By using the near-field method, the surface drag is completely defined by the pressure and friction the flow exerts on the nacelle. The pressure drag is retrieved from the CFD analysis. The friction drag is calculated with the formula shown in Section 3.1.3. Calculating the total drag in this way does not explain why certain flow phenomena occur and how they each contribute to the total drag. Many drag terms exist to describe each flow phenomena. For illustrative purposes, these main drag terms and their relation to the surface forces ϕ are explained below. However, their value is not explicitly calculated.

Spillage drag Spillage drag is a drag that occurs on the inlet's lip. When the MFR is 1, the nacelle's inlet completely captures the upstream streamtube. In this case, the pre-entry force equals the lip suction force, $F_{\text{G}_0} = F_{\text{G}_1}$ [22]. A lower MFR or high angles of attack cause the stagnation point to shift outward: a part of the incoming air has to turn around the fan cowl and is 'spilled'. It reduces the mass flow going through the inlet, and thus the velocity is lowered. On the other hand, there is a higher chance of separation on the outer fan cowl because this experiences a velocity increase. The spillage drag is, therefore, incorporated in the pre-entry and cowl drag. This is shown in Equation 3.11. The spillage drag is the difference of two terms: the increase in pre-entry drag that arises when the $MFR \neq 1$ and the difference in fan cowl drag from the reduction in mass flow.

$$D_{\text{spillage}} = \phi_{\text{pre}} - \left(\phi_{\text{cowl}_{MFR=1}} - \phi_{\text{cowl}}\right) \quad [22] \tag{3.11}$$

Scrubbing drag For short-duct turbofans, an additional drag force is produced on the plug and external core cowl. These nacelle parts are placed inside the jet streams, which have a higher velocity than the freestream. This addition in pressure and friction drag is called the scrubbing drag. The scrubbing drag decreases with the bypass ratio, as a larger bypass flow reduces the velocities of the jet streams [7]. The actual influence of the scrubbing drag is hard to estimate as shocks can form in the jet stream. This drag is therefore not separately calculated but included in ϕ_{AB} and ϕ_{p}.

Boattail drag The boattail is the part of the fan cowl and core cowl that tapers down towards the nozzle. The exhaust flows from the fan and turbine influence the pressure over these nacelle parts. Especially an underexpanded nozzle, where the exhaust pressure is higher than the ambient pressure, has a large influence on the boattail. The higher exhaust pressure causes the jet stream to expand outward, and this generates a large adverse pressure gradient over the boattail [9]. The dip in the transition from the boattail to the expanding jet stream often results in a separated region. Higher boattail angles will aggravate this effect, which is explained in more detail in Section 3.2.4. An initial angle of 15° and a curvature radius to cowl diameter above 4 can be taken as a guideline to prevent large separation regions [9, 11].

Interference drag Just as the name suggests, interference drag is the increase in drag when the flow around an object changes in the vicinity of another nearby object. An example is the mutual interference of the nacelle and pylon. The sum of the drag contributions from the isolated pylon and nacelle is not the same as the total drag of the system. The difference is the interference drag. However, this project only considers an isolated nacelle and does not take the interference contribution of the pylon and wing into account.

Interference drag is still present on the afterbody of an isolated nacelle. It occurs between the two jet streams of a non-mixing nacelle configuration. The drag is seen as a change in afterbody force due to the jet effects. If the two exhaust streams are perfectly expanded, and the pressure of both streams is the same, there will be no interference drag and the post-exit force will be zero [22]. Taking this as a datum condition, the interference drag can be determined with Equation 3.12, where $D_{P_{19,9}=P_\infty}$ is the reference drag when the exhaust flow is completely expanded. The difference between the actual jet stream and the ideal reference condition is the interference drag.

$$D_\mathrm{i} = \phi_\mathrm{AB} + \phi_\mathrm{p} + \phi_\mathrm{post} - D_{P_{9,19}=P_\infty} \qquad [22] \quad (3.12)$$

3.1.3 Friction drag

Friction drag is one of the largest contributions to the total drag, as it can go up to 50% [11]. Since Euler equations are used in the CFD analysis, this contribution is not included in the CFD data. Nevertheless, it can be approximated with the empirical relations proposed by [7]:

$$D_\mathrm{friction} = FF \cdot C_F \cdot q \cdot S_\mathrm{wet,nac} \qquad [7] \quad (3.13)$$

In Equation 3.13 is q the dynamic pressure, S_wet the wetted area of the nacelle parts, FF is the form factor and C_F is the skin friction coefficient. The term $qS_\mathrm{wet,nac}$ is calculated with the CFD data along the surface. This data includes the increase in friction drag due to the priory mentioned boattail, scrubbing and interference drag and therefore gives more accurate results. The program Fluent, which is used for the simulations, integrates the dynamic pressure over a surface according to Equation 3.14.

$$\int q \mathrm{d}A = \sum_{i=1}^{n} q_i \cdot A_i \qquad [26] \quad (3.14)$$

The symbol q_i is the average facet dynamic pressure value along the surface boundary and A_i is the corresponding facet area. It overpredicts the friction drag as it does not take the boundary layer into account, so the flow will stay longer attached and at a higher velocity near the surface. However, this is balanced out by the lack of separation drag. [27] compares several numerical methods on their performance for exhaust nozzles and boattails. Inviscid methods such as the potential flow theory and Crowns mesh method showed nearly identical results to the experimental data in the subsonic region up to Mach 0.8. [28] reports similar results for an over-the wing nacelle configuration.

C_F is the skin friction coefficient that can be used to calculate the basic skin friction drag. Equation 3.15 uses the Prandtl-Schlichting relation for the skin friction of a flat plate in a turbulent flow.

$$C_F = \frac{0.455}{\log {Re_l}^{2.58}} \qquad [7,\ 29,\ 30] \quad (3.15)$$

The Reynolds number, Re, is based on the length of the nacelle parts immersed in the different flow streams, as shown in Equation 3.16. Equation 3.17 shows Sutherland's law for the dynamic viscosity μ. The static temperature, velocity and density needed for the Reynolds number and dynamic viscosity are based on the average CFD data of the nacelle part considered. Fluent also calculates these at the facet areas, as shown in Equation 3.18 for the static temperature. Note that this equation can be applied for any field variable.

$$Re_l = \frac{\rho V L_\mathrm{part}}{\mu} \qquad [7] \quad (3.16)$$

$$\mu = \frac{1.458 \cdot 10^{-6} T_\mathrm{s}^{\frac{3}{2}}}{T_\mathrm{s} + 110.4} \qquad (3.17)$$

$$T_{\mathrm{s}} = \frac{1}{A}\int T_{\mathrm{s}}\mathrm{d}A = \frac{1}{A}\sum_{i=1}^{n} T_{\mathrm{s}_i}|A_i| \qquad [26] \quad (3.18)$$

Roughness drag is another contribution to the friction drag. How much these imperfections increase the drag depends on the Reynolds number. At low Reynolds numbers, the boundary layer is very thick and contains the roughness elements. As long as these elements stay immersed, the friction drag will be the same as that of a smooth plate. This part of the friction drag slowly decreases with increasing Reynolds number. At some point, the boundary layer becomes too thin to contain the disturbances. Small vortices will be shed from these disturbances so that the flow becomes turbulent [9]. The skin friction in Equation 3.15 assumes that the complete boundary layer is turbulent to account for these irregularities [7]. However, the increasing pressure from the vortices influences the friction drag and the friction drag will remain constant after a certain Reynolds number [9]. At which Reynolds number this occurs depends on the size of the irregularities. Nikurade investigated the roughness drag by covering the inside of circular pipe sections with sand [9, 29]. Nowadays, a separate factor correlates the roughness of any body to the sand roughness from Nikurade's experiments. This factor is the equivalent sand roughness k_s. A painted aircraft surface has an equivalent sand roughness of approximately 20 microns [7, 31]. Equation 3.19 is used to calculate the constant skin friction coefficient above the cut-off Reynolds number. This equation is proposed in [31] for Nikurade's experimental data for a sand roughness in between $10^{-5} - 10^{-3}$ [31].

$$C_{F_{\mathrm{termi}}} = 0.032\left(\frac{k_s}{L_{\mathrm{part}}}\right)^{\frac{1}{5}} \qquad [31] \quad (3.19)$$

The last variable to discuss is the form factor FF. The basic skin friction only includes the drag that a flat plate of the same proportions would experience. However, the nacelle curvature increases the local flow velocity around the fore- and afterbody. The form factor accounts for the effect of curvature on the flow, which is calculated with Equation 3.20. The fraction $\frac{l}{d}$ is the slenderness ratio which can be calculated with Equation 3.21. This equation directly models the nacelle surfaces as a body of revolution [32]. Similarly to the dynamic pressure and skin friction coefficient, this is calculated for each nacelle part separately.

$$FF = 1 + \frac{1.5}{\frac{l}{d}^{1.5}} + \frac{7}{\frac{l}{d}^{3}} \qquad [31] \quad (3.20)$$

$$\frac{l}{d} = \frac{L_{\mathrm{nac,part}} + D_{\mathrm{in}}}{\sqrt{\frac{4}{\pi}\left(A_{\mathrm{max}} - \frac{A_{\mathrm{exit}}+A_{\mathrm{in}}}{2}\right)}} \qquad [32] \quad (3.21)$$

The friction drag is calculated for both the internal and external surfaces, whereas the pressure drag is only calculated for the external surfaces. Since the Euler equations do not take any viscous effect into account, there is no boundary layer development in the internal duct. This would overestimate the thrust forces at the duct exit, as there are no velocity and pressure losses due to friction. To compensate for this effect, the friction is calculated on every wetted surface area of the nacelle.

3.1.4 Net Propulsive Force

The thrust calculation of the engine has been explained in Section 3.1.1. For the complete engine performance, also the nacelle plays a role. The shape and structure of the nacelle induce drag terms that need to be subtracted from the force that the engine delivers. These terms have been previously explained in Section 3.1.2. The combination of these influences is calculated with the net propulsive force (NPF). The net propulsive force is the main objective that needs to be increased during the design. In the aerodynamic design of the nacelle, it can be achieved by reducing the drag components and by optimising the nozzle duct such that the highest exhaust velocity can be reached. This section shows the definition of the NPF as well as its calculation from the CFD data.

The net propulsive force is the overall forward thrust on the engine system. Using the control volume as defined in Figure 3.1, the following definition of the net propulsive force can be used:

$$NPF = F_{\mathrm{G}_\infty} + F_{\mathrm{G}_{1,\infty}} - F_{\mathrm{G}_0} - D_{\mathrm{nac}} \tag{3.22}$$

The thrust is here determined using the unperturbed upstream force with respect to the fully expanded gross thrust. However, the latter is difficult to determine without extensive wake process analysis. In this case, the thrust can be rewritten in terms of the nacelle exit stations 19 and 9, which can be obtained from CFD results and are directly related to the nacelle exhaust geometry. Inserting Equations 3.8 and 3.9 gives:

$$\begin{aligned} NPF &= F_{\mathrm{G}_9} + F_{\mathrm{G}_{19}} - F_{\mathrm{G}_0} + \phi_{\mathrm{post},1} - \phi_{\mathrm{p}} - \phi_{\mathrm{AB}} - D_{\mathrm{nac}} \\ &= T_{net} + \phi_{\mathrm{post},1} - \phi_{\mathrm{p}} - \phi_{\mathrm{AB}} - D_{\mathrm{nac}} \\ &= T_{\mathrm{net}} - \phi_{\mathrm{p}} - \phi_{\mathrm{AB}} - \phi_{\mathrm{pre}} - \phi_{\mathrm{cowl}} \qquad [22] \end{aligned} \tag{3.23}$$

This is rewritten in terms of the intrinsic thrust, thereby eliminating ϕ_{pre} and F_{G_0}. It simplifies the equation further, as the determination of the streamtube boundaries and forces become unnecessary. This is shown in Equation 3.24, with the use of Equations 3.2, 3.3 and 3.7.

$$\begin{aligned} NPF &= T_{\mathrm{int}} + F_{\mathrm{G}_1} - F_{\mathrm{G}_0} - \phi_{\mathrm{pre}} - \phi_{\mathrm{p}} - \phi_{\mathrm{AB}} - \phi_{\mathrm{cowl}} \\ &= T_{\mathrm{int}} - \phi_{\mathrm{CB}} - \phi_{\mathrm{p}} - \phi_{\mathrm{AB}} - \phi_{\mathrm{cowl}} \qquad [22] \end{aligned} \tag{3.24}$$

As mentioned previously, the term F_{G_1} depends on the stagnation point and shifts depending on the flow conditions. However, in cruise, this point is very close to the highlight plane as the MFR will be close to 1 for optimum cruise conditions. In take-off, when the MFR increases, the stagnation point shifts outwards. In most cases, this distance is minimal and negligible. Furthermore, the pressure over the surface between the highlight and the actual stagnation point is instead incorporated in the pressure drag. F_{G_1} is therefore assumed fixed at the highlight plane.

The thrust forces depend on the area, pressure difference and velocity. The area integral for the pressure is directly computed with Fluent, using Equation 3.14 but then for the pressure $P_i - P_\infty$. The pressure $P_i - P_\infty$ is the average cell face value at the exit planes. Similarly, Fluent uses Equation 3.25 for the axial velocity and mass flow facet values on the exit planes.

$$\int \rho \overrightarrow{u}^2 \mathrm{d}A = \sum_{i=1}^{n} \rho_i \overrightarrow{u_i}^2 \cdot \overrightarrow{A_i} \qquad [26] \tag{3.25}$$

The surface forces ϕ include a pressure and viscous part. Since Euler equations are used, the viscous part is not obtained directly from the CFD analysis but from the empirical friction drag formula described in Subsection 3.1.3. The pressure forces are obtained directly from the external nacelle surfaces by generating a Force report in Fluent. This uses Equation 3.26 to discretise the pressure force, where P_i is the static pressure of the cell, A is the cell's face area and p_{ref} is the given reference pressure, P_∞.

$$D_p = \sum_{i=1}^{n} \left(P_i - P_{\mathrm{ref}}\right) A n_x \qquad [26] \tag{3.26}$$

3.1.5 Nozzle Coefficients

The performance of a nozzle is captured mostly by the loss in thrust rather than the drag. Losses such as skin friction, offset losses and pressure losses reduce the pressure and velocity terms at the duct's exit and thus the gross thrust. Another commonly used method to evaluate these losses is through the nozzle coefficients. These coefficients indicate how much the flow differs from the ideal isentropic flow. Three coefficients are used to capture these errors: the velocity coefficient, the discharge coefficient and the thrust coefficient. All three ratios are shown in Equation 3.27 through 3.29. Note that in Equation 3.30, two different ratios are used. The difference depends on

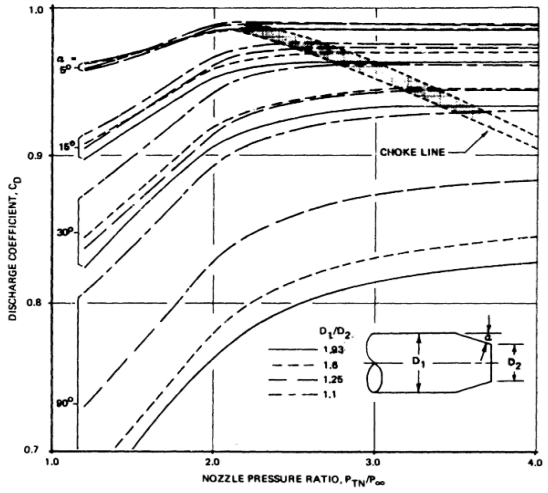

Figure 3.2 Nozzle discharge coefficient variation with nozzle contraction ratio and angle [33]

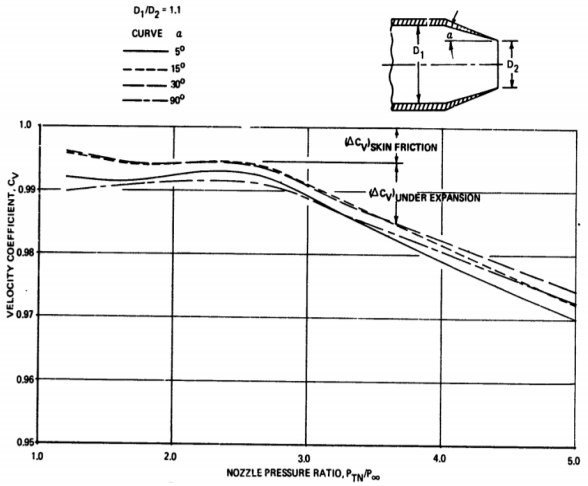

Figure 3.3 Velocity coefficient variation with nozzle wall angle [33]

the station where the discharge coefficient is determined. In case this is at the exhaust area, the thrust coefficient is exactly equal to the product of the two other coefficients. For a convergent-divergent nozzle, the discharge coefficient can also be determined at the throat area. In this case, the equation needs an additional area ratio [22].

$$C_v = \frac{V_{\text{act}}}{V_{\text{id}}} \qquad [9] \quad (3.27)$$

$$C_d = \frac{\dot{m}_{\text{act}}}{\dot{m}_{\text{id}}} \qquad [9] \quad (3.28)$$

$$C_t = \frac{F_{\text{act}}}{\dot{m}_{\text{id}} V_{\text{id}}} = \qquad [9] \quad (3.29)$$

$$= C_v C_{d_9} \quad or \quad C_v C_{d_8} \frac{A_{9_{\text{act}}} A_{8_{\text{id}}}}{A_{8_{\text{act}}} A_{8_{\text{act}}}} \qquad [22] \quad (3.30)$$

The discharge coefficient can not be evaluated with an inviscid simulation, as it is a measure of the boundary layer formation inside the nozzle. This layer reduces the actual geometric area. Especially in chocked conditions, when the mass flow cannot further increase, the boundary layer formation becomes paramount. The discharge coefficient is, therefore, influenced by the nozzle pressure ratio (NPR), exhaust velocity and the rate at which the nozzle contracts. The latter is described by the wall cone angle θ_{cone}.

The velocity coefficient depends on the viscous losses at the exhaust plane. These viscous losses are influenced by both the effective flow area and the exhaust pressure. It is possible to rewrite the velocity coefficient in terms of the discharge coefficient and nozzle pressure ratio, as shown in Equation 3.31. In this form, the velocity coefficient is related inversely to the discharge coefficient. This can also be seen in Figure 3.2 and 3.3, where several conditions are contradicting each other. A high nozzle pressure ratio and a small contraction angle are advantageous for the discharge coefficient. On the other hand, the velocity coefficient rapidly decreases for nozzle pressure ratios above 2.5. The contraction angle influences the velocity coefficient less than the discharge coefficient, though it also shows that angles between 15°-30°are favourable. A trade-off has to be made to optimise the thrust coefficient C_t for the different operating conditions.

$$C_v = \sqrt{\left[1 - \left(\frac{P_{s_9}/P_{s_0}}{NPR \cdot \frac{P_{t_9}}{P_{t_7}}}\right)^{\frac{\gamma-1}{\gamma}}\right] \left[1 - \left(\frac{P_{s_9}/P_{s_0}}{NPR \cdot C_{D_8}^2}\right)^{\frac{\gamma-1}{\gamma}}\right]^{-1}} \qquad [12] \quad (3.31)$$

These three coefficients measure the loss in the magnitude of thrust. However, the direction of the thrust force also influences the performance. As the flow expands at the exhaust, a part of the thrust force is lost as the flow is

directed outward. Of course, the expansion angle varies over the exhaust plant. If the nozzle is of sufficient length, then the flow can be assumed to follow a point source pattern. In that case Equation 3.32 can be derived for the angularity loss coefficient C_a.

$$C_a = \frac{1}{2}\left(1 + \cos\phi_{\mathrm{i}}\right) \qquad [12,\ 34] \qquad (3.32)$$

3.2 Shape Generation Method

A computational optimisation evaluates and adapts a nacelle geometry multiple times. It becomes paramount to simplify the geometry to reduce the complexity and time required. Shape parameterisation is, therefore, a frequently researched topic and often used in multidisciplinary design optimisation (MDO) and CFD. Examples of parameterisation methods are polynomials and splines. Polynomial curves are used frequently and form the basis for more advanced methods, such as the Class-Shape Transformation (CST) method. A disadvantage is that higher-order polynomials, which are needed to construct more complex curves, produce oscillations and numerical instabilities [35]. Splines counter this problem by breaking the curve up into several lower-order polynomials. There are various spline methods with different degrees of flexibility and ability to represent circles, ellipses and cones [35, 36]. Also, [37] has shown that at least 4-6th order polynomials are needed to describe a predefined airfoil and its aerodynamic forces accurately. For this preliminary study, it is preferred to decrease the number of parameters and speed up the program so that it evaluates more nacelle geometries. A parametric study by TsAGI's Propulsion Department shows that about 20 geometric parameters are needed to determine the effective thrust of a short-duct nacelle [8]. This project uses a combination of ellipses, polynomials and splines to reach this.

As mentioned in Chapter 2, a nacelle can have a long or short-duct which has either a convergent or convergent-divergent (CD) exhaust. This section will describe how the geometry for each type of nacelle is created. However, the design strategy is independent of the nacelle type and starts with defining the plug geometry. From here, the geometry is defined from the aft towards the front: the core duct, the core cowl, the bypass duct and finally the fan cowl. The inlet is designed separately from the nozzles, where the nacelle's maximum diameter is considered the transition between the two areas. Section 3.2.1 explains which constant variables are used for the geometry. The geometry of the core duct, bypass duct and inlet is shown in Sections 3.2.2, 3.2.3 and 3.2.4 respectively.

3.2.1 Fixed Geometry Parameters

This project's goal is to design the optimum nacelle geometry around an engine; the core engine's dimensions are considered fixed. These dimensions are shown in Figure 3.4. Two different fan diameters, D_{fan} and $D_{\mathrm{fan_{exo}}}$, can be specified to vary the inlet and exit of the fan casing. Moreover, this figure includes two clearance requirements: above the fan case ($y_{\mathrm{fan_{clr}}}$) and above the turbine mounting ring ($y_{\mathrm{t_{clr}}}$). This ensures that enough volume remains for other equipment, such as cooling equipment and thrust reversers. Typical clearance requirements, as proposed by [38], are 12.7 cm for $y_{\mathrm{fan_{clr}}}$ and 2.54 cm for $y_{\mathrm{t_{clr}}}$.

The exhaust area is needed to determine the duct geometry. These areas have to be determined with some key cycle parameters. Table 3.1 summarises the minimum cycle engine parameters needed, as they are used for the CFD's boundary conditions. This is explained in more detail in Section 3.3. Currently, there is hardly any data available on the engine cycle design. Programs such as GasTurb [39] can be used to determine any unknown parameters. This program can model and simulate the gas turbine on a system level and, once the design point is known, evaluate the engine performance on off-design conditions. Besides the parameters shown in the table, also the duct pressure ratio influences the area to some extent. This value is not always known upfront and is close to unity for a well-designed duct. This will only give differences of a few millimetres in the exhaust radius. The following two subsections explain how the parameters shown in Table 3.1 are used to determine other fixed parameters, such as the flow conditions and exhaust areas at the beginning and end of a nozzle.

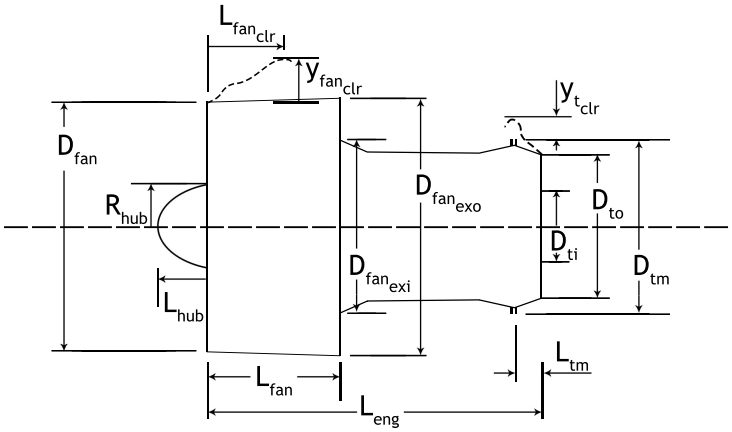

Figure 3.4 Required core engine dimensions for the nacelle design [Adapted from [38]]

Table 3.1 Key engine cycle parameters

M	Mach number	-	h	Altitude	m
$\dot{m}_{\mathrm{corr}}$	Corrected mass flow	$\frac{kg}{s}$	$\dot{m}_{\mathrm{fuel}}$	Fuel mass flow	$\frac{kg}{s}$
BPR	Bypass ratio	-	FPR	Fan pressure ratio	-
P_{t_5}	Total pressure after LPT	Pa	T_{t_5}	Total temperature after LPT	K
γ_{g}	Poisson constant for gas	-	C_{p}	Specific heat coefficient for gas	$\frac{kJ}{kgK}$
η_{fan}	Fan efficiency	-			

3.2.1.1 Core engine inlet conditions

The cycle parameters, as shown in Table 3.1, are needed to determine the aerodynamic conditions at the beginning of the inlet, bypass and core duct. Thus the duct geometry will be adapted and optimised for a predefined airflow. Firstly, the mass flow through each duct needs to be determined. The atmospheric conditions before the inlet are defined with the mass flow, Mach number and altitude. Other airflow conditions can then be calculated with the International Standard Atmosphere (ISA) relations. The total required mass flow is often corrected with the ISA sea-level conditions to obtain the corrected mass flow $\dot{m}_{\mathrm{corr}}$ as shown in Equation 3.33. The corrected mass flow allows for a direct comparison between engines independent of the flight conditions. Equation 3.34 then calculates the mass flow going through the bypass and the core.

$$\dot{m}_{\mathrm{corr}} = \dot{m} \frac{\sqrt{\frac{T_{\mathrm{t}_{\mathrm{fan}}}}{T_{\mathrm{t}_\infty}}}}{\frac{P_{\mathrm{t}_{\mathrm{fan}}}}{P_{\mathrm{t}_\infty}}} \tag{3.33}$$

$$BPR = \frac{\dot{m}_{\mathrm{b}}}{\dot{m}_{\mathrm{c}}} \tag{3.34}$$

Secondly, the pressure and temperature conditions at the fan need to be determined for the CFD analysis. These follow directly from the atmospheric conditions and the isentropic relations. Their calculation is shown in Equations 3.35 and 3.36.

$$T_{\mathrm{t}_{\mathrm{fan}}} = T_\infty \left(1 + \frac{\gamma_{air} - 1}{2} M^2\right) \tag{3.35}$$

$$P_{t_{fan}} = P_\infty \left(1 + \frac{\gamma_{air} - 1}{2} M^2\right)^{\frac{\gamma_{air}}{\gamma_{air}-1}} \tag{3.36}$$

Thirdly, the pressure and temperature at the start of the bypass nozzle can be determined with Equations 3.37 and 3.38. However, the fan causes multiple inlet distortion effects. The rotation of the fan causes radial swirls of different intensities and shapes [40, 41]. This lowers the surge limit and the mass flow of the engine. Since the inlet shape is unknown and the effects are highly three-dimensional, it is not possible to analyse this effect in this project. The fan efficiency incorporates any additional losses over the fan.

$$T_{t_{fan_{ex}}} = T_{t_{fan}} \left(1 + \frac{1}{\eta_{fan}} \left(FPR^{\frac{\gamma_{air}-1}{\gamma_{air}}} - 1\right)\right) \tag{3.37}$$

$$P_{t_{fan_{ex}}} = FPR \cdot P_{t_{fan}} \tag{3.38}$$

3.2.1.2 Nozzle conditions

The exhaust areas for a convergent or CD nozzle depend on the exhaust's flow conditions. First, the flow conditions at the smallest cross-sectional area, the throat, need to be determined. For a convergent nozzle, the throat area is simultaneously the exhaust area. The calculation of the exhaust area depends on whether the flow is choked. A flow is choked once it reaches Mach number of 1 at the throat, and the mass flow cannot increase further. The critical nozzle pressure ratio at which choking occurs is calculated with Equation 3.39. Typical NPR during cruise are in the order of 2.0-3.0. The NPR lowers to 1.5-2.0 during take-off [9].

$$\epsilon_{crit} = \frac{P_t}{P_{crit}} = \left(1 - \frac{1}{\eta_n}\frac{\gamma - 1}{\gamma + 1}\right)^{\frac{-\gamma}{\gamma+1}} \approx \frac{\gamma + 1}{2}^{\frac{\gamma}{\gamma+1}} \quad [12] \tag{3.39}$$

For a one-dimensional isentropic flow, the relations in Table 3.2 can be used to calculate the throat area for an unchoked and choked duct flow. These equations hold for both the bypass duct and the core duct.

Table 3.2 Internal flow calculations for a convergent nozzle [30]

$NPR < \epsilon_{crit}$	$NPR \geq \epsilon_{crit}$
$M_{ex} = \sqrt{\frac{2}{\gamma-1}\left(\left(\frac{P_{t_7}}{P_{s_\infty}}\right)^{\frac{\gamma-1}{\gamma}}\right)}$	$M_{ex} = 1$
$P_{s_{ex}} = P_\infty$	$P_{s_{ex}} = P_{t_7}/\epsilon_{crit}$
$A_{ex} = \frac{\dot{m}\sqrt{T_{s_{ex}}}}{M_{ex}P_{s_{ex}}}\sqrt{\frac{R}{\gamma}}$	$A_{ex} = \frac{\dot{m}\sqrt{T_{s_{ex}}}}{P_{s_{ex}}}\sqrt{\frac{R}{\gamma}}$

A CD nozzle further expands the exhaust flow towards ambient pressure to increase its velocity. Whether this is beneficial for the net propulsive force depends on the nozzle pressure ratio, the geometry and the flow conditions. Even if the CD nozzle increases the performance during cruise, it can cause over-expansion during other flight conditions. When the NPR falls below 0.3-0.4, separation will occur as the ambient pressure propagates upstream of the diverging section [30]. A CD nozzle is more effective for engines with a high NPR. An increase of 5% in gross thrust can be reached for NPR around 5.5 [30]. In that case, the exhaust and throat areas can be calculated with the left and right side equations of Table 3.2 respectively.

The same equations apply for a long-duct nacelle, but the upstream conditions change as the fan and core flow are no longer separated. The velocity difference between the core and fan flow will mix the two streams. This is beneficial for both the thrust and noise. Mixing breaks the eddies up into smaller vortices which increases the noise frequency [11, 42]. A lob can be applied to increase the flow's mixing forcefully. This is a curved annular ring placed at the point where the bypass flow and core flow converge. Swirls are introduced as the air sheds from the lob's curves. Care must be taken that the flow has long enough to mix in the duct because any swirling components remaining at the exhaust decreases the axial velocity and therefore the thrust [43]. However, The effect of mixing

cannot be analysed with an axisymmetric Euler model. [44] has shown that free mixer configurations improve the specific fuel consumption by 0.5 % compared to the optimised separate flow condition. Analysing a long-duct nacelle remains possible with a marginal error in the thrust. The area and ideal full mixed flow conditions can again be calculated by assuming a one-dimensional flow with the following set of equations:

$$\begin{aligned}
\text{Continuity:} \quad & \rho_{\mathrm{mxd}} A_{\mathrm{mxd}} V_{\mathrm{mxd}} && = \rho_{\mathrm{c}} A_{\mathrm{c}} V_{\mathrm{c}} + \rho_{\mathrm{f}} A_{\mathrm{f}} V_{\mathrm{f}} && (3.40)\\
\text{Momentum:} \quad & P_{\mathrm{s}_{\mathrm{mxd}}} A_{\mathrm{mxd}} + \dot{m}_{\mathrm{mxd}} V_{\mathrm{mxd}} && = (P_{\mathrm{s}_{\mathrm{f}}} A_{\mathrm{f}} + \dot{m}_{\mathrm{f}} V_{\mathrm{f}}) + (P_{\mathrm{s}_{\mathrm{c}}} A_{\mathrm{c}} + \dot{m}_{\mathrm{c}} V_{\mathrm{c}}) && (3.41)\\
\text{Energy:} \quad & \dot{m}_{\mathrm{mxd}} C_{\mathrm{p}_{\mathrm{mxd}}} T_{\mathrm{t}_{\mathrm{mxd}}} && = \dot{m}_{\mathrm{c}} C_{\mathrm{p}_{\mathrm{c}}} T_{\mathrm{t}_{\mathrm{c}}} + \dot{m}_{\mathrm{f}} C_{\mathrm{p}_{\mathrm{f}}} T_{\mathrm{t}_{\mathrm{f}}} && (3.42)\\
\text{Equation of state:} \quad & P_{\mathrm{s}} && = \rho R T_{\mathrm{s}} && (3.43)\\
\text{No swirl:} \quad & P_{\mathrm{s}_{\mathrm{c}}} && = P_{\mathrm{s}_{\mathrm{f}}} && (3.44)
\end{aligned}$$

There are five equations and five unknowns: the fully mixed conditions $P_{\mathrm{s}_{\mathrm{mxd}}}$, ρ_{mxd}, V_{mxd} and $T_{\mathrm{t}_{\mathrm{mxd}}}$ as well as the static pressure in front of the mixing plane $P_{\mathrm{s}_{\mathrm{c}}}$. The mixing conditions are therefore completely defined and can be solved interactively for the pressure. The exhaust area for a long-ducted nacelle can then be calculated with the relations shown in Table 3.2.

3.2.2 Core Exhaust Geometry

The core duct geometry is the first step in the parametric design of the engine. When its height and length are known, it is possible to continue with the bypass duct. The core duct is generated with five design parameters, as shown in Figure 3.5. As mentioned before, the geometry differs depending on the selected type of duct. The exhaust can be convergent or convergent-divergent, and the plug can lay inside or extend outward the core duct. The former is indicated with an additional integer variable. The latter depends on both the plug length and the core cone angle. The core duct adapts for an outer plug if the plug length is longer.

The core duct geometry is constructed with polynomials. It is one of the simplest shape parameterisation methods that can describe a curve in a very compact form with few design variables [35]. The design parameters, as shown in Figure 3.5, allow for the calculation of the end points of a curve. In combination with the angles at the end points, a 3rd order 'clamped' polynomial constructs the curves in the core duct. The angles at the turbine exit are not shown in the figure because they are kept constant. They are set to zero and $\theta_{\mathrm{c}_{\mathrm{cone}}}$ to have a smooth transition from the turbine to the duct.

Figure 3.5 Design variables used to construct the core duct

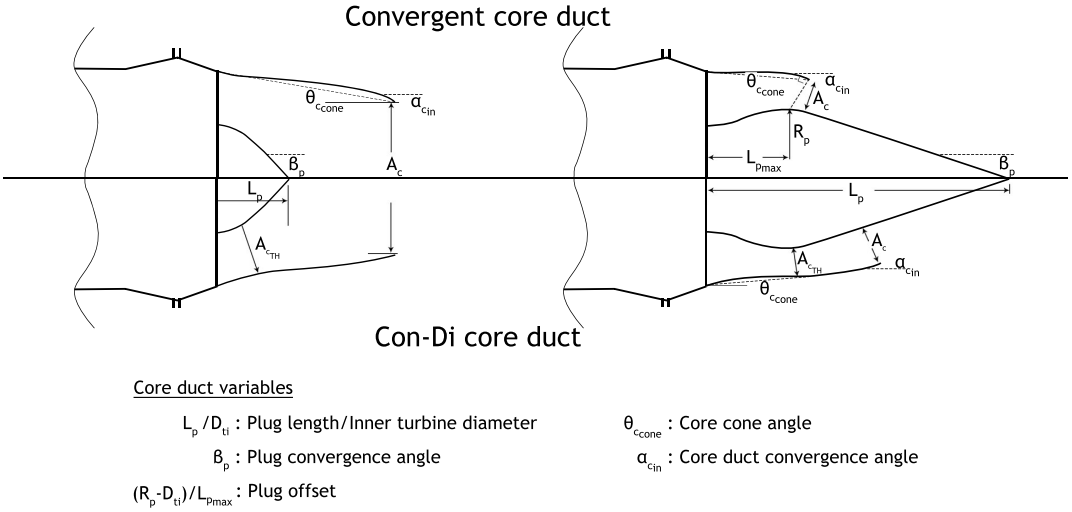

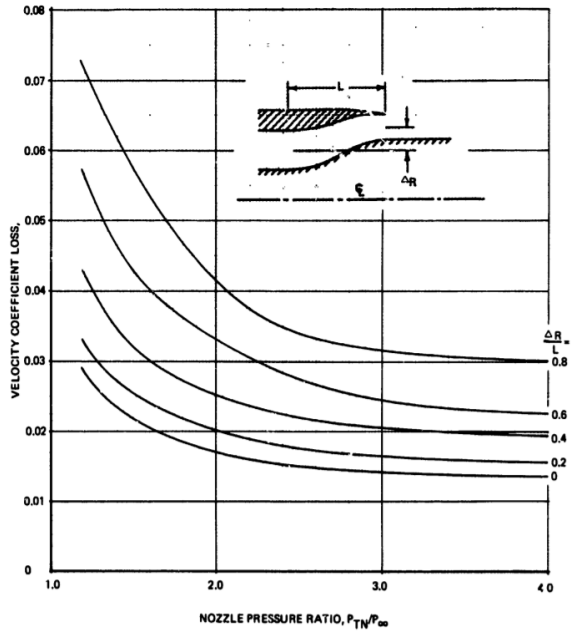

Figure 3.6 Velocity coefficient variation with nozzle offset [33]

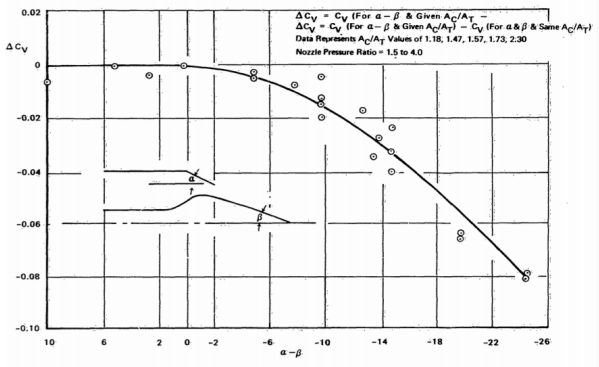

Figure 3.7 Velocity coefficient variation with nozzle wall angle [34]

The polynomial order raises to a 4th order to include the position of the throat in a convergent-divergent duct. This position is determined as the point that has a constant cross-sectional throat area, A_{TH}, from the plug and lies closest to the initial 3rd order polynomial to ensure a smooth geometry.

For a plug outside the core duct, the geometry is specified similarly. It only includes an additional variable to determine the maximum radius of the plug: the plug offset. The location of the core exit is just over the maximum radius to create some overhang. It guides the core exhaust slightly downward. The exhaust can then be aligned better with the fan exhaust to decrease the boattail drag and jet entrainment. Figures 3.6 and 3.7 show the effect of the different angles and offset on the velocity coefficient. It can be concluded from these figures that the duct offset should be kept to a minimum while $\alpha_{\mathrm{c_{in}}}$ should be larger than β_{p} to reduce any duct losses.

3.2.3 Bypass Exhaust Geometry

The bypass duct geometry can be determined once the core duct geometry is known. Whether this should be a long or short-duct is a design choice that depends on multiple factors, such as weight, performance, thrust and drag. The design factor that has a large influence on these factors is the BPR. A high BPR increases the engine diameter. The bypass duct is often shortened to counter the increase in weight this causes. It also decreases the scrubbing drag [11, 45]. When the bypass ratio is lower, the increase in the thrust that can be achieved by mixing the flow in a long-duct might outweigh the reduction in weight with a short-duct. It has as an additional effect that it reduces the exhaust frequency by breaking up the larger eddies into smaller vortices. [45] has made a comparison on the direct operating cost of an aircraft with a short and long-duct nacelle for several bypass ratio engines. In this study, it shows that the break-even point is at a BPR of 3-4. For higher bypass ratio engines a short-duct becomes advantageous. The design parameterisation for both ducts is shown in Figure 3.8. It is possible to analyse bot short- and long-ducted nacelles during the program run. An integer variable indicates the duct type, similar to the exhaust type mentioned previously. Note that the program might eventually converge to one duct type, as it does not take other factors such as weight and viscosity into account.

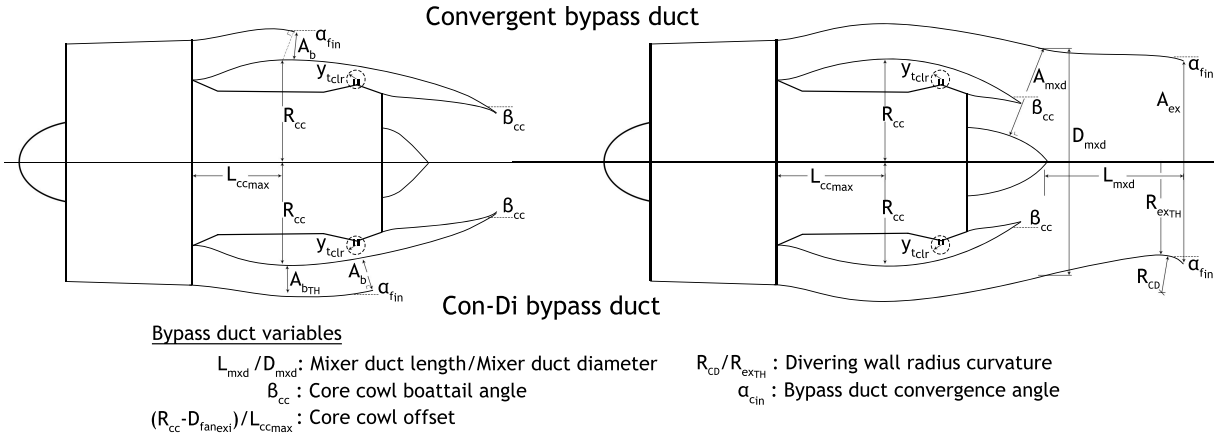

Figure 3.8 Design variables used to construct the bypass duct

The first step in the bypass duct design is the outside of the core cowl since this is independent of the duct type. Two design variables determine this shape: the bypass duct offset and the core cowl boattail angle. As shown previously in Figures 3.6 and 3.7, some offset is beneficial such that it turns the external flow without causing large adverse pressure gradients on the core cowl as long as the turning of the nozzle flow is moderate. The maximum radius is, therefore, calculated with the nozzle offset such that the core cowl fits tightly around the turbine mount. It reduces the maximum radius and the duct length. As soon as this point is known, two polynomials can be constructed for the core cowl.

The construction of the fan cowls' inner contour for a short-duct nacelle is similar to that of the core duct with and outer plug: the exit plane has a small overhang after the maximum radius. A 3rd or 4th order polynomial is used for a convergent and convergent-divergent nozzle, respectively. However, a long-ducted nacelle requires a different method. In this case, the determination of the mixing plane becomes paramount. Since the program does not take viscosity into account, it constructs a simple free mixer configuration, as shown in Figure 3.8. The mixing plane is located on the same plane as the core exit plane. Depending on the shape of the plug, this plane can be tilted under an angle. To prevent large tilting angles, which give unreasonable geometries, a constraint is placed that the mixing plane diameter D_{mxd} should remain larger than the throat diameter.

As soon as the mixing point is known, the remaining tailpipe length can be calculated. This parameter is usually important for the mixing efficiency. [44] contains a mixer study design, where it evaluates the performance of a long-duct nacelle for different lob mixers, tailpipe lengths and mixing plane angles. In this report, $\frac{L_{\mathrm{mxd}}}{D_{\mathrm{mxd}}}$ varies between 0.5-1.0. It shows that a doubling in duct length nearly doubles the mixing level, but that the increase in external skin friction and weight outweigh this effect. Shorter mixing ducts are most advantageous, and since these have a low mixing level they can still be approximated with this parameterisation using Euler CFD calculations within reasonable margins. The diverging section of convergent-divergent long-duct is determined with the wall radius ratio $R_{\mathrm{CD}}/R_{\mathrm{ex_{TH}}}$. This variable determines the longitudinal wall radius at the throat: a higher value will give a large wall curvature R_{CD} and thus a gradual extension towards the exit plane. Smaller ratios will result in shorter ducts but will eventually lead to boundary layer separation. Figures 3.2 and 3.9 show the effect of this variable on the discharge coefficient. The wall radius ratio should not get lower than 1 to prevent large deterioration in the nozzle performance.

The inner fan cowl is then constructed with a clamped spline through the different points. A spline is here preferable over a polynomial because higher-order polynomials are susceptible to oscillations. Care must be taken in the area distribution in the duct, such that the spline creates a gradually increasing or decreasing duct. If this is not the case, a knot is added at this location assuming a linear area distribution.

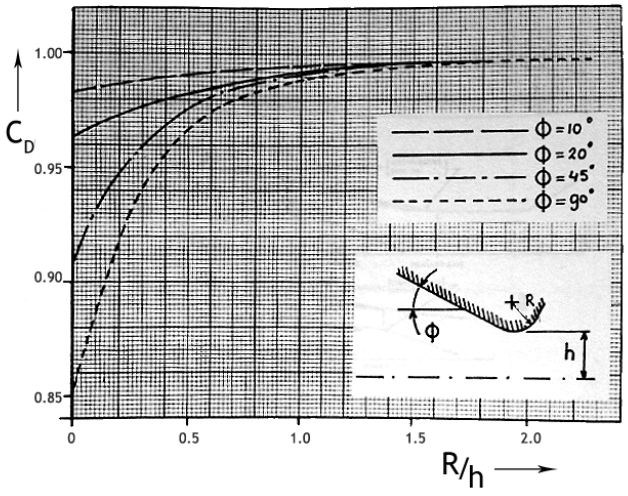

Figure 3.9 Discharge coefficient variation with longitudinal radius [46]

3.2.4 Inlet and Outer Fan cowl Geometry

The geometry of the fan cowl is highly dependent on the operational conditions. The incoming air, indicated by A_∞ in Figure 3.10, changes in size when going from take-off to climb or cruise. As a consequence, the stagnation point and high local velocities can occur anywhere on the inner lip or outer fan cowl. The design of the fan cowl should find the best compromise for the different operational conditions. The design variables used to describe this geometry are shown in Figure 3.10 and divide the geometry up into four curves: the lip, the inlet diffuser, the front fan cowl and the fan cowl boattail.

The first variable, the mass flow ratio, describes the size of the captured streamtube with respect to the highlight area. Its definition is shown in Equation 3.45.

$$MFR = \frac{A_\infty}{A_{\mathrm{HL}}} \tag{3.45}$$

$$A_{\mathrm{HL}} = \frac{\dot{m}}{\rho_{\mathrm{s}} V_\infty \cdot MFR} \tag{3.46}$$

An MFR of 1 would indicate that the highlight area precisely captures all the incoming air that is required by the engine. This is the ideal cruise situation. Often this value lies a little lower, to compromise the performance with windmilling and take-off conditions. Mass flow ratios in between 0.15-0.3 and 2 are reached in these conditions, respectively [9]. This non-dimensional parameter is used as a design variable to calculate the highlight area since the captured streamtube is constant once the cruise conditions are defined. Similarly, the throat area can be determined with the contraction ratio CR, as defined in Equation 3.47.

$$CR = \frac{A_{\mathrm{HL}}}{A_{\mathrm{TH}}} \tag{3.47}$$

Generally, a first design rule is that the one-dimensional throat Mach number should remain below 0.8. Higher values will lead to shock formation near the wall and possibly boundary layer separation. For mass flow ratios below one, the stagnation point is on the inner lip. The favourable pressure gradient over the lip prevents separation. When the angles of attack or mass flow ratios increase, the stagnation point will shift forward or even outward. The maximum Mach number is then at the highlight area due to the extreme curvature at this point [47]. Higher

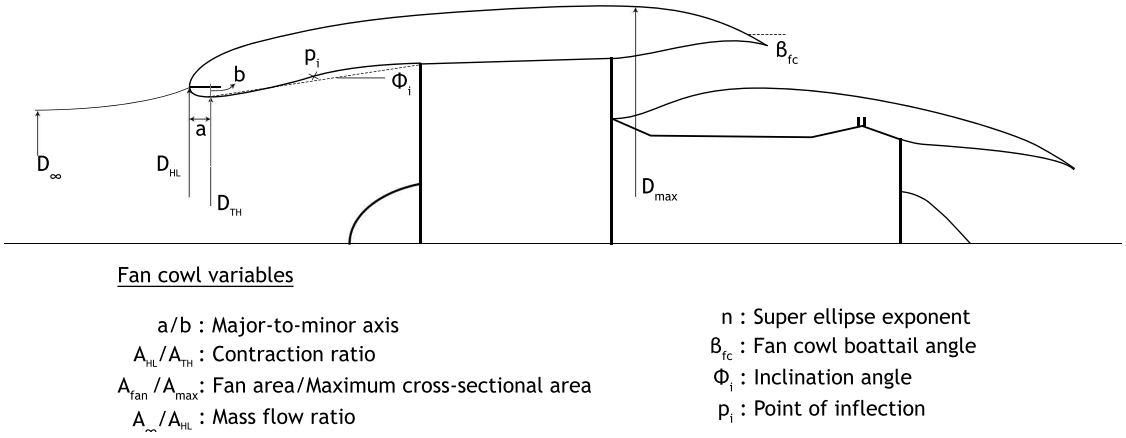

Figure 3.10 Design variables used to construct the fan cowl

contraction ratios will round the curvature and improve pressure recovery in these conditions. Take-off, in particular, is the most difficult condition because both high mass flow ratios and angles of attack occur in this condition. A common shape to describe the lip is the super-ellipse, which has been used in, for example, the NACA-1 and DAC-1 contours [11, 48]. The formula for the super-ellipse is shown in Equation 3.48.

$$1 = \left(\frac{x}{a}\right)^n + \left(\frac{y}{b}\right)^n \qquad [11,\ 47] \qquad (3.48)$$

[47] experimentally researched the effect of the contraction ratio, major-to-minor axis and lip exponent at different speeds and angles. They concluded that an a/b ratio of 2 gives the lowest peak Mach number and local Mach number gradient, though slightly higher values improved the circumferential Mach number gradient. Moreover, the exponent n can be used to control the peak Mach number by changing the lip's bluntness. By varying this value between 1.75-2.5, it found that n has to increase with increasing values of a/b to minimise the Mach number gradient. [47] recommends an initial value of 2 for both a/b and n.

Now that the throat area is known, the diffuser can be determined. The diffuser length depends on the wall inclination angle. This angle is a useful design parameter, as it can be closely related to the pressure recovery.

$$L_{\text{diff}} = \frac{D_{\text{fan}} - D_{\text{TH}}}{2\tan\phi_i} \qquad (3.49)$$

Beyond a certain inclination angle, it becomes impossible to have natural flow expansion and separation will occur. Figure 3.11 shows the experimental data for a conical diffuser of different lengths, area ratios and inclination angles. A maximum angle of 6° is possible before separation occurs, but this reduces as the angle of attack is raised [49]. The same trend is seen for an increasing throat Mach number of decreasing flight speed. The diffuser contour also plays a role in the pressure recovery of the diffuser. In [49], the inflection point is varied in between 25, 50 and 75% of the diffuser length. It proved better to diffuse the air rapidly in the first part of the diffuser. At a Mach number of 0.12 and an angle of attack of 40°, separation would occur for inflection points higher than 50%.

The fan cowl boattail is approximated by a circular arc as these perform better than conical afterbodies [38, 50]. The most influencing parameters of the boattail are the diameter ratio $D_{\text{b}}/D_{\max}$ and the boattail angle β, as shown in Figure 3.12. Note that the exit diameter D_{b} depends on many other variables, in contrast to the maximum diameter $D_{\max}$. [50] investigated the influence of these parameters on the base pressure coefficient and boattail drag coefficient for the jet-off case. Both drag contributions decrease with increasing diameter ratio, as the reduction in tapering causes a smaller adverse pressure gradient. This can be reached by either lowering the maximum diameter or raising the duct's offset, but this causes additional bypass duct pressure losses.

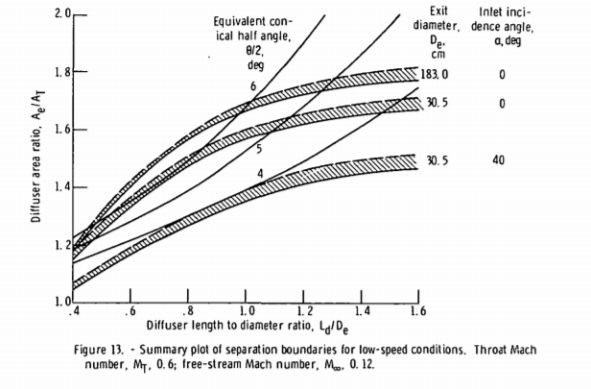

Figure 3.11 Diffuser separation angle at M_∞ =0.12 and M_{TH} =0.6 [49]

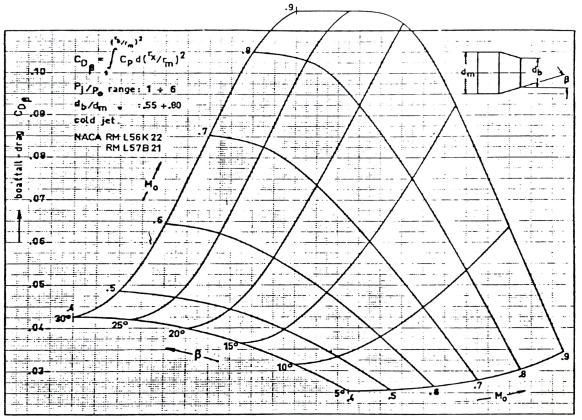

Figure 3.12 Boattail drag variation with boattail angle [11]

The boattail drag also increases with increasing boattail angle, though for the base drag an optimum boattail angle of 20°-24°is found for Mach numbers below 0.9 [50]. Often, a boattail angle of 15° is used as a compromise and to reduce the fan cowl length [11, 38]. In some cases, a circular boattail is not possible without intersecting the fan clearance requirement or the bypass duct. This situation is depicted in Figure 3.13. A combination of several parameters gives a circular boattail section that crosses through either the bypass duct's contour or the fan clearance requirement. Only in this specific case is the position of the maximum diameter placed further aft. The minimum angle that still satisfied the constraints is used to determine the new position. A 4th order polynomial then constructs the boattail.

The last curve is the front fan cowl. A semi-cubic parabola is used to construct this curve, for which the formula is shown Equation 3.50 [38, 48]. The second derivative at the maximum diameter should be within the range shown in Equation 3.51 to prevent imaginary results.

$$y = \sqrt{a + bx + cx^2 + dx^3} \qquad [38] \quad (3.50)$$

$$\frac{-3}{2}\frac{D_{\max} - D_{\mathrm{HL}}}{2x_{\max}^2} \geq f''_{A_{\max}} \leq 0 \qquad (3.51)$$

Figure 3.13 A 4th order polynomial instead of a circle segment is used for the boattail if certain requirements are not met

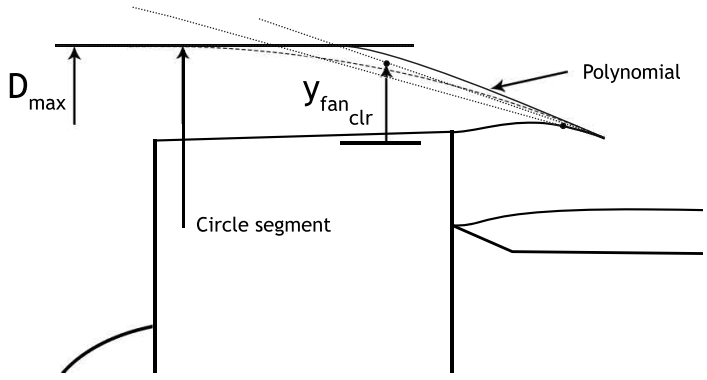

3.3 Computational Fluid Dynamics

During this project, each nacelle geometry is evaluated with respect to two flight conditions: take-off and cruise. See Sections 3.4 and 4.1 for more details about the GA algorithm and flight conditions. Two CFD simulations are needed to obtain the forces working on the nacelle in each flight condition. However, multiple nacelle geometries need to be evaluated to search the design space and find the Pareto front. It becomes quickly computationally expensive. Therefore, three assumptions simplify the CFD simulations:

2D This assumption greatly reduces the computational time, as a smaller and less complex grid is needed. However, it neglects the three-dimensional flow effects that occur, amongst others, in the nozzles.

Axisymmetric To further reduce the grid and flow complexity, an axisymmetric nacelle is assumed. Of course, a real nacelle is not perfectly axisymmetric. The sides and bottom of the nacelle often have different camber and nacelle thicknesses. The inlet is drooped and scarfed to align the flow better. However, an asymmetry assumption also requires a zero incidence flow. The incoming airflow has a very small angle during cruise and at the start of the take-off phase. The use of droop, scarfing and change in thicknesses of the cowling is used to counter this effect. The behaviour is assumed similar to a fully axisymmetric nacelle and flow condition.

Inviscid The inviscid flow equations neglect friction, thermal conduction and mass diffusion. It is unable to calculate the boundary layer growth, and eventually, the flow separation. The flow after separation is turbulent and fully three-dimensional. Thus not only the friction but also the interaction of the different flow streams at higher flight speeds will be vastly different. The friction drag is instead estimated with the empirical equations in Section 3.1.3 to partly counter this assumption.

Before the actual simulation can be started, several other steps need to be taken. Firstly, the nacelle geometry and the flow domain around it needs to be discretised. The meshing of the domain is explained in Section 3.3.1. The boundary conditions and model settings are further explained in Section 3.3.2.

3.3.1 Meshing

To gain reasonable answers from the CFD analyses, a proper defined domain is needed. Several decisions on the program, domain size, mesh type and structure have to be taken.

The optimisation uses ICEM CFD as a meshing tool. This program allows for easy automation of the meshing progress. Predefined commands can be gathered in a text file and executed in the background for each nacelle. This text file can be accessed and adapted easily from Matlab during this process. The geometry itself is loaded into ICEM CFD as formatted data points sets. The formatted data point input contains the x, y and z points of the generated nacelle contours. A fourth line tells ICEM CFD the number of points to use for the generation of one line. ICEM CFD then constructs a B-spline through these points. The data points are defined up to five decimals, and the approximation tolerance was set to 10^{-5} to ensure that the B-spline can approximate the nacelle contour. This precision was especially necessary at the nacelle lip.

The shape and size of the domain influence the computations. A domain must be large enough to prevent that the boundary conditions influence the flow around the nacelle, but larger meshes are computationally expensive. Stańkowski et al. [51] performed a domain-independence study on two axisymmetric nacelle configurations. It recommends a circular domain with a radius of $60{\cdot}D_{\max}$ to prevent large spurious effects. The drag coefficient found for this domain remained within 0.1% of the largest domain ($150{\cdot}D_{\max}$ radially) considered. Also in [52], a domain size of at least 50 diameters radially was used. For this reason, the domain size of $60{\cdot}D_{\max}$ was deemed accurate enough while remaining low in computational complexity. However, the grid was switched from an O-grid to a C-grid of the same size to simplify the generation of a structured mesh. In a structured mesh, the cells are topologically similar and aligned with the flow. This reduces the required memory and time and improves the

convergence rate [53]. As each mesh is evaluated for two different flow conditions, the disadvantage of a slower grid generation is surpassed by the advantages. The C-grid proved to have a slightly better mesh quality, as it reduced the cell's skewness and was more easily adaptable to the different nozzle types.

The meshing is done using blocks. A C-grid is used around the geometry with an additional C-grid around the fan cowl. Refinement of the mesh is limited to the regions around the nacelle. Nevertheless, boundary layer refinement is not of interest for Euler computations. The vertical spacing around the nacelle is constant to keep the mesh as uniformly as possible and keep a smooth transition in the mesh of different blocks. Figures 3.14 and 3.15 shows the mesh around a short- and long-duct nacelle. Eight different text files are created for ICEM CFD for each type of nacelle since a divergent duct or an outer plug require an additional block. However, the meshing in the other blocks remains nearly the same.

Figure 3.14 Mesh around a short-duct nacelle

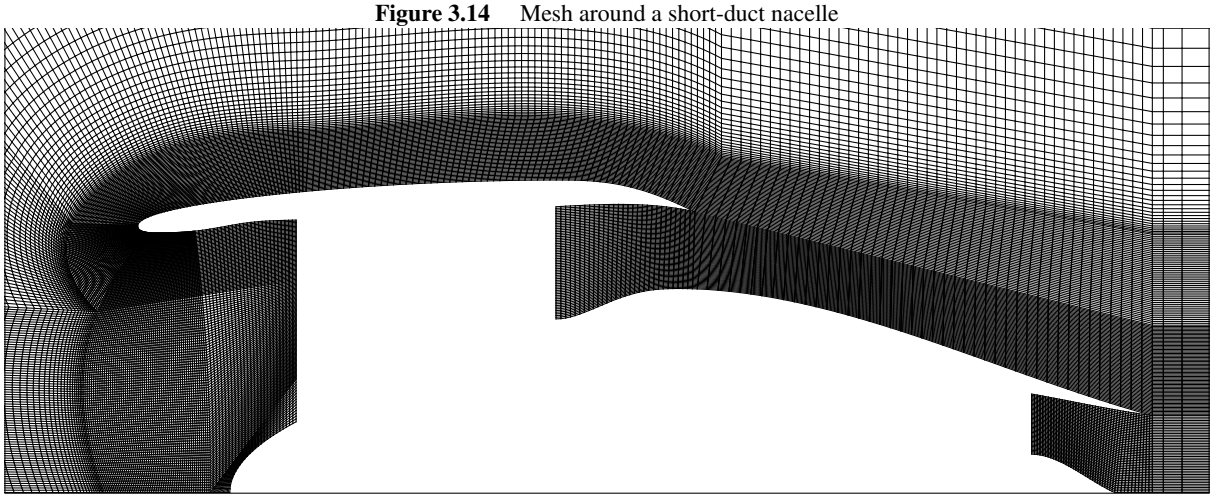

Figure 3.15 Mesh around a long-duct nacelle

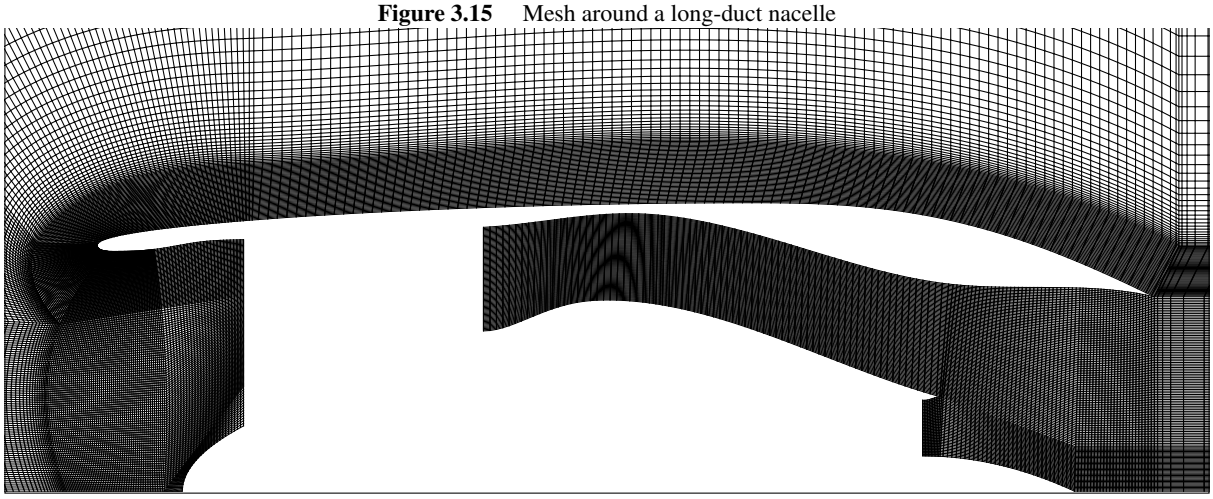

3.3.2 Model Set-up

The ANSYS Fluent software is used to solve the CFD problem. The 2D mesh was exported from ICEM CFD and imported into Fluent. However, before the simulation can be started, boundary and convergence conditions need to be imposed. These settings are discussed in the upcoming sections.

3.3.2.1 Solver schemes

As mentioned previously, the model uses an Euler inviscid scheme. It requires a few additional solution method settings. Firstly, a solver method needs to be selected. Historically, a density-based solver is used for high-speed compressible flows while a pressure-based solver is used for subsonic flows. Nowadays, both solvers are used for all types of airflows. The density-based solver was investigated but showed a slower convergence rate. The different mass flow boundaries often caused divergence problems, and this was more stable using a pressure-based solver. The pressure-based solver was used in its coupled form, as this improves the convergence rate over a segregated pressure-based solver [26].

Fluent stores all the discrete values at the cell centres. These need to be interpolated to obtain the cell face values. Different spatial discretization schemes are available in Fluent. Since the flow is compressible, at least a second-order scheme is needed, in which case the QUICK and the third-order MUSCL schemes are the most accurate. The QUICK scheme has been selected, as it produces better results over shockwaves than the third-order MUSCL [26].

3.3.2.2 Boundary conditions

On all boundaries, the initial flow conditions need to be set before any CFD model can be started. Figure 3.16 shows the sketch of the fluid domain and the respective boundary settings.

Several boundary conditions can be defined by Fluent, though some are limited to (in)compressible flow. In this case, pressure boundary conditions are needed at the inlet and outlet to simulate a compressible flow correctly. A pressure far-field boundary condition is placed at the inlet to model the freestream conditions with the predefined Mach number. Similarly, a pressure outlet is specified at the outlet boundary. This requires the static gauge pressure and total temperature conditions. In both cases, the gauge pressure remains at zero, and the operating pressure is set to the freestream static pressure. Any static pressure in the CFD results is therefore directly presented for the freestream pressure, thus $P_{\mathrm{s}_{\mathrm{CFD}}} = P_{\mathrm{s}} - P_{\infty}$.

Figure 3.16 Sketch of the CFD domain and the applied boundary conditions

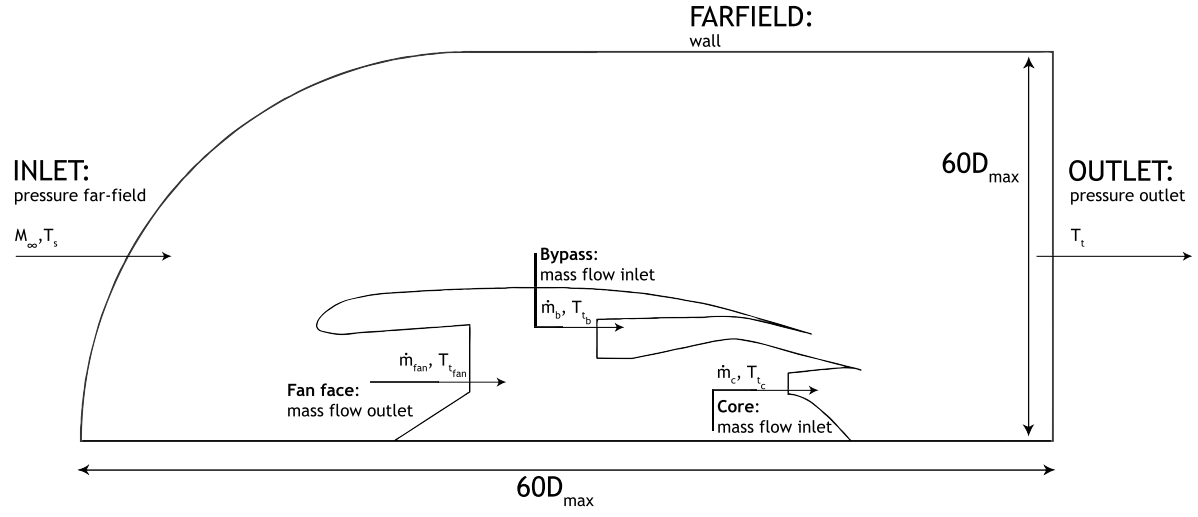

Fluent treats all nacelle contours as walls, except for the fan face, fan exit and turbine exit. To simulate the suction and expelling of air, these are modelled as mass flow boundaries. The mass flow conditions follow from the cycle design, as specified in Appendix C. Fluent determines the other flow conditions from this mass flow. This boundary represents the ideal situation, as the specified mass flow is always reached independently of the upstream conditions. If part of the flow separates at the upper inlet wall due to very high Mach numbers over the throat, it does not impact the mass flow at the fan. Instead, the flow accelerates at another region of the boundary, so that the condition M<0.6 does no longer hold. Moreover, the mass flow condition requires a specified direction, which is enforced over the complete boundary. The outwards normal option is used at the fan face. It causes the flow to act more as an outflow, as fluxes are allowed to vary across the domain such that the flow profile is kept intact. The normal to boundary option is used at the bypass and core. This is identical to specifying purely axial incoming flow since the fan is placed under a 90°angle to the centerline.

3.3.2.3 Convergence settings

The CFD simulations are automated and run in batch mode to reduce the computational cost of the program. That means that the solver runs for a predefined number of iterations, without knowing if the flow has converged. A sufficiently large number of iterations needs to be set to allow convergence of the different nacelle geometries. However, a too large number will be time-consuming. The maximum number of iterations is, therefore, set to twice that of the initial nacelle, namely 500. This number depends on the convergence settings, which are discussed in this section.

The first necessary convergence settings are on the residuals. These are considered converged if they fall below the threshold of 10^{-5}. Fluent's residual convergence settings are lower, at $2.5 \cdot 10^{-6}$, so that the solution can stabilise within this margin. The last 50 iterations are used to check the stability of the solution. For these iterations, the fluctuation of the drag coefficient is monitored. The average value over the last 25 and 50 iterations and the standard deviation should differ less than 0.1%. This is mathematically described in Equations 3.52 and 3.53.

$$\frac{\overline{C_{d_{50}}} - \overline{C_{d25}}}{\overline{C_{d25}}} \leq 10^{-3} \quad [54] \quad (3.52)$$

$$\frac{\sigma_{50}}{\overline{C_{d25}}} \leq 10^{-3} \quad [54] \quad (3.53)$$

3.4 Optimisation Algorithm

The type of optimisation technique determines partly the design space and how fast it finds a solution. During the literature survey, several optimisation methods have been compared to see which optimisation would apply to the current design problem. Since the nacelle geometry varies a lot with different flow conditions and the requirements are often contradictory to each other, a multi-objective formulation could be advantageous. It allows the designer to analyse the effects of the different variables on several conditions and choose the best compromise. It was decided to opt for a Pareto-based Evolutionary Algorithm (EA), namely the NSGA-II algorithm. These terms are further explained in Section 3.4.1. The algorithm logic is shortly explained in Section 3.4.2.

3.4.1 Evolution Algorithms Definitions

Evolutionary Algorithms (EA) is a class of global optimisation algorithms. Instead of evaluating one geometry and searching for a new geometry based on its results, a global optimisation algorithm evaluates multiple geometries in parallel. The best set of solutions is adjusted to generate the next set of solutions, or population, in search of a global optimum. As such, they can be applied to any optimisation problem. It was initially invented for natural evolution problems and these terms are still used.

Individual An individual is a set of parameters that contains a single solution to the problem. It can be seen as a vector $\bar{x}$ containing a unique set of values for the design variables.

Population A group of multiple individuals forms a population. Thus, a population of the size N contains the set $\{\bar{x}_1, \bar{x}_2, ...\bar{x}_N\}$ of individuals.

Generation One generation is a single population set. Once the first population has been analysed, a new population is generated based on the results of each individual. This is called the second generation. This can be continued for any G number of generations.

Fitness The fitness value is the value of the objective function for each individual. The best individuals are then more likely to be used for the creation of the next generation.

Pareto-based Pareto-based algorithms assign a ranking to each solution rather than using the objective values, as a rank is easier for algorithms to work with. The rank is dependent on the number of solutions an individual dominates. The lowest rank is assigned to the best individuals, i.e. the individuals closest to a Pareto front.

Elitism It is not always certain that the next generation performs better than the previous. These individuals are lost if nothing is done. Elitism ensures that the best-ranked individuals survive to the next generation. That can be done by copying them directly into the next generation, but this can cause premature convergence. Therefore, it is also possible to store them in a separate archive and maintain diversity in each generation.

Archive An archive contains the set of the N best individuals. After each generation, the new individuals are compared to the individuals in the archive. The new individuals that have a better fitness value will replace the lowest valued individuals in the archive so that its size remains the same. This set is then used to create the next generation.

A typical EA algorithm exists of 3 things: a population generator, a fitness estimator and three basic genetic operators [55]. The population generator creates the first generation within the selected bounds, whereas the fitness estimator determines the objective values for each individual. The next generation is created by a combination of crossover, mutation and selection. Selection does not evolve the next individual, but individuals are simply kept and transferred to the next generation. With crossover and mutation, new individuals are created: two individuals are selected from the current generation, the parents, and used to create two new individuals, the children, for the next generation. Crossover is accomplished by recombination of the design variables of its parents. With mutation, random changes are applied to the parents to broaden the search space. The Mutation is more useful in the initial generations and for smaller populations [55]. There are different mutation and crossover functions depending on the used algorithm.

3.4.2 Nondominated Sorting Genetic Algorithm II

A subclass of EA is the genetic algorithms (GA). The opted Nondominated Sorting Genetic Algorithm (NSGA) is one of these algorithms. As the name suggests,it uses nondominated sorting to determine the best solutions among a population. Moreover, it incorporates a method to find multiple Pareto points simultaneously. NSGA-II is an improvement of NSGA by incorporating an elitist algorithm.

The basic steps that the algorithm follows are shown in Figure 3.17. The search starts with a population set P of N individuals. This population is generated randomly within the applied variable bounds values and linear constraints. The light blue blocks in Figure 3.17 are the specific steps taken in this project on each individual. After the geometry is determined and a CFD analysis is performed, the nonlinear constraints are checked. The algorithm has difficulty finding new points in the design space if the constraints are too strict since the objective values are calculated only for individuals for which all constraints are satisfied. The population and archive are combined to one set of $2N$ individuals after every individual in the population is analysed. The rank and crowding

distance are determined for the new set, after which the best N individuals are stored back in the archive. The crowding distance is used to ensure that all individuals maintain a widespread on the Pareto front. An individual with a larger crowding distance scores therefore better than an individual with a smaller crowding distance of the same rank.

A new population is generated using crossover and mutation on the design vectors stored in the archive. Thus, only the best sets of ranked solutions are used to keep the optimisation close to the Pareto-front. Matlab's function *gamultiobj* is based on the NSGA-II program. However, this program does not allow integer variables. A custom crossover and mutation function based on [56] is used to incorporate integer variables. This uses a linear crossover function, as shown in Equation 3.54.

$$child_1 = \frac{1+\beta_{cr}}{2} \cdot parent_1 + \frac{1-\beta_{cr}}{2} \cdot parent_2 \quad [56] \quad (3.54)$$

$$child_2 = \frac{1-\beta_{cr}}{2} \cdot parent_1 + \frac{1+\beta_{cr}}{2} \cdot parent_2 \quad [56] \quad (3.55)$$

β_{cr} is the spread factor in this equation. If $\beta_{cr} < 1$, then the design variable will lie somewhere between their parents' value and the solution will be contracting. If it is higher, the solution will be expanding. Due to the fraction, $child_1$ will lie closer to $parent_1$ and $child_2$ will be closer to $parent_2$. Whether the spread factor is contracting or expanding is decided randomly by the variable u, as shown in Equation 3.56. The variable η_{cr} can be specified beforehand to influence the spread factor. The larger the value, the closer β_{cr} is to 1 and the closer the children will be to the previous population.

$$\beta_{cr} \begin{cases} (u \cdot \alpha_{cr})^{\frac{1}{\eta_{cr}+1}}, \text{ if } u \leq \frac{1}{\alpha_{cr}} \text{ (Contracting)} \\ (u \cdot \alpha_{cr})^{\frac{-1}{\eta_{cr}+1}}, \text{ if } u > \frac{1}{\alpha_{cr}} \text{ (Expanding)} \end{cases} \quad [56] \quad (3.56)$$

Where:

$$u = \textit{random } [0,1] \quad (3.57)$$

$$\alpha_{cr} = 2 - \left(1 + \frac{2 \cdot \textit{min distance to bound}}{|parent_1 - parent_2|}\right)^{(-1-\eta_{cr})} \quad (3.58)$$

Mutation applies random changes to the previous population to broaden the search space. The parents that are not used for crossover are used for mutation. The used mutation operator is shown in Equation 3.59. Whether the mutation value lies closer to the upper or lower bound depends on the mutation factor β_m. Again a mutation variable, η_m, can be used to influence the spread. The larger the value, the closer β_m is to 0, and the less the parent is mutated. The Matlab scripts for both functions are included in Appendix A and B.

$$child_1 = Parent_1 + \beta_m \cdot (\textit{Upper bound - Lower bound}) \quad [56] \quad (3.59)$$

Where:

$$\beta_m \begin{cases} -1 + \left(2u + (1-2u) \cdot (1-mut)^{\eta_m+1}\right)^{\frac{1}{\eta_m+1}} & \text{, if } u \leq 0.5 \text{ (Negative)} \\ 1 - \left(2(1-u) + (2u-1) \cdot (1-mut)^{\eta_m+1}\right)^{\frac{1}{\eta_m+1}} & \text{, if } u > 0.5 \text{ (Positive)} \end{cases} \quad (3.60)$$

$$u = \textit{random } [0,1] \quad (3.61)$$

$$mut = \frac{\textit{min distance to bound}}{\textit{Upper bound - Lower bound}} \quad (3.62)$$

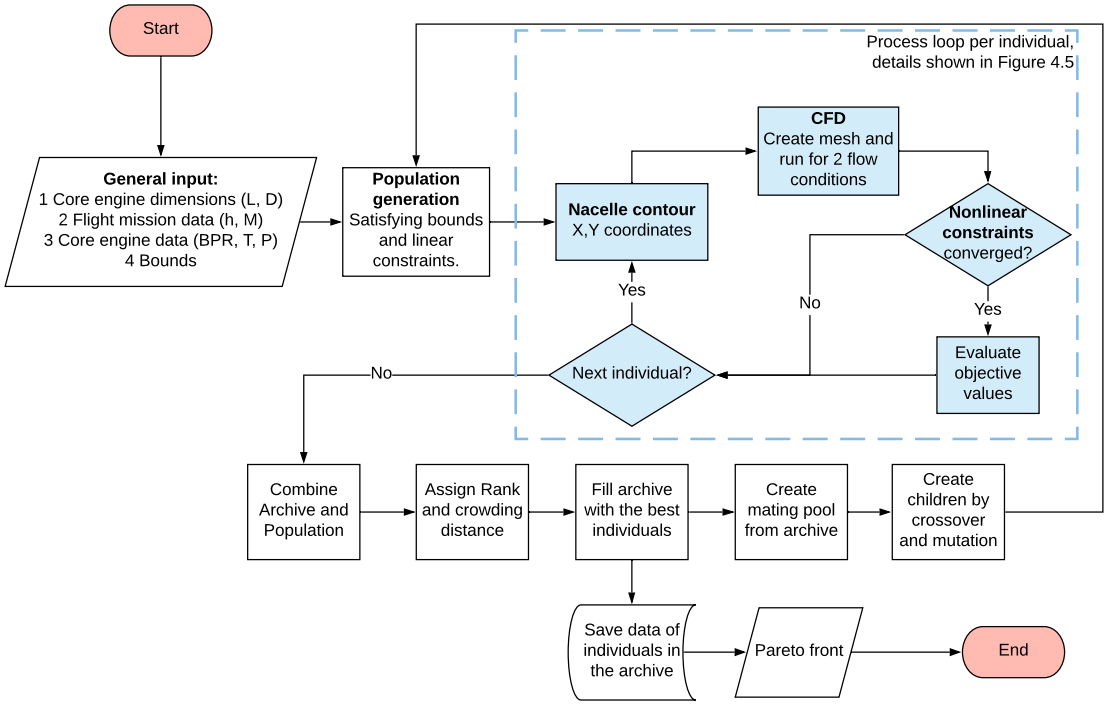

Figure 3.17 NSGA-II algorithm steps taken per generation

4 MODEL STRUCTURE

The program can not be started with just the parameters. The design space would be so large that the search for the Pareto front will be time-consuming, and a large part of the evaluated individuals would not be realistic. Constraints and bounds are needed to constrict the design space. The choice for these are explained in Section 4.4 and 4.5 respectively. In addition to the constraints, it is also possible to define one or several individuals of the initial population, so that they are not generated randomly. A good starting process can accelerate the search process. The geometry used as a starting point is described in detail in Section 4.1.

4.1 Test Case Conditions

Both the geometry and operational conditions must be known to use a nacelle for verification. This is difficult, as hardly any data is available on the current nacelles geometry. In the past, the NACA-1 profiles were used for the cowling and adjusted to get the desired geometry. The engine technology has evolved since then and changed too much to apply it to the current technology. Instead, the data from the slightly older report [38] from 1985 has been used. It is part of NASA's Energy Efficient Engine (EEE) program, which developed new engine turbofan technologies to improve the specific fuel consumption. This report analyses new nacelle configurations with the combined use of an axisymmetric Euler computation, experimental data and semi-empirical relations. Although the EEE never went into production, the developed technology has been used widely in the current generation engines. The STF653 configuration from this report is used for the verification of this program. It has a high bypass ratio of 12.8 and dimensions similar to current engines, such as the PW1100G used on the A320neo. The configuration data is further described in Section 4.2 and 4.3.

As mentioned previously, the nacelle's performance is tested for two flow conditions: cruise and take-off. The first choice is logical; it encompasses the largest part of the flight, and it should work optimally to reduce drag and fuel. The take-off condition is chosen for several other reasons. Firstly, the requirements for this condition are often conflicting with the cruise requirements, especially for the inlet. Secondly, the required mass flow and thrust are the largest during take-off, even though the relative freestream velocity is low. These requirements also hold during climb, but due to the angles of attack, this can only be analysed with a viscous two-dimensional grid to capture the important separation points. It would drastically increase the computational time. The conflicting flight conditions hopefully show a clear Pareto front with different optimal geometries for each condition. The aerodynamic conditions are summarised in Table 4.1.

The cruise conditions are identical to those in [38]. These are typical cruise conditions as the cruise Mach number ranges between 0.75-0.85. A low Mach number during take-off is more demanding as this increases the MFR. However, a zero or very low freestream velocity is not possible in Fluent as this gives convergence issues. A Mach number of 0.1 is therefore selected: this is halfway the take-off Mach number range (M_∞ = 0-0.25). This point would give a MFR of 4.2. However, other take-off conditions can also be selected. Two other cases are run to show how the take-off condition influences the optimum geometry and the Pareto front. The first is for a

Table 4.1 Aerodynamic test conditions

		First test condition			Second test condition		
Case number	Duct type	$h\ [m]$	M_∞	$\Delta T_{\text{sISA}}\ [^\circ C]$	$h\ [m]$	M_∞	$\Delta T_{\text{sISA}}\ [^\circ C]$
1	Short	10670	0.8	0	0	0.1	0
2	Long	10670	0.8	0	0	0.1	0
3	Short	10670	0.8	0	0	0.2	0
4	Short	10670	0.8	0	1655	0.1	26

higher take-off Mach number, at the end-of-runway take-off conditions. The other case is the hot & high engine condition. Having both a higher temperature and altitude reduces the air density and the engine's performance. The air conditions of Denver's airport are taken for this case. This airport is located at a high altitude and can reach temperatures around 31°C in the summer [57]. It is almost 26°C higher than the ISA conditions at this altitude. Note that for all cases, the same cruise conditions are used. Cruise is often the main condition for which turbofans are designed. Moreover, it ensures that the same starting design vector and geometry is used.

4.2 Fixed parameters

A nacelle is influenced either by the design parameters such as the nacelle length and boattail angle, or the engine conditions such as the BPR, exhaust pressure and temperature. The latter parameters change with the flight phases and have to be determined for both flow conditions. However, once known, they are kept constant during the program run. The first part of the constant parameters includes the core engine dimensions for which the nacelle needs to fit. The second part are the engine cycle conditions during take-off and cruise. They are explained in Section 4.2.1 and 4.2.2 respectively.

4.2.1 Engine Dimensions

The required core engine dimensions, as discussed in Section 3.2.1, are retrieved from [38]. The engine length, fan casing length and fan diameter are stated explicitly. The hub to tip ratio is given in [58] as 0.26. The exit diameters and turbine length, however, are not specifically mentioned. These are scaled and tuned to fit the given contour. As shown in Figure 4.3, these core engine dimensions are nearly identical. The actual values of all the dimensions are shown in Table 4.2. The last row includes the space requirements that can be set for the fan casing and turbine mount [38]. These are taken directly into account when the nacelle contour is constructed. The relative location of the fan clearance requirement is not known. It is assumed midway the fan case to cover the complete fan case.

Table 4.2 Core engine geometry variables

	Geometry variables										
Parameters	L_{fan}	D_{fan}	$D_{\text{fan}_{\text{exo}}}$	$D_{\text{fan}_{\text{exi}}}$	R_{hub}	L_{hub}	L_{eng}	D_{tm}	L_{tm}	D_{ti}	D_{to}
Value [m]	1.29	2.71	2.85	1.73	0.35	0.33	3.66	1.19	0.29	0.38	0.98
	Clearance requirement variables										
Parameters	$y_{\text{fan}_{\text{clr}}}$	$f_{\text{fan}_{\text{clr}}}$	$y_{\text{t}_{\text{clr}}}$								
Value [m]	0.127	0.5	0.0254								

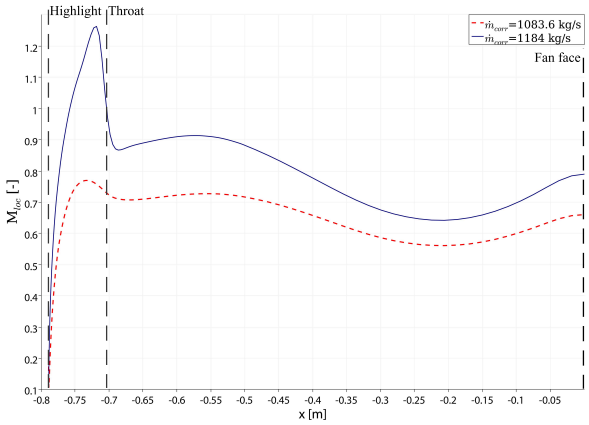

Figure 4.1 Local Mach number distribution on the inlet wall for different mass flows at cruise ($h = 10670\ m$, $M = 0.8$)

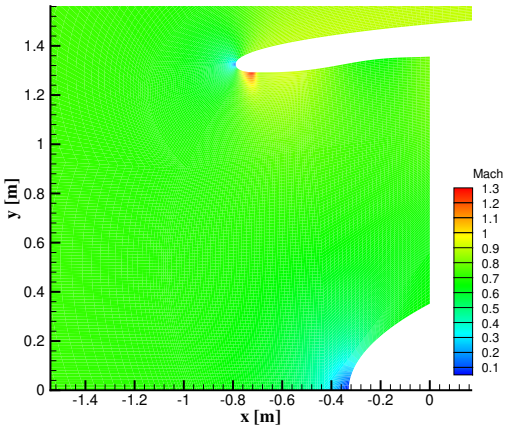

Figure 4.2 Mach number contour plot for $\dot{m}_{\text{corr}}$=1184 kg/s at cruise ($h = 10670\ m$, $M = 0.8$)

4.2.2 Turbofan Engine Cycle Design

Cycle data is only scarcely available to the public. The test engine data from [38] and [58] only give a few variables in cruise, such as the BPR, FPR, $\dot{m}_{\text{corr}}$ and the velocity and pressure ratios between the core and bypass. This would cover most of the necessary input data, except that the conditions apply to the maximum cruise conditions. The specified corrected mass flow of 1184 $\frac{kg}{s}$ results in an average fan Mach number far above the 0.6 threshold, namely 0.69. Only the mass flow could be lowered to meet this threshold while keeping the same inlet geometry. The one-dimensional Mach number can be calculated with Equation 4.1. This gives a corrected inlet mass flow of 1083.6 $\frac{kg}{s}$, which is the same as a mass flow $\dot{m}$ at take-off conditions of 420 $\frac{kg}{s}$.

$$A = \frac{\dot{m}\sqrt{T_{\text{t}}}}{P_{\text{t}}}\sqrt{\frac{R}{\gamma}}\frac{\left(1+\frac{\gamma-1}{2}M^2\right)^{\frac{\gamma+1}{2\gamma-2}}}{M} \tag{4.1}$$

The local Mach number over the inlet is plotted for both mass flows in Figure 4.1. A larger mass flow causes a steep rise in Mach number over the lip, which terminates with a shock at the throat. This peak is visible in Figure 4.2. Though the average Mach number remains here below 0.8, the strength of the shock could lead to separation and negatively affect the pressure recovery and fan blade loading. Reducing the mass lowers this peak and creates a flatter velocity profile. This is not surprising, as the highlight area and fan area are relatively close.

With this new mass flow, the engine cycle has to be updated. This is created using GasTurb 12. The different engine cycle analysis in cruise and take-off are included in Appendix C. The cruise cycle is tuned to give the same cycle parameters as specified in [38, 58], and the main engine parameters are summarised in Table 4.3. However, the change in cruise mass flow gives a lower thrust and exhaust area than the reference engine. This difference is the largest at the bypass duct, as shown in Figure 4.3. It was verified that increasing the mass flow to the reference value of 1184 $\frac{kg}{s}$, gives the same fan cowl contour as the reference engine.

GasTurb is also used to evaluate the three off-design points. This gives the cycle data included in Appendices C.3-C.5. The thrust at a Mach 0.1 sea-level conditions is not known, but [38] specifies the maximum take-off thrust and the thrust at Mach 0.2. As a compromise, the cycle for Mach 0.1 has been iterated until the thrust is in between the specified conditions.

Table 4.3 Test engine cycle data

Parameters	$\dot{m}_{\text{corr}}$	$\dot{m}_{\text{fuel}}$	BPR	FPR	P_{t_5}	T_{t_5}	γ_{g}	C_{p}	η_{fan}
Unit	$\frac{kg}{s}$	$\frac{kg}{s}$	-	-	kPa	K	-	$\frac{kJ}{KgK}$	-
Cruise	1083.6	0.63	12.8	1.53	43.1	647	1.33	1150	0.92
Take-off case 1&2	971.6	1.57	12.8	1.46	129.7	747	1.33	1150	0.94
Take-off case 3	972.4	1.57	13.1	1.45	129.7	745	1.33	1150	0.95
Take-off case 4	898	1.10	13.6	1.39	100.4	767	1.33	1150	0.94

4.3 Initial design variables

Most of the design variables follow directly from the reference nacelle data in [38]. This includes the main diameters and duct lengths, as shown in Table 4.4. These need to be converted to the specified design variables.

The inlet design variables can be calculated with the data in this table and the cruise mass flow in Table 4.3, thus A_∞. The MFR, CR, $\frac{a}{b}$ and $\frac{A_{\text{fan}}}{A_{\max}}$ ratios can be calculated with the specified diameters. The diffuser angle ϕ_i is calculated with the use of Equation 3.49. The only remaining unknowns are n and P_i. The influences of these parameters have been explained previously in Section 3.2.4. The ellipse exponent n is closely related to $\frac{a}{b}$, which has a relatively high value. n is therefore raised to 2.5 to follow the blunt lip of the initial nacelle geometry. Lastly, P_i could not be determined directly because the inlet diffuser of the reference nacelle is constructed differently, with multiple line segments. P_i is assumed at 0.5 to approximate the contour. The fan cowl, the red line in Figure 4.3, overlaps the STF653 nacelle almost completely.

The largest difference however, becomes apparent at the ducts. This difference is caused by the use of a rounder third order polynomial and slightly smaller exhaust areas. However, the rounder boattail is kept, because it showed a slightly weaker shock and thus a reduced pressure and friction drag. The nozzle parameters $L_{\text{p}}/D_{\text{ti}}$ and $\theta_{\text{c}_{\text{cone}}}$, could be determined from the known duct lengths. Also β_{fc} could be calculated from the position of the maximum nacelle diameter, using a circular arc segment for the boattail. The other variables are tailored to keep the difference in the bypass duct geometry minimal. The initial design vector is summarised in Table 4.5.

Table 4.4 Reference nacelle data specified in [38]

Symbol	Parameter	Value (m)
D_{fan}	Fan diameter	2.71
$D_{\max}$	Maximum diameter	3.11
D_{TH}	Throat diameter	2.58
D_{HL}	Highlight diameter	2.65
a	Throat length	0.085
L_{diff}	Diffuser length	0.71
L_{nac}	Nacelle length	5.06
$L_{\max}$	Maximum diameter position	2.09
$L_{\text{b}_{\text{duct}}}$	Bypass duct length	0.69
$L_{\text{c}_{\text{duct}}}$	Core duct length	0.61

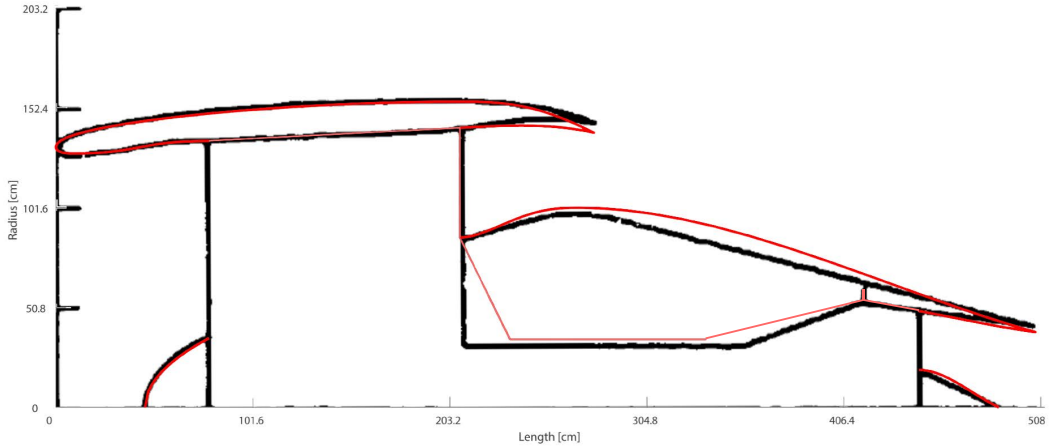

Figure 4.3 Difference in STF653 contour (black) and generated nacelle test case (red)

Note that this design vector is used twice: once to run the program for a short-ducted nacelle and once for a long-ducted nacelle. This is useful to determine the difference in the performance of the different nacelle geometry. However, two additional parameters are needed to describe the tailpipe. The choice and influence of these variables have already been discussed in Section 3.2.3. The tailpipe is kept short to minimise the skin friction without reducing the discharge coefficient.

Table 4.5 Initial design variables

	Inlet variables						
Parameters	$\frac{a}{b}$	n	MFR	CR	ϕ_i	P_i	$\frac{A_{\text{fan}}}{A_{\max}}$
Unit	–	–	–	–	°	–	–
Value	2.46	2.5	0.84	1.05	5.19	0.5	0.71

	Nozzle variables										
Parameters	Duct type	Exit type	$\frac{L_{\text{p}}}{D_{\text{ti}}}$	β_{fc}	β_{cc}	β_{p}	α_{fc}	α_{cc}	$\theta_{\text{c}_{\text{cone}}}$	Offset_{p}	$\text{Offset}_{\text{cc}}$
Unit	–	–	–	°	°	°	°	°	°	–	–
Value	1 or 2	1	1.08	26.0	15.5	24.8	12.8	7.35	10.1	0.0	0.25

	Additional long-ducted nacelle variables	
Parameters	$\frac{L_{\text{mxd}}}{D_{\text{mxd}}}$	$\frac{R_{\text{CD}}}{R_{\text{ex}_{\text{TH}}}}$
Unit	–	–
Value	0.5	1.5

4.4 Constraints

As previously mentioned, the NSGA-II program evaluates the nacelle geometry based on the objective values and constraints: the objectives are only evaluated if all the constraints are satisfied. Moreover, it makes a distinction between linear and nonlinear constraints. The program generates individuals that satisfy the linear constraints before evaluating the non-linear constraints. Constraints are necessary to account for non-aerodynamic aspects, such as structural, engine and safety requirements. The linear and nonlinear constraints that arise from these requirements are discussed in this section. Note that besides the constraints discussed here, there are additional CFD convergence requirements and clearance requirements on the fan casing and turbine mount. The latter is directly taken into account during the construction of the nacelle geometry to minimise the number of constraints needed. The CFD convergence settings are explained in Section 3.3.2.3 and can be expressed as constraints, as shown below:

$$C_{\mathrm{nl}_{\mathrm{conv}}}(1) = \epsilon_{\mathrm{residuals}} \leq 10^{-5} \tag{4.2}$$

$$C_{\mathrm{nl}_{\mathrm{conv}}}(2) = \left(\overline{C_d}_{50} - \overline{C_d}_{25}\right) {\overline{C_d}_{25}}^{-1} \leq 10^{-3} \tag{4.3}$$

$$C_{\mathrm{nl}_{\mathrm{conv}}}(3) = \sigma_{50} {\overline{C_d}_{25}}^{-1} \leq 10^{-3} \tag{4.4}$$

Firstly, the linear constraints are shown in Equations 4.5 through 4.7. These mostly arise from geometry: the cowling must have a non-negative thickness. Moreover, there must be enough room in the cowl for other structures and systems. The difference in boattail angle and the duct's wall angle is, therefore, set to 5°.

$$C_{\mathrm{l}}(1) = \beta_{\mathrm{cc}} - \alpha_{\mathrm{c_{in}}} \geq 5^\circ \tag{4.5}$$

$$C_{\mathrm{l}}(2) = \beta_{\mathrm{fc}} - \alpha_{\mathrm{f_{in}}} \geq 5^\circ \tag{4.6}$$

$$\begin{aligned} C_{\mathrm{l}}(3) &= A_{\max} \geq A_{\mathrm{HL}} \\ &= \frac{A_{\mathrm{fan}}}{A_{\max}} \cdot A_\infty - MFR \cdot A_{\mathrm{fan}} \leq 0 \end{aligned} \tag{4.7}$$

The nonlinear constraints can be broken up in two parts: those that arise from structural requirements and those that arise from engine requirements. The former is shown in Equations 4.8 through 4.11. Regulation requirements in FAR 25 an 23 describe the safety measures that must be taken to mitigate the impact of a disk failure. The nacelle cowling or a containment ring can be used to contain the debris, in which case the nacelle must be large enough to cover the debris's path. This path is shown in Figure 2.2.

$$C_{\mathrm{nl}}(1) = R_{\mathrm{fan}} \tan 15^\circ \leq L_{\mathrm{inlet}} \tag{4.8}$$

$$C_{\mathrm{nl}}(2) = R_{\mathrm{fan}} \tan 15^\circ \leq L_{\mathrm{b_{duct}}} \tag{4.9}$$

$$C_{\mathrm{nl}}(3) = R_{\mathrm{to}} \tan 15^\circ \leq L_{\mathrm{c_{duct}}} \tag{4.10}$$

The last structural constraint is a further limitation of the boattail constraints since this does not restrict the cowling thickness next to the boattail. However, the cowling must remain thick enough to ensure the structural integrity and the internal space for cooling, anti-icing and acoustic lining. Therefore, the minimum thickness is set to 0.02 m, which allows for some acoustic lining further from the boattail [59, 60]. This constraint applies everywhere on the cowling except for the last part of the boattail, as shown in Figure 4.4. Assuring that the boattail has a minimum thickness after this length, prevents very long thin tapered boattails.

$$C_{\mathrm{nl}}(4) = 0.02 - t_{\mathrm{cowl}} \leq 0 \tag{4.11}$$

The last nonlinear constraints arise from the core engine requirements to ensure a safe operation of the fan. The one-dimensional Mach number requirement at the fan is a first guideline to prevent shock forming at the tip [9]. In this case, the resulting CFD data is used so that the Mach number can be related to the inlet's performance. As such, the axial Mach number at each cell is averaged with respect to the area.

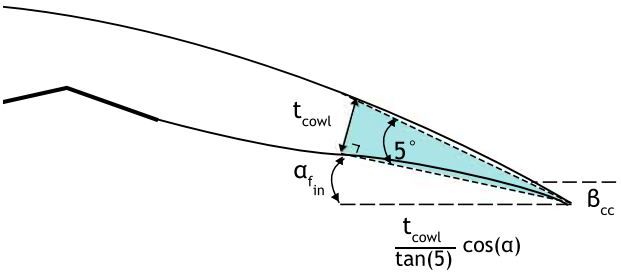

Figure 4.4 Application of the thickness constraint on the cowling

$$C_{\mathrm{nl}}(5) = D_{\mathrm{TH}} \leq D_{\mathrm{fan}} \tag{4.12}$$
$$C_{\mathrm{nl}}(6) = M_{\mathrm{fan_{CR}}} \leq 0.6 \tag{4.13}$$
$$C_{\mathrm{nl}}(7) = M_{\mathrm{fan_{TO}}} \leq 0.6 \tag{4.14}$$

4.5 Bounds

Besides the constraints, bounds are applied to the design variables to ensure that they stay within a reasonable range. Both the lower and upper bounds are shown in Table 4.6. Common values for the design variables have been discussed in Section 3.2. These values are mostly based on experiments found in literature. The upper bound for all angles is dictated by boundary layer separation. The values are set large enough to ensure that the bounds do not constrict the Pareto front.

The only bounds that can not be changed are the upper bounds for the MFR and the maximum nacelle diameter ratio. Firstly, a MFR larger than 1 in cruise would be unrealistic: that would mean that the highlight area is too small to capture the necessary air in all flight conditions. Secondly, the maximum nacelle diameter ratio depends on the minimum value for D_{max}: this can not become smaller than the clearance requirement set on the fan.

Table 4.6 Bounds of design variables

	Inlet variables						
Parameters	$\frac{a}{b}$	n	MFR	CR	ϕ_i	P_i	$\frac{A_{\mathrm{fan}}}{A_{\mathrm{max}}}$
Lower bound	1.5	1.5	0.5	1.0	4.0°	0.15	0.5
Upper bound	2.5	3.0	1.0	1.8	8.0°	0.5	$\frac{R_{\mathrm{fan}}^2 - R_{\mathrm{hub}}^2}{\left(R_{\mathrm{fan}} + y_{\mathrm{fan_{clr}}}\right)^2}$

	Nozzle variables										
Parameters	Duct type	Exit type	$\frac{L_{\mathrm{p}}}{D_{\mathrm{ti}}}$	β_{fc}	β_{cc}	β_{p}	α_{fc}	α_{cc}	$\theta_{\mathrm{c_{cone}}}$	$\mathrm{Offset_p}$	$\mathrm{Offset_{cc}}$
Lower bound	1	1	0	0°	0°	0°	0°	0°	4°	0	0
Upper bound	2	2	4.0	40°	40°	45°	30°	30°	30°	0.7	0.4

	Additional long-ducted nacelle variables	
Parameters	$\frac{L_{\mathrm{mxd}}}{D_{\mathrm{mxd}}}$	$\frac{R_{\mathrm{CD}}}{R_{\mathrm{ex_{TH}}}}$
Lower bound	0.1	0.05
Upper bound	1.2	3.0

4.6 Model Structure

As stated in Section 3.4.2, the NSGA model structure is used for the multiobjective algorithm. The global steps to create and evaluate each generation are discussed in that section and are shown in Figure 3.17. However, this did not include the separate actions and external file reports to evaluate each individual. Instead, these actions are shown in Figure 4.5. This loop is repeated for each individual in the population. Once every individual is evaluated, the NSGA-II algorithm continues with the generation of the next population, as shown in Figure 3.17. Note that two measures are taken to decrease the computational time needed per individual:

- Figure 4.5 includes three decision points. The last two decision points are automatically included by the NSGA algorithm as it only evaluates the objectives once all the constraints are satisfied. However, an additional decision point is included midway of the constraint evaluation. If the first five nonlinear constraints are not satisfied, the program will skip the CFD analysis. It reduces the computational time considerably during the first few generations and prevents that Fluent would crash due to unrealistic geometries.
- The cruise and take-off analysis in Fluent is run in parallel. This saves about 3-4 minutes for each individual.

The NSGA-II algorithm tries to minimise both objectives, while the designer wants to maximise the net propulsive force. The objective is therefore formulated as a percentage of the initial nacelle, as shown in Equation 4.15. An objective value of 0.9, therefore, means an increase of 10% in the NPF with respect to the initial nacelle. A mathematical description of the complete optimisation is shown below.

$$\text{Minimize: } \begin{cases} 1 - \frac{NPF_{\text{CR}} - NPF_{\text{CR}_{\text{init}}}}{NPF_{\text{CR}_{\text{init}}}} \\ 1 - \frac{NPF_{\text{TO}} - NPF_{\text{TO}_{\text{init}}}}{NPF_{\text{TO}_{\text{init}}}} \end{cases} \tag{4.15}$$

Subject to:

Convergence constraints

$C_{\text{nl}_{\text{conv}}}(1) = \epsilon_{\text{residuals}} \leq 10^{-5}$

$C_{\text{nl}_{\text{conv}}}(2) = \left(\overline{C_{d_{50}}} - \overline{C_{d25}}\right) \overline{C_{d25}}^{-1} \leq 10^{-3}$

$C_{\text{nl}_{\text{conv}}}(3) = \sigma_{50} \overline{C_{d25}}^{-1} \leq 10^{-3}$

Linear inequality constraints

$C_{\text{l}}(1) = \beta_{\text{cc}} - \alpha_{\text{c}_{\text{in}}} \geq 5^\circ$

$C_{\text{l}}(2) = \beta_{\text{fc}} - \alpha_{\text{f}_{\text{in}}} \geq 5^\circ$

$C_{\text{l}}(3) = D_{\max} \geq D_{\text{HL}}$

Nonlinear inequality constraints

$C_{\text{nl}}(1) = R_{\text{fan}} \tan 15 \leq L_{\text{inlet}}$

$C_{\text{nl}}(2) = R_{\text{fan}} \tan 15 \leq L_{\text{b}_{\text{duct}}}$

$C_{\text{nl}}(3) = R_{\text{to}} \tan 15 \leq L_{\text{c}_{\text{duct}}}$

$C_{\text{nl}}(4) = 0.02 - t_{\text{cowl}} \leq 0$

$C_{\text{nl}}(5) = D_{\text{TH}} \leq D_{\text{fan}}$

$C_{\text{nl}}(6) = M_{\text{fan}_{\text{CR}}} \leq 0.6$

$C_{\text{nl}}(7) = M_{\text{fan}_{\text{TO}}} \leq 0.6$

Design vector:

$$x = \left[\frac{a}{b}, n, MFR, CR, \phi_i, P_i, \frac{A_{\text{fan}}}{A_{\max}}, \text{Duct type, Exit type, } \frac{L_{\text{p}}}{D_{\text{ti}}}, \right.$$
$$\left. \beta_{\text{fc}}, \beta_{\text{cc}}, \beta_{\text{p}}, \alpha_{\text{fc}}, \alpha_{\text{cc}}, \theta_{\text{c}_{\text{cone}}}, \text{Offset}_{\text{p}}, \text{Offset}_{\text{cc}}, \frac{L_{\text{mxd}}}{D_{\text{mxd}}}, \frac{R_{\text{CD}}}{R_{\text{ex}_{\text{TH}}}} \right]$$

Bounds:

$$\text{Upper bound} = \left[2.5, 3.0, 1.0, 1.8, 8.0, 0.5, \frac{R_{\text{fan}}^2 - R_{\text{hub}}^2}{\left(R_{\text{fan}} + y_{\text{fan}_{\text{clr}}}\right)^2}, 2, 2, 4.0, \right.$$
$$\left. 40, 40, 45, 30, 30, 30, 0.7, 0.4, 1.2, 3.0\right]$$
$$\text{Lower bound} = [1.5, 1.5, 0.5, 1.0, 4.0, 0.15, 0.5, 1, 1, 0,$$
$$0, 0, 0, 0, 0, 4, 0, 0, 0.1, 0.05]$$

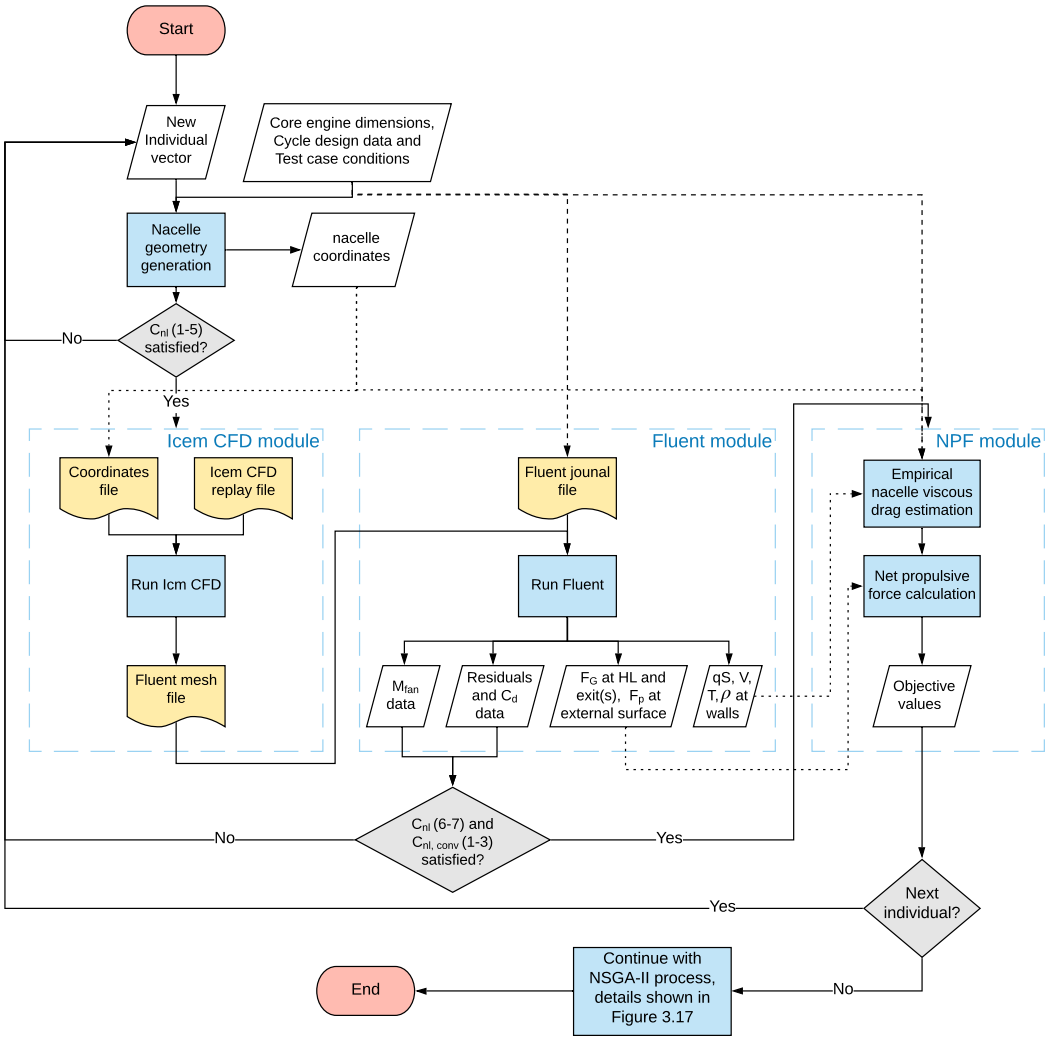

Figure 4.5 Model structure per individual

5 VERIFICATION AND VALIDATION

The larger and more complex a code becomes, the more susceptible it is to errors. The program needs to be tested to ensure that it works according to expectations. This can be achieved by verifying and validating the program. Verification answers the question: *Does the product meet the requirements?*. Several requirements for the code are to be as fast, accurate and robust as possible. Ideally, a designer must be able to treat the code as a 'black box'. That is, a designer without a profound knowledge of the code should still be able to run the code by adapting the initial variables and boundaries only. The most basic verification methods are simply inspecting the code for bugs and running smaller unit tests on the (sub)systems. A slightly more complex verification of a subsystem is the mesh convergence study, which explained in more detail in Section 5.1. A verification method to test the complete program is a sensitivity analysis. This is done for several variables in Section 5.3.

Validation is performed after verification, and answers the question: *Does the software resemble reality?*. This question is harder to answer, as it requires actual data which is not always publicly available. A part of the discrepancies between the test case and the program's geometry has been discussed in Chapter 4. Section 5.4 tries to validate the program further by comparing the engine cycle data with other reference engine data available.

5.1 Mesh Convergence Study

CFD simulations are sensitive to the mesh. In terms of computational time, a very coarse mesh is desired but the mesh should remain fine enough to capture the aerodynamic flow correctly. A mesh convergence study is performed to determine the impact of the mesh. The coarsest mesh is refined by gradually increasing the number of elements. This is done for both the short-ducted and the long-ducted nacelle. The nacelle geometry for these test cases is described in more detail in Chapter 4.

Several meshes where created varying from 70 000 elements to 500 000 elements. Refinement is mostly limited to the blocks around the nacelle, with gradual increasing element sizes outwards to have a smooth grid transition between blocks. A slightly denser mesh is necessary at the boattail to accurately capture the shocks formation in this region. Figures 5.1 and 5.2 show the convergence plot of a short-ducted and long-ducted nacelle respectively. In both figures, the error in the net propulsive force and the drag coefficient is plotted against the required convergence time and mesh elements. The error is calculated with respect to the propulsive force data represented in [38], as shown in Equation 5.1. Thus, the corrected mass flow is set to 1184 $\frac{kg}{s}$ for a fair comparison of the drag forces, irrespective of the high fan Mach number discussed in Section 4.2.2. However, the drag data in [38] could not be used for the drag coefficient, as this uses a different force breakdown. Instead, the inviscid drag coefficient error is calculated relative to the finest tested grid. Table 5.3 shows more details about the drag forces.

$$Error_{NPF} = \frac{NPF_{\text{data}} - NPF_{\text{mesh}}}{NPF_{\text{data}}} \cdot 100\% \quad (5.1) \qquad Error_{\text{C}_\text{d}} = \frac{C_{d_{\text{inv}}} - C_{d_{\text{inv}}}^{\text{fine}}}{C_{d_{\text{inv}}}^{\text{fine}}} \cdot 100\% \quad (5.2)$$

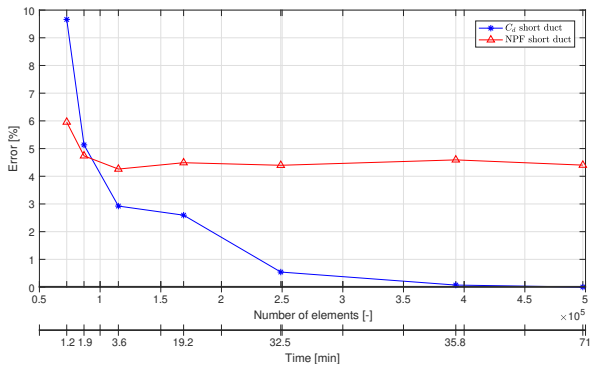

Figure 5.1 Mesh converge of the short-ducted nacelle at M=0.8, h=10670 m, $\dot{m}_{\text{corr}}$=1184 kg/s

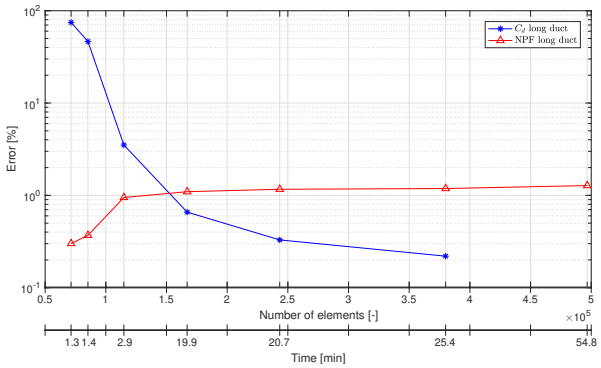

Figure 5.2 Mesh converge of the long-ducted nacelle at M=0.8, h=10670 m, $\dot{m}_{\text{corr}}$=1184 kg/s

A rapid decrease is visible in the drag coefficient error for both the long-ducted and short-ducted nacelle. The error reduces to 2.9% and 3.5% for the third mesh, which has about 115 000 mesh elements. The error for the NPF does not converge to zero but levels out to 4.4% for the short-ducted nacelle. This error is partly due to the empirically calculated friction drag. If only the thrust and pressure drag on the outer surface are compared, the error reduces to less than 1% for meshes larger than 105 elements. Similarly, the error in the NPF for a long-ducted nacelle levels out at 1.8%. However, this error shows an increasing trend. A longer duct causes a weaker shock at the boattail than a short duct, thereby reducing the pressure drag and increasing the net propulsive force slightly. As the mesh becomes finer, the shock is better captured and the difference in thrust becomes increasingly apparent.

The third mesh was selected for both the long-ducted and short-ducted nacelle. This mesh has a drag coefficient error around 3% and a finer mesh does not show much improvement in the NPF. The time calculation for this mesh is limited to 3-4 minutes.

5.2 Mesh Quality Assessment

The mesh quality can also influence the results. However, the quality of the mesh can only be estimated. As the geometry changes during the optimisation , so does the quality of the mesh change. However, assuming that the initial geometry is a logical starting point, it is not expected that large changes in the nacelle geometry and the meshing blocks will occur. The meshes previously shown in Figures 3.14 and 3.15 will be taken as a guideline for the quality assessment. If these have a high quality, it is assumed that the geometry adjustments during the optimisation do not have enough impact to deteriorate the quality and convergence rate much.

Besides the mesh size, a quality assessment usually includes checking the aspect ratio, skewness and smoothness of the cells [61]. An optimal structured grid would have equilateral squares whose sizes change smoothly through the domain. Firstly, the aspect ratio is a measure of the stretching of the cell. It can be calculated as the longest edge side over the shortest edge side, although Fluent uses a slightly different definition. This defines the aspect ratio as the maximum distance from the cell's centroid to the cell's node divided by the minimum distance from the centroid to the edge [62]. This value should be kept as low as possible, generally below 5 outside the boundary layer. There is no definite upper limit, but higher values can influence the stability of the energy equation [62]. Figure 5.3 shows the distribution of the cell's aspect ratio. The majority of the elements, about 58%, has an aspect ratio below 8. Some higher aspect ratio elements are present in the block behind the engine's exhaust due to the grid refinement around the engine. However, these elements align with the flow direction. The energy equation remained therefore stable in all of the geometries analysed.

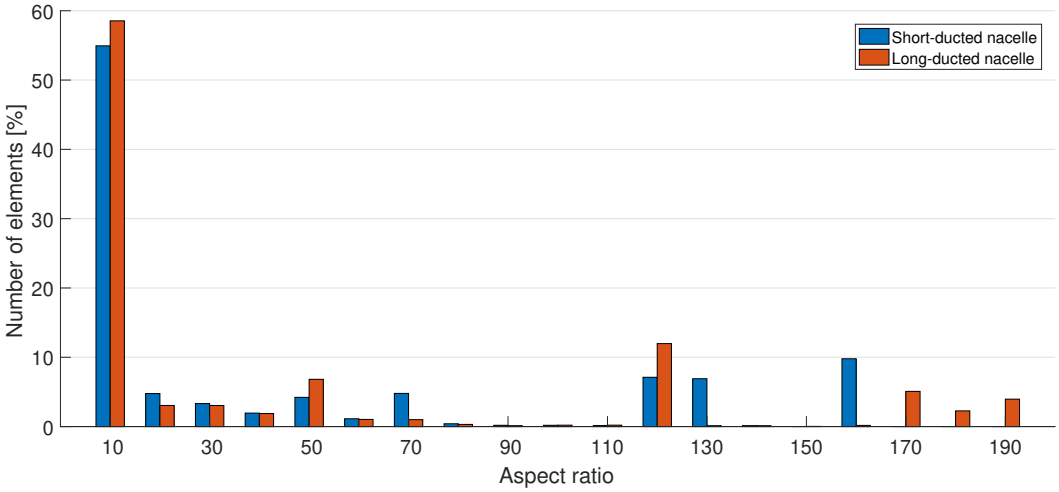

Figure 5.3 Aspect ratio distribution of the mesh

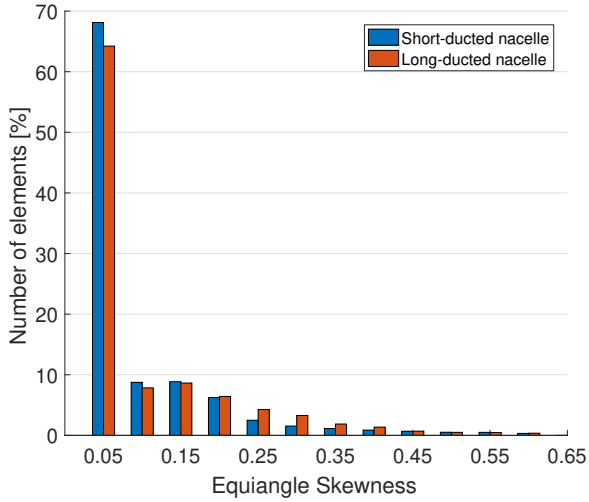

Figure 5.4 Equiangle skewness distribution of the mesh

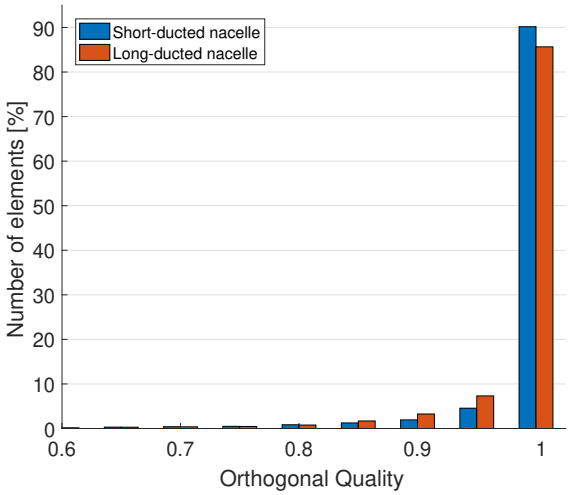

Figure 5.5 Orthogonal quality distribution of the mesh

The second parameter is the equiangle skewness. This parameter influences the accuracy and stability of the solution. Its value should stay close to zero so that the cell's angles are 90°. Figure 5.4 shows the skewness distribution for a long- and short-ducted nacelle. The largest part of the mesh is not skewed, except for the elements around the hub and inlet lip. This is unavoidable as the mesh should follow the geometry. When comparing the actual cell angles, it can be said that most angles should remain within 45° and 135° and never fall below 30° [61]. The mesh fulfils these conditions, as all the angles remain within 36° and 144°. Only 0.8% of the mesh elements falls outside the 45°-135° bound.

The last parameter is the smoothness of the mesh. ICEM CFD allows for the matching of edges. This means that the user can specify the number of elements in a horizontal or vertical direction of a mesh block. With edge matching, the cells of two consecutive blocks are spread such that there is a smooth transition between these blocks. The mesh will then be smooth as long as there are enough elements specified in a block. This option is applied to the meshes during the optimisation to smooth the mesh irrespective of the changing geometry. Especially the horizontal spacing behind the nacelle is difficult to match with that of the two exhaust streams. However, the mesh

size is deemed large enough that the ratios between cells remain small and give accurate results. Fluent also looks at the orthogonality of the mesh [62]. For a 2D mesh, this is calculated as the cosine between the edge normal vector and the vector from the centroid to the edge. The orthogonality should be as close to one as possible and always stay above 0.05 [62]. Figure 5.5 shows that this bound is satisfied with a large margin. It can thus be concluded from these three parameters that the quality of these meshes are satisfactory.

5.3 Parameter Sensitivity

When starting the program with an initial nacelle design, the algorithm will search for an optimum. The code will go through different design variable values and combinations in its search. However, several other parameters that influence this search are kept constant. A sensitivity analysis tries to determine how much this affects the eventual results. One or multiple fixed parameters are varied to analyse the differences in the results. Some examples are the algorithm settings and the assumed test conditions.A sensitivity analysis is conducted for these parameters in Subsections 5.3.1 and 5.3.2.

5.3.1 Influence of Population Size Settings

A large population size allows for a broader search of the design space. It increases the chance of finding a global optimum. The downside is that the complexity increases. To determine the rank of an individual, the algorithm needs to determine: 1) the number of individuals that another individual dominates and 2) the amount of individuals that dominate the individual. If this is repeated for each objective, then the algorithm goes through $2N^2$ comparisons [55, 56]. This makes large population sizes computational expensive. A population size of at least twice the amount of design variables is selected to allow for enough variation. The program is run for a population size of 50 and 100. The computational time is sensitive to the number of generations. [63] has shown that large population sizes do not improve the GA results when the number of evaluations, or time, is restricted. Time restricts the number of generations and therefore the convergence rate. To ensure that the program is completed after two days, the number of generations, G, is set to 13 and 6 respectively. Moreover, this ensures that every run evaluates 700 geometries.

Figures 5.6 and 5.7 show the best individuals stored in the archive for each generation. It clearly shows that the larger population has had too little generations to converge. It took until the sixth generation to find a 100 geometries that meet all constraints and thus had their objective values evaluated. After this happens, the archive gets updated and the worst individuals are replaced by better geometries to get closer to the Pareto front. However, the inferior solutions are still present at the last generation due to the restricted number of generations. No

Figure 5.6 Optimisation in the objective space for N=50

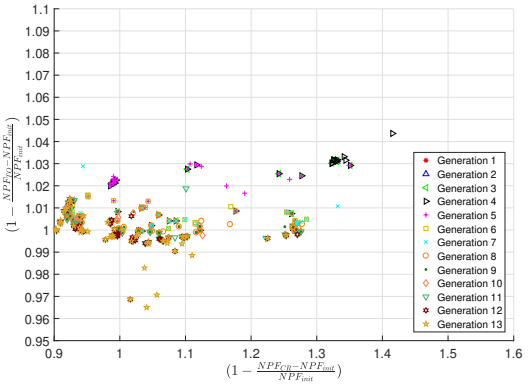

Figure 5.7 Optimisation in the objective space for N=100

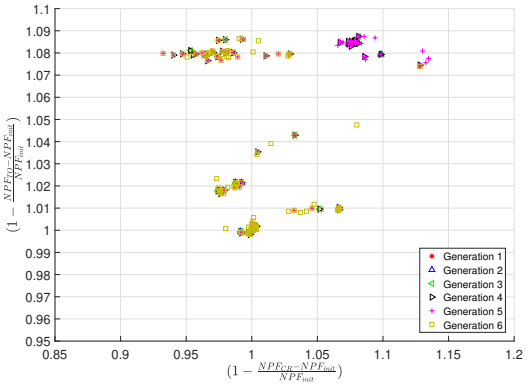

distinctive Pareto front has been found. Thus, a larger population size might effectively broaden the search but is time-consuming to be considered for this problem. Rather, the same might be reached by varying the other algorithm settings explained in Section 5.3.2. The relative time of each generation is also shown in Table 5.1. The population size will be kept to 50 for the other analyses in this report as this allows for more generations within the time frame while keeping sufficient diversity in the individuals.

Table 5.1 Run time per generation

Generation		1	2	3	4	5	6	7	8	9	10	11	12	13
Elapsed	N=50	8.35	12.2	16.4	20.5	24.4	27.7	30.5	33.6	36.5	39.8	42.9	46.4	49.8
time [hr]	N=100	11.6	15.6	23.1	32.0	40.9	49.8							
Generation	N=50	501	228	252	248	233	198	173	182	174	201	186	206	202
time [min]	N=100	697	240	450	535	532	531							

Note that the time for the first generation includes both the initial randomly generated population as well as the first population. Thus, 100 individuals are evaluated in 501 minutes. This is due to the internal structure of Matlab's *gamultiobj*. Moreover, The first few generations take slightly more time than later generations. This is most likely due to the CFD analysis. At the first few generations, some geometries do not converge so that Fluent runs until it reaches the maximum amount of iterations. Fluent converges faster as the geometries improve in later generations. The average time needed to evaluate one individual is about 4.3 minutes.

5.3.2 Influence of Crossover and Mutation Settings

The individuals of the next generation are created by applying crossover and mutation to the best individuals of the previous generations. The amount of individuals generated by crossover is set with the probability of crossover P_c. Thus, if a population size of 50 is used, and P_c is set to 0.8, then 40 individuals will be created by crossover. The remaining individuals are created by mutation probability P_m or by the survival of parents to the next generation. The latter is redundant as a separate archive is used for elitism. In this case, it holds that:

$$P_c + P_m = 1 \tag{5.3}$$

These control parameters are closely related to the population size. Crossover is often more effective than mutation, as it ensures a fast exploration, while mutation causes a more random search. However, the mutation probability increases when the population size is smaller to ensure that the design space is effectively covered [55, 63]. [64] investigated seven parameter settings of GA and concluded that crossover influences the success of GA the most, followed by mutation and population size. Moreover, [63] has shown that a population size N in between 20-30 gives the best GA convergence for P_c = 0.75-0.95 and P_m = 0.005-0.01. The same crossover rate, of 0.8, is also recommended for Matlab's *gamultiobj* function [65]. This gives a mutation probability P_m of 0.2.

The other parameters introduced by [56] into the crossover and mutation function are η_{cr} and η_m. As mentioned previously, these variables influence the amount of manipulation to a parent to create the child. The higher the value, the closer the child will be to the parents. These operators influence the spread of the solution. [56] uses a value of 20 for both η_{cr} and η_m for most test cases, only lowering it if the solution is prone to converge to a local optimum. The program is run once for a value of 20 and once for a value of 5 to analyse the influence of these operators. The population size and number of generations is the same as in Section 5.3.1.

Figures 5.8 and 5.9 show the advancing Pareto front over the generations. Figure 5.9 is identical to Figure 5.6 but depicted again for fast comparison between the two solutions. Note that the first generations of a run sometimes include the same points. It is not until the fifth generation that 50 geometries have been found that meet all constraints. After this, the solution quickly converges from its broad search: the best points are used to create the next population and thus more and more realistic geometries are found near the Pareto front. The plots also

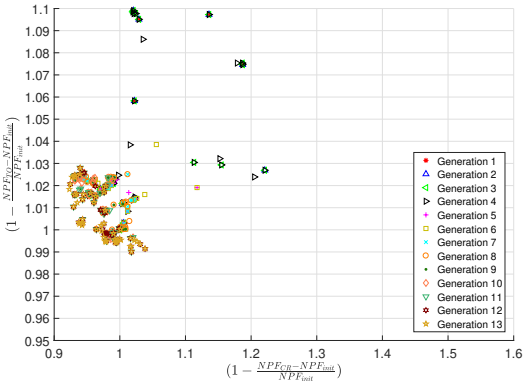

Figure 5.8 Optimisation search in the objective space for η_{cr}, η_m =5

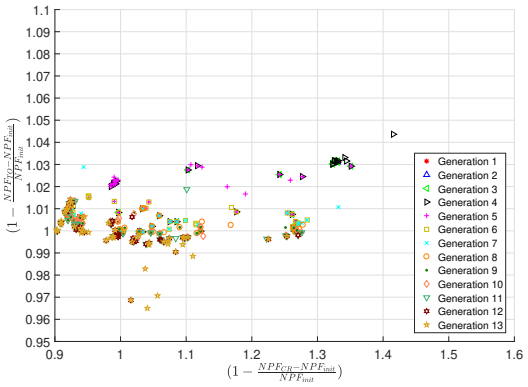

Figure 5.9 Optimisation search in the objective space for η_{cr}, η_m = 20 (Same as Figure 5.6)

show the difference in convergence speed. For η_{cr}, η_m = 5, there is a large exploration of the design space at the beginning due to the higher mutation rate. However, a lot of these geometries are far from realistic and produce worse results than the initial starting point, which lowers the convergence speed. The last generation has 14 non-dominated individuals, but their value is comparable to the 11th generation of the other solution with η_{cr}, η_m = 20. The other solution, η_{cr}, η_m = 20, has advanced further in the last two generations but has only 7 non-dominated solutions as a result.

For a fair comparison between both solutions, the convergence and the diversity of the individuals should be checked. [56] uses these criteria to determine the effectiveness of their algorithm for several multi-objective problems. However, the former cannot be checked without a known optimal Pareto front to compare the current front against. Both fronts are still advancing, but a higher value for the crossover and mutation operators speeds up the convergence. A lower mutation operator or higher mutation probability might be more effective in later generations to ensure that the complete length of the Pareto front is found and the solution does not converge to a local Pareto front. For the number of generations selected a higher crossover and mutation value converges faster.

The other criteria measures how much the individuals are spread equally between the outermost boundary individuals. Figure 5.11 is a figurative representation of the parameters needed for this criteria. Figure 5.10 shows the obtained solutions in the last generation, where the non-dominated individuals for each case are encircled. The boundary individuals are usually found by fitting a curve through the obtained Pareto front that is parallel to the optimal Pareto front [56], to ensure that the complete Pareto region is covered. Lacking data on the optimal Pareto front, the outermost individuals of both solutions are used instead. These are encircled with a thicker green ring in Figure 5.10. The diversity matrix is then obtained with:

$$\Delta = \frac{d_f + d_l + \sum_{i=1}^{N-1} |d_i - \bar{d}|}{d_f + d_l + (N-1)\bar{d}} \qquad \text{[56]} \qquad (5.4)$$

Where d_i is the Euclidean distance between the obtained individuals and $\bar{d}$ is the average of these distances. Note that by setting the boundary individuals equal to one of the attained individuals, both d_f and d_l are zero for one of the found Pareto fronts. The best distribution would be an equal distance between all the individuals, in which case Δ goes to zero. Table 5.2 shows the calculated data of the non-dominated solutions in the last generation. It can be seen that a higher value for the crossover and mutation operators improves the results for the mean objective. The diversity matrix is high for both solutions because several points lie close to one another, with a Euclidean distance less than $5 \cdot 10^{-3}$. In Figure 5.10, these points lie nearly on top of each other. The solution $\eta_{cr}, \eta_m = 5$ performs

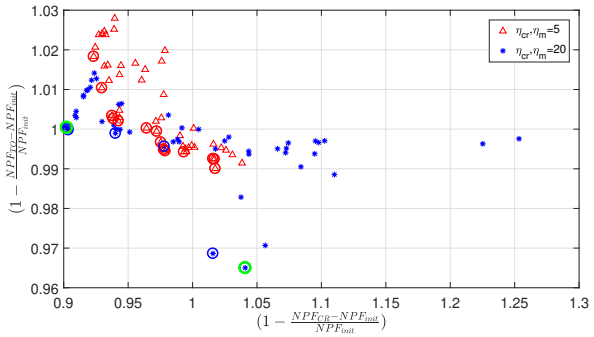

Figure 5.10 Obtained Pareto front for both η_{cr}, η_m = 5 and 20

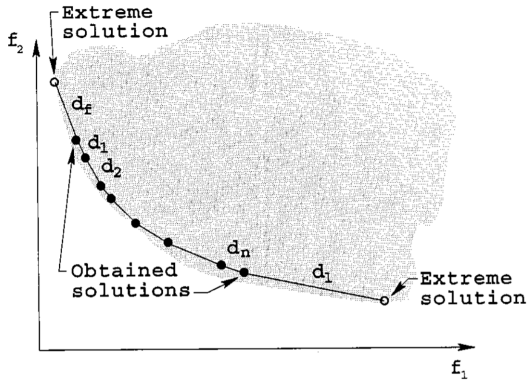

Figure 5.11 Parameters for the diversity matrix Δ

worse because it has more points with such a small distance. Moreover, the length of the Pareto front is smaller which gives higher values for d_f and d_l. Thus, this solution $\eta_{cr}, \eta_m = 20$ has a better spread and converged Pareto front. The operators use a value of 20 for all further analysis discussed in this report.

Table 5.2 Spread and average objective value of the individuals on the Pareto front for η_{cr}, η_m = 5 and 20

Parameter	Symbol	η_{cr}, η_m=5	η_{cr}, η_m=20
Mean cruise objective	$\bar{f}_1$	0.97	0.96
Standard deviation cruise	σ_{CR}	0.032	0.053
Mean take-off objective	$\bar{f}_2$	1.00	0.99
Standard deviation take-off	σ_{TO}	0.007	0.015
Diversity matrix	Δ	0.85	0.65

5.4 Validation of Engine Model

Validation of the engine model is a difficult task, as engine manufacturers only post the most basic engine cycle data. Information about the nacelle geometry is even more scarce. This was one of the main reasons to chose the engine from [38] to test the program. The report is from a scientific engine development program, and therefore included both the basic engine cycle data as well as the nacelle geometry. These variables are discussed in Chapter 4. However, the parameters that can be used for validation are limited to the drag and thrust forces. These are shown in Table 5.3.

This table clearly shows that there are large differences in the values of the respective drag and thrust terms, even though the final NPF lie relatively close. [38] calculates these forces with correlations between geometry and experimental data. The cowl friction, for example, is calculated for a flat plate friction drag and multiplied by 0.98 to fit the experimental scale model test data. Similar approaches are taken for the wave drag, pressure drag, duct offset losses and thrust coefficient. Thus, all of these forces are related to experimental data. The second row includes the forces obtained from the inviscid Euler analysis in Fluent with the method described in Sections 3.1.3 and 3.3. The force difference between the two columns is due to the inviscid analysis. This causes a higher pressure and velocity at the nacelle skin and the duct exhausts, resulting in higher values for both the thrust and drag values.

However, the largest difference is in the determination of the inlet drag. The inlet performance from [38] only includes pressure losses and no friction forces. It is impossible to determine pressure losses with an inviscid analysis, so the inlet drag calculated from Fluent is the friction drag. The rather blunt shape of the hub causes the largest friction drag. The last row in Table 5.3 shows that the error in NPF is reduced to 1.46% if the hub friction drag is not taken into account. Thus, the analysis of the NPF is relatively close to the actual model even if the individual force terms differ. However, it was decided to keep hub friction drag for the optimisation. The hub geometry is kept constant, but the inlet geometry changes. This might improve the friction drag of both the inlet and the hub. Keeping the hub friction drag will show a larger difference in optimisation objectives and improve the overall inlet geometry optimisation.

Table 5.3 Validation of the model forces with $\dot{m}_{corr}$=1184$\frac{kg}{s}$ in cruise condition ($h = 10670\ m$, $M = 0.8$)

	Forces from [38] [N]	Forces from Fluent [N]	Error [%]
T_{int}	52266	59101	13.08
$C_{t_{bypass}}$	0.9953	0.9983	0.35
$C_{t_{core}}$	0.9957	0.9944	0.13
D_{inlet}	94.08	390.57	315.1
D_{hub}	-	1409.50	-
$D_{fric_{AB}}$	577.60	1580.60	173.6
$D_{fric_{cowl}}$	729.00	1424.10	95.4
$D_{pressure}$	223.20	5673.00	2441.7
NPF[1]	50407	48260	4.26
NPF[2]	50407	49669.5	1.46

[1] Approximating internal drag from [38] as $D_{internal} = (1 - \frac{C_{t_{bypass}} + C_{t_{core}}}{2})T_{int}$

[2] Neglecting the hub friction drag D_{hub}

Another way of determining if the initial engine parameters are reasonable is by comparing it to other existing engines. Table 5.4 shows the basic engine data available of other engines currently in service. The JT9D engine is an older model but used as a reference engine in [38]. The STF 653 engine was a conceptual engine developed by [38] in the 1980s to improve the engine technology and its efficiency. To see whether the engine performs according to today's technology, the engine cycle data from Table 5.4 is plotted.

Figures 5.12 and 5.13 show the change in mass flow and bypass ratio with the take-off thrust. The mass flow of the STF 653 engine in line with the other data. However, a different trend is seen in Figure 5.13 for the low and high

Figure 5.12 Reference engines plotted for take-off thrust against mass flow

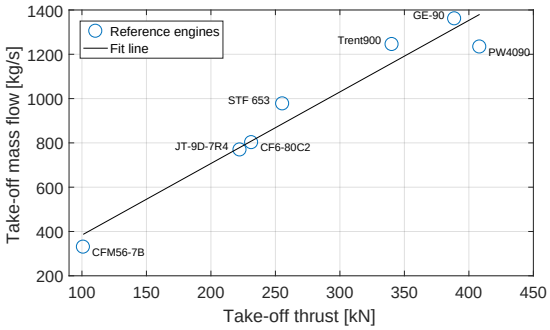

Figure 5.13 Reference engines plotted for take-off thrust against bypass ratio

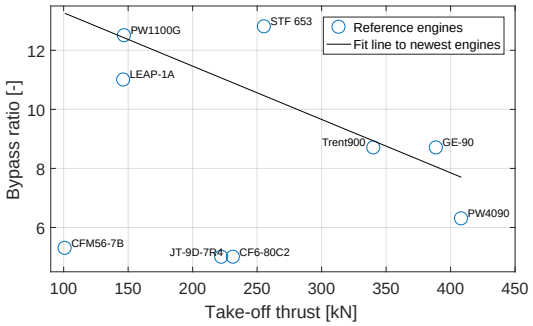

Table 5.4 Comparison of STF653 engine against existing engines [38, 66–69]

Parameter	T_{CR}	T_{TO}	$\dot{m}_{TO}$	PR_{HPC}	FPR	BPR	$\frac{L_{\text{nac}}}{D_{\text{max}}}$	D_{fan}	D_{max}
Unit	kN	kN	$\frac{kg}{s}$	-	-	-	-	mm	mm
STF 653	50.3[1]	255.5	970	23.0	1.53	12.8	1.625	2713	3111
JT-9D-7R4	52.0	222.4	769	24.2	1.67	5	1.368	2372	2463
GE-90	77.4	388.8	1361	34.4	1.65	8.7	1.44	3124	3404
CFM56-7B	24.2	101	330.2	32.7	-	5.3	1.37	1549	1829
CF6-80C2	50.4	231.4	802	27.4	-	5	1.585	2362	2692
PW1100G	-	147	-	-	-	12.5	1.529	2032	2224
PW4090	-	408.3	1233.8	38.6	1.74	6.3	1.622	3001	2845
RR Trent 900	65.4	340.3	1245	41.1	-	8.7	1.389	2946	3944
LEAP-1A	-	146.4	-	40	-	11	1.314	1981	2533

[1] Cruise thrust adapted from data in [38] to a lower $\dot{m}_{corr}$ of 1083 $\frac{kg}{s}$, see Section 4.2.2.

bypass ratio engines. The bypass ratio is closely related to the mass flow. For a given core mass flow, there is an optimum bypass ratio for the engine. Increasing the bypass ratio increases the mass flow, fan diameter and thrust of the fan duct. If the fan diameter grows too large, the size and weight will offset the increase in thrust. The opposite also holds. If the total mass flow is constant, then the take-off thrust will decrease with a higher bypass ratio, as a greater portion of the exhaust gas is cold. This is one of the reasons for the difference in take-off thrust between the RR Trent 900 and PW4090 engines. For two other engines, the PW1100G and LEAP-1A, are the mass flows unknown. Their mass flow must lie in between the CF6-80C2 and CFM56-7B engines when comparing the fan diameter of all the engines. Combined with their high bypass ratios, would explain their lower take-off thrust. The test engine, the STF 653, has the largest bypass ratio. This is high when compared to the current engines, even though the mass flow and take-off thrust are in line with the other data. This will influence the nacelle design, as the bypass will choke in cruise conditions while the core remains unchoked.

Figures 5.14 and 5.15 show the trends of the different nacelle dimensions. Firstly, the STF 653 is in line with the other engines' maximum diameter and fan diameter. Secondly, the slenderness of the engine is plotted in the last figure. The maximum diameter follows from the engine size and requirements, such that the main varying parameter is the length. Stubby nacelles, with a low slenderness ratio, tend to have a higher wave drag as the nacelle's curvature increases [70]. However, longer nacelles have a higher wetted area. This division is visible in Figure 5.15. The STF 653 is designed for a low wave drag, and is thus in line with the other slender nacelles [38].

Figure 5.14 Reference engines plotted for maximum diameter against fan diameter

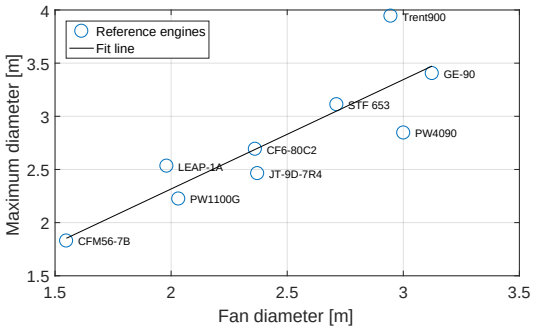

Figure 5.15 Reference engines plotted for slenderness ratio against fan diameter

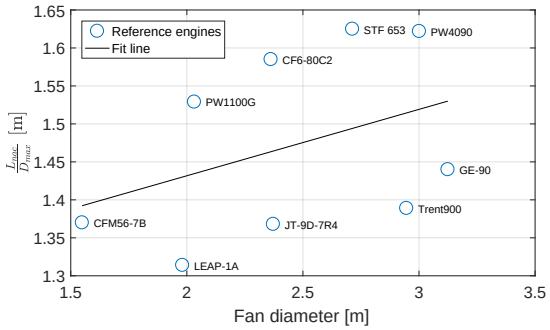

6 RESULTS OF THE NACELLE DESIGN METHOD

This chapter presents the main results from the multiobjective optimisation carried out in this report. The convergence will be analysed to find out which conditions are influencing the results. Afterwards, the geometries and their impact on the aerodynamic forces are analysed. This is repeated for several geometries and flow conditions.

6.1 Optimisation objective and constraints

Chapter 4 discussed all the variable and constraint settings of the program. It was then run for four different cases: all with the same cruise condition, but either for a short-ducted nacelle with different take-off conditions or for a long-ducted nacelle with the same take-off condition. This was done to analyse how both the parameters and selected flow conditions influence the geometry. Figure 6.1 shows the non-dominated individuals on the Pareto front for all four cases. The front is expressed directly in the NPF rather than their objective values from Equation 4.15 since the take-off values differ for cases 1, 3 and 4. The starting points, from the initial geometry, are boxed in red. Not every individual in the last generation lies on the Pareto front. Only 7, 16, 5 and 5 non-dominated individuals are found for each case respectively. Thus, the program is still focused on advancing the front rather than improving the spread. It is recommended for future analysis to either run the program for a longer time or, when more data is available, to improve the initial generation by specifying more geometries. This prevents a lot of randomly generated individuals in the first population which improves the convergence rate.

Figure 6.1 Pareto front in terms of NPF for all four aerodynamic test conditions

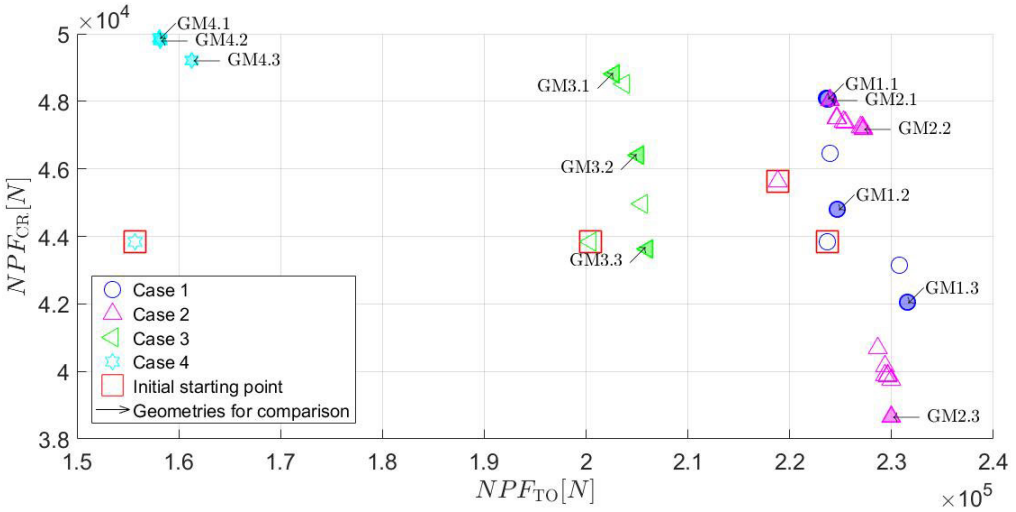

The upcoming sections will discuss the constructed geometries and compare them to other test cases to determine how this has influenced the geometry. For simplicity, only three geometries for each case are used for the comparison. Two geometries are selected at the Pareto fronts ends: the geometries with either the best cruise performance or the best take-off performance. These two individuals are expected to give the largest difference in geometry. The last geometry is a compromise between the two conditions as it lies in the middle of the Pareto front. Figure 6.1 includes the numbering of all the geometries. The other sections will use the same numbers to refer to the different geometries. A list of the thrust and drag forces for these geometries is included in Appendix D. Before the final geometries are explained, the following subsection will discuss the convergence and the influence of the constraints on the results.

6.1.1 Influence of Bounds and Constraints on Convergence

The constraints are evaluated in steps, as explained in Section 4.4. After all, it is unreasonable and time-consuming to perform a CFD analysis on a geometry that doesn't satisfy the geometry and structural constraints. Only when all the constraints are satisfied are the objectives evaluated. Depending on how restrictive the constraints are, it can take several generations before the archive is filled with only feasible individuals. The number of feasible individuals found per generation is shown in Figure 6.2 for all four cases. In the first few generations, the number of feasible individuals almost doubles every generation. Crossover and mutation create better individuals when the parent individuals stored in the archive improve. The archive is filled after the fourth or fifth generation. After this, the number of feasible individuals found per generation stays relatively constant.

The archive gets updated after N feasible individuals are found. The best individuals found in each generation will replace the worst ranking individuals in the archive. Figure 6.3 shows the number of new individuals in the archive per generation. When comparing Figure 6.2 with Figure 6.3, it shows that still about half of the feasible solutions are used to improve the archive in the last generations. This also confirms that the Pareto front can be further improved if the program runs for a longer time, as at least 17-25 new individuals are still added to every generation. Case 2 has the least number of individuals added to the archive. This is also the case with the most non-dominated solutions at the front in Figure 6.1. It is found that the Pareto front did not advance much further in the last generations. However, several individuals are still added to the archive every generation to improve the spread over the Pareto front.

Figure 6.2 Number of feasible individuals found per generation

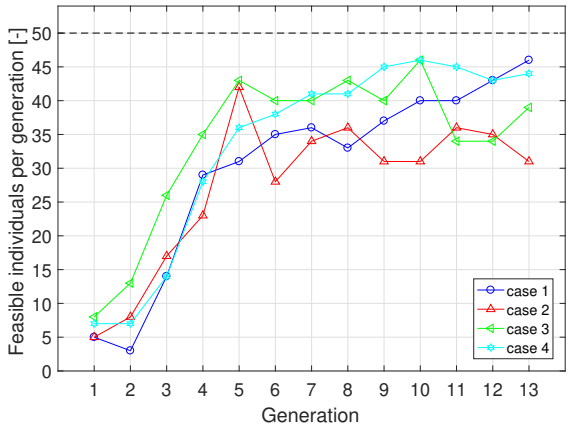

Figure 6.3 Number of new individuals added to the archive per generation

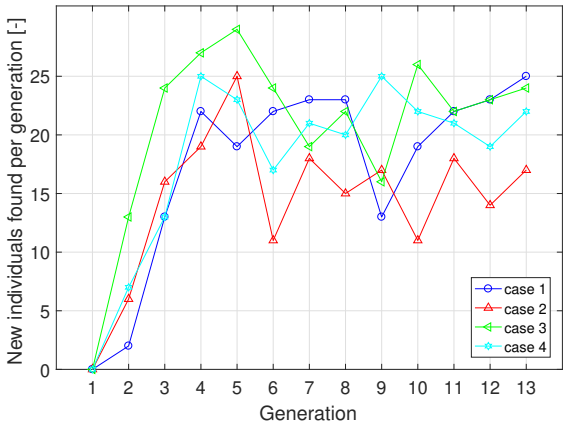

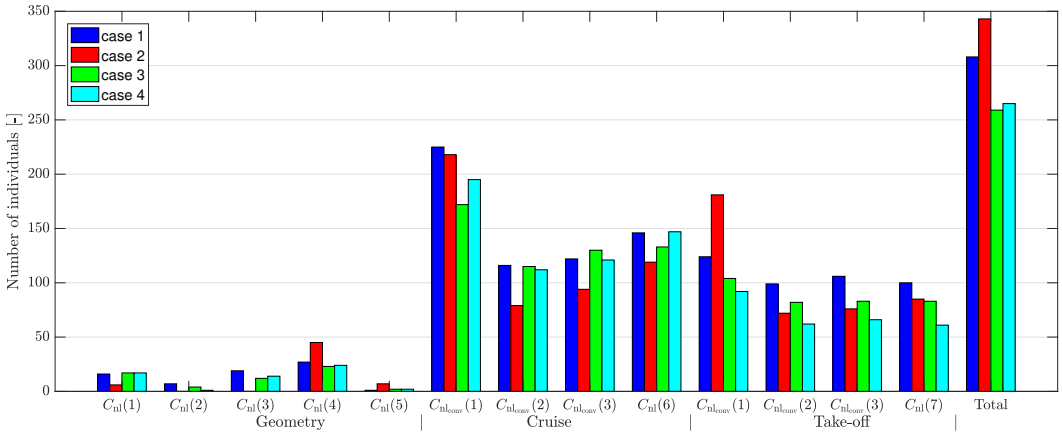

Figure 6.4 Total number of violated constraints

The total number of geometries evaluated for every run is $N(G+1)$, where N is the population size and G the number of generations. Every case evaluated 700 geometries for the settings in this report. However, it can also be derived from Figure 6.2 how many geometries are deemed infeasible. If it takes until the 4th/5th generation before 50 feasible individuals are found, then the other individuals do not satisfy the constraints. This reduces in later generations: in between 5-20 geometries are rejected every generation. Of the 700 geometries evaluated only 360-450 geometries satisfy the constraints. Figure 6.4 shows the distribution of the number of times a constraint got violated. Note that some geometries are counted double. For example, most geometries that did not satisfy $C_{\mathrm{nl_{conv}}}(1)$ also violated the other convergence constraints. The last bar shows the total number of rejected nacelles.

The nonlinear geometry constraints $C_{\mathrm{nl}}(1-5)$ mostly get violated in the first few generations. However, this does not apply to cowl thickness constraint $C_{\mathrm{nl}}(4)$. This proved to be the hardest geometry constraint to satisfy, because it depends on multiple variables. The cowl's boattail tends to become thin and sharp for low boattail angles because this increases the boattail length and increases its radius of curvature. This gets aggravated when the core offset or maximum diameter are low. For a short-ducted nacelle, the constraint is mostly violated for the core cowl or for a very short fan cowl. For a long-ducted nacelle, it is also possible to violate the constraint further from the boattail. The fan cowl can become too thin behind the fan casing if the maximum diameter decreases and its position moves more aft. The other constraints are the convergence constraints from the CFD analysis in cruise and take-off. The mass flow residual from constraint $C_{\mathrm{nl_{conv}}}(1)$ is by far the hardest to satisfy. In fact, at most 20 geometries that satisfied the residuals constraints, violated the convergence stability constraints. It is uncertain what caused the slow convergence of the mass flow imbalance since Fluent has been run in batch mode. However, 60-70% of the individuals that violated this constraint occurred in the first four generations. This suggests that a part is due to the randomly generated geometry causing very strong shocks or a creating a bad mesh.

A part of the initially bad generated individuals can be resolved by tightening the bounds. However, it is difficult how much the bounds can be tightened without influencing the design space since no true Pareto front has yet been found. Moreover, the influence of the linear constraints and the bounds in the current settings is difficult to estimate, as every generated geometry already satisfies these settings. It is therefore only possible to determine the margin of the individuals in the last generation to the bounds and linear constraints. If the margin is small, than the bounds constricted this value. This is not an issue with the bounds for the nozzle variables. However, some of the inlet variables such as CR, $\frac{a}{b}$, n and $\frac{A_{\mathrm{fan}}}{A_{\mathrm{max}}}$ are close to the upper or lower bound set. These bounds are not increased because that would give values that deviate a lot from the common values found in the industry and in literature. Moreover, very large values for these variables would cause shock induced boundary layer separation in cruise if viscous effects are taken into account.

The lowest margins for each linear constraint are shown in Table 6.1. The linear constraints that had a margin of less than 10% are highlighted in this table. For case 1, 2 and 3, this only occurs on 1 individual. Moreover, none of the individuals with such as low constraint value have a rank below 3. They are thus further removed from the Pareto front. Only case 4 has several individuals close to the second linear constraint. Lowering this linear constraint at the start of the search would most likely increase the number of individuals that fail $C_{\mathrm{nl}}(4)$. Thus, it seems that the linear constraints and bounds have been set properly: they have constricted the design space but have little influence on the found Pareto front.

Table 6.1 Lowest linear constraint value at generation 13 for each case

	$C_{\mathrm{l}}(1)$ $\beta_{\mathrm{cc}} - \alpha_{\mathrm{c_{in}}} \geq 5°$	$C_{\mathrm{l}}(2)$ $\beta_{\mathrm{fc}} - \alpha_{\mathrm{f_{in}}} \geq 5°$	$C_{\mathrm{l}}(3)$ $A_{\max} - A_{\mathrm{HL}} \geq 0$
case 1	**5.1**	6.06	1.31
case 2	5.74	**5.2**	1.09
case 3	7.25	**5.24**	1.80
case 4	5.79	**5.09**	2.45

6.2 Optimum cruise Geometry

The cruise condition remained the same for all four cases considered. The optimum cruise geometry is the geometry at one end of the Pareto front. Since the flow conditions are the same, it is possible to directly compare the three short-ducted geometries (GM 1.1, GM 3.1 and GM 4.1) with the initial test geometry. Table 6.2 shows the design vector of the different geometries. A more global overview is given in Figure 6.5, where these vectors are used to construct the nacelle geometries.

Table 6.2 Final design variables for the best geometries in cruise condition ($h = 10670\ m$, $M = 0.8$)

	Inlet variables							Nozzle specification	
Parameters	$\frac{a}{b}$	n	MFR	CR	ϕ_i	P_i	$\frac{A_{\mathrm{fan}}}{A_{\max}}$	Duct type	Exit type
Unit	–	–	–	–	°	–	–	–	–
Initial vector	2.46	2.5	0.84	1.05	5.19	0.5	0.71	1	1
GM 1.1	1.85	2.42	0.75	1.16	6.75	0.43	0.68	1	1
GM 3.1	1.89	2.66	0.80	1.11	7.11	0.38	0.69	1	1
GM 4.1	2.47	2.51	0.89	1.06	4.98	0.50	0.73	1	2
	Nozzle variables								
Parameters	$\frac{L_{\mathrm{p}}}{D_{\mathrm{ti}}}$	β_{fc}	β_{cc}	β_{p}	α_{fc}	α_{cc}	$\theta_{\mathrm{c_{cone}}}$	$\mathrm{Offset_{cc}}$	
Unit	–	°	°	°	°	°	°	–	
Initial vector	1.08	26.0	15.5	24.8	12.8	7.4	10.1	0.25	
GM 1.1	1.08	17.5	13.6	36.1	8.8	0.8	6.9	0.17	
GM 3.1	0.52	20.9	10.2	33.3	12.1	0.9	6.05	0.06	
GM 4.1	0.71	24.4	14.0	26.1	19.3	7.9	10.3	0.21	

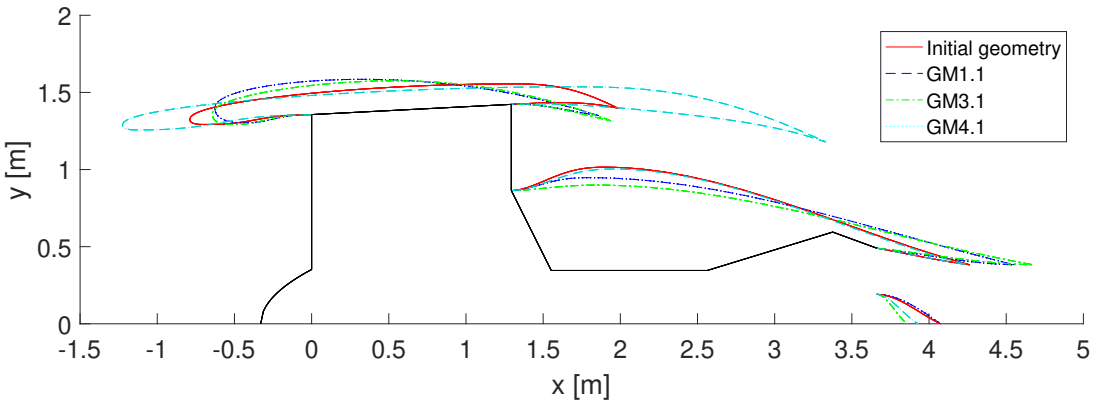

Figure 6.5 Variation in the optimum cruise geometries found for the optimisation of the three short-ducted cases

All three geometries differ greatly from the initial geometry, though case 1 and 3 show a similar trend. The reason for this trend is summarised below:

- A large difference is visible at the upper fan cowl. The length of the bypass duct is only slightly shorter as the initial geometry. However, the maximum diameter has increased and shifted forward. This is in line with the expectations. The expansion of the bypass flow causes an adverse pressure gradient over the fan cowl which leads to flow separation [9]. The forward shift in maximum diameter gives the boattail a larger radius of curvature which may delay flow separation. Both boattail angles are closer to the expected 15° angle [9, 11]. However, the effect of a higher $\frac{D_{\text{HL}}}{D_{max}}$ is two-folded. According to [71] it will lead to supersonic flow over the cowl and lower the critical Mach number. A higher diameter ratio is better for the inlet's low-speed properties as it increases the upper lip radius [30]. Instead, both [30, 72] propose to increase the lip radius, flatten the cowl after the lip and move the maximum diameter to the front. The largest curvature should be at the position of the maximum diameter. This should increase the suction force and improve the low-speed properties of the engine. However, care should be taken that the shock remains ahead of the increased curvature to lower the shock strength [72]. Figures 6.6 and 6.7 show the Mach contour plots of the respective geometries. Geometry GM3.1 shows indeed the strongest shock at the end of the cowl and has a pressure force almost twice as high as GM1.1. This is also shown in the pressure coefficient plotted in Figure 6.9. The pressure coefficient of GM3.1 shows a steep drop at the shock location, whereas this does not appear for GM1.1.

- Both the inlet lip and inlet diffuser is shorter. This reduces the surface area but increases the surface velocity at the throat. The maximum throat Mach number is increased from 0.78 for the initial geometry to 0.82 and 0.85 for GM1.1 and GM1.3 respectively. This gives nearly the same friction drag as the initial geometry (see Table D.1). Moreover, the highlight area has been increased. This is detrimental in cruise, as this increases the difference with the captured freestream area and thus the static pressure at the highlight. The optimum MFR should be close to 1 to have the least ram drag F_{G_1}. The increase in highlight area seems to be lowered to improve the fan cowl as it lowers the diameter ratio $\frac{D_{\text{HL}}}{D_{max}}$. It additionally shortens the duct to move the highlight closer to the position of the maximum diameter.

- Nacelle GM3.1 has a higher NPF in cruise that GM1.1. This difference is due to the core cowl geometry. GM1.1 has a larger offset and core boattail angle. Both cause a quick expansion of the flow and increase the shock strength over the core cowl. The combined pressure and friction drag is 1137 N higher than that for nacelle GM3.1. Still, both geometries have a better core cowl that the initial geometry. The maximum surface Mach number is lowered from 1.64 to 1.4 and 1.49. Moreover, the bypass gross thrust of GM3.1 is higher due to its higher static pressure.

– The core duct is unchoked and thus always convergent. The low flow velocity gives a very low friction drag over the plug. It seems that the plug geometry has hardly any influence on the NPF and that this is the reason that its length can become very small. The conclusion that can be made is that having a plug smaller than the core duct is better than a plug outside of the duct.

The last nacelle, GM4.1, is very different from the other geometries. Its core cowl is nearly identical to that of the initial geometry, but the longer fan cowl creates a CD bypass duct. The outside of fan cowl performs worse than that of GM1.1 and GM3.1. The maximum diameter moves aft and the cowl has a larger surface area. This increases both the pressure and friction drag over the fan cowl. However, this is negated by significantly lower pressure drag over the core cowl. Both Figure 6.10 and 6.10 show that the first shock has completely disappeared due to the internal expansion of the CD duct. The second shock also reduces in strength. Note that the flow for this geometry remains subsonic in the bypass. This lowers the gross thrust compared to the other geometries. The reason is the mass flow inlet boundary condition in Fluent. The total pressure is varied to fit the mass flow and total temperature settings. The final total pressure is 2.7 kPa higher than predicted by the GasTurb analysis. Consequently, the throat area for chocked flow is lower. Keeping the same design vector while lowering the throat area would increase the NPF_{CR} with 2.5 kN. This margin does not have had much impact on the convergence of the cases, as a CD duct already performs better than a convergent duct in cruise. However, for future analysis, it is recommended to update the fixed exhaust areas with the CFD data.

Figure 6.6 Mach contour plot for geometry GM1.1 ($h = 10670\ m$, $M = 0.8$)

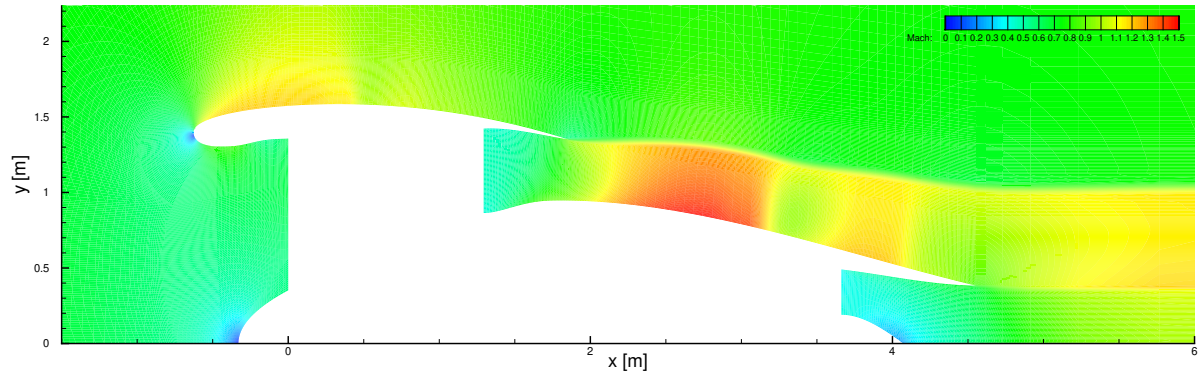

Figure 6.7 Mach contour plot for geometry GM3.1 ($h = 10670\ m$, $M = 0.8$)

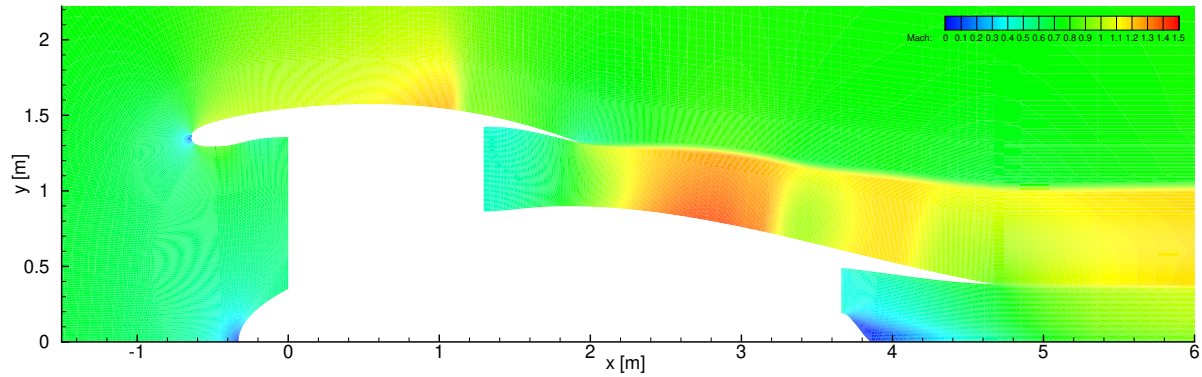

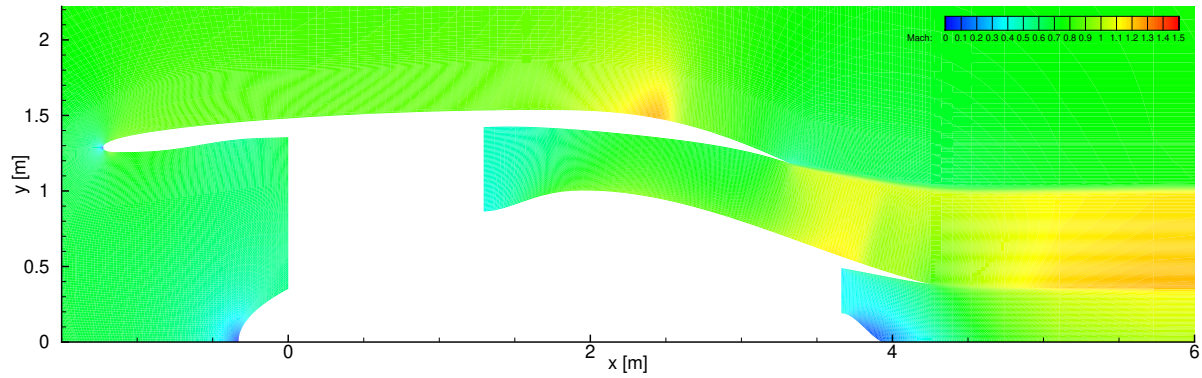

Figure 6.8 Mach contour plot for geometry GM4.1 in cruise conditions

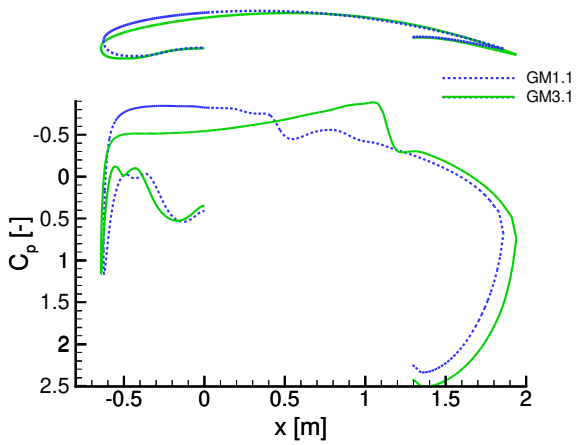

Figure 6.9 Pressure coefficient distribution over the fan cowl of geometry GM1.1 and GM3.1 in cruise conditions

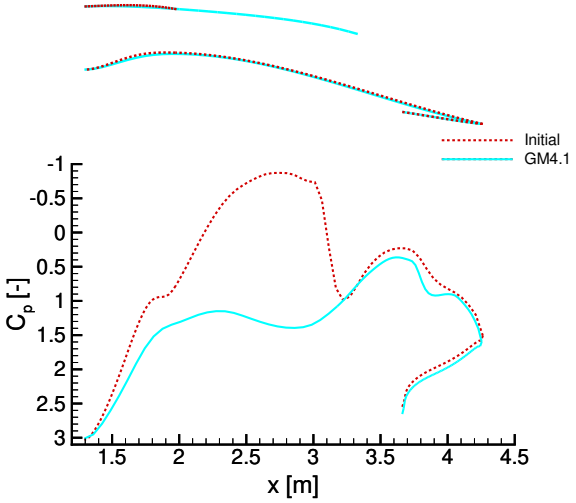

Figure 6.10 Pressure coefficient distribution over the core cowl of the initial geometry and GM4.1 in cruise conditions

6.3 Effect of Mach number on Geometry

In this section the effect of a different take-off Mach number on the nacelle geometry will be discussed. Most nacelles are initially designed for cruise and in later project phases adapted for a better take-off performance. This can be done simultaneously with the developed program, but that makes the selection of the second off-design point more important. The take-off objective is set to midway-of-runway and to end-of-runway conditions by varying the take-off Mach number. Basically, this section compares case 1 and case 3. The focus will lie on nacelles GM1.2, GM1.3, GM3.2 and GM3.3 since these geometries will show the largest differences. The design vectors of these nacelles are shown in Table 6.3 and their geometries are depicted in Figure 6.11. The performance of these nacelles will be discussed first and afterwards it will be related to their respective Pareto front.

Three of these geometries show a similar trend. The geometries with an improved take-off performance all have a large diameter, core cowl offset and round inner lip. The reason for these geometry changes are summarised below:

– The increased highlight area lowered the MFR. In take-off, the lower flight velocity increases the mass flow ratio beyond 1 and the stagnation point shifts to the outer fan cowl. The supervelocities therefore occur on the

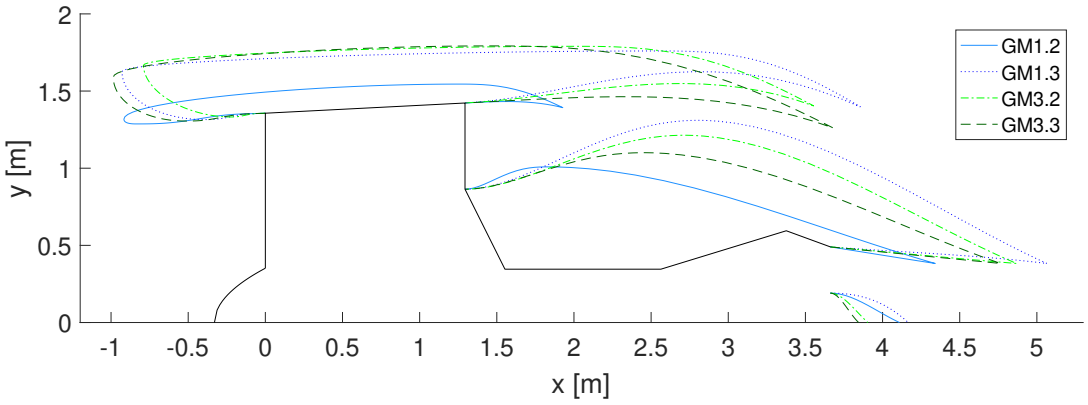

Figure 6.11 Nacelle geometries of case 1 and case 3

Table 6.3 Final design variables for the nacelle geometries in case 1 and 3

	Inlet variables							Nozzle specification	
Parameters	$\frac{a}{b}$	n	MFR	CR	ϕ_i	P_i	$\frac{A_{\text{fan}}}{A_{\max}}$	Duct type	Exit type
Unit	–	–	–	–	°	–	–	–	–
GM 1.2	2.50	2.47	0.85	1.05	4.73	0.50	0.72	1	1
GM 1.3	1.71	2.02	0.56	1.53	5.96	0.41	0.55	1	2
GM 3.2	1.68	1.59	0.54	1.57	6.09	0.40	0.54	1	2
GM 3.3	1.64	2.03	0.59	1.48	5.58	0.43	0.53	1	2

	Nozzle variables							
Parameters	$\frac{L_{\text{p}}}{D_{\text{ti}}}$	β_{fc}	β_{cc}	β_{p}	α_{fc}	α_{cc}	$\theta_{\text{c}_{\text{cone}}}$	$\text{Offset}_{\text{cc}}$
Unit	–	°	°	°	°	°	°	–
GM 1.2	1.18	25.7	16.0	24.8	14.2	8.72	8.98	0.27
GM 1.3	1.32	31.0	24.3	42.6	24.1	6.98	4.37	0.30
GM 3.2	0.64	28.2	23.1	42.2	20.4	4.69	5.08	0.25
GM 3.3	0.48	27.0	19.2	42.2	20.1	5.57	5.56	0.20

inner lip, between the highlight and throat [9]. Both GM1.3 and GM3.3 have a lower $\frac{a}{b}$ and higher CR and n to round the inner lip that prevents shock forming and flow separation. Also P_i is lowered to further round the throat. All these changes are as expected. Figure 6.12 and 6.13 show the Mach contour plots of geometry GM3.3 and GM1.3 in take-off. These measures improve the ram drag F_{G_1} and the hub friction drag. The latter would have increased if the flow separated. This reduces the actual area through which the air flows, so that the velocity is increased over the hub.

– The maximum diameter has increased in response to the increasing highlight area. However, the maximum diameter could not increase any further due to the lower bound. This gives a very flat fan cowl geometry. The more aft maximum diameter also increases the pressure drag as a larger component of the force will be directed in the positive x-direction.

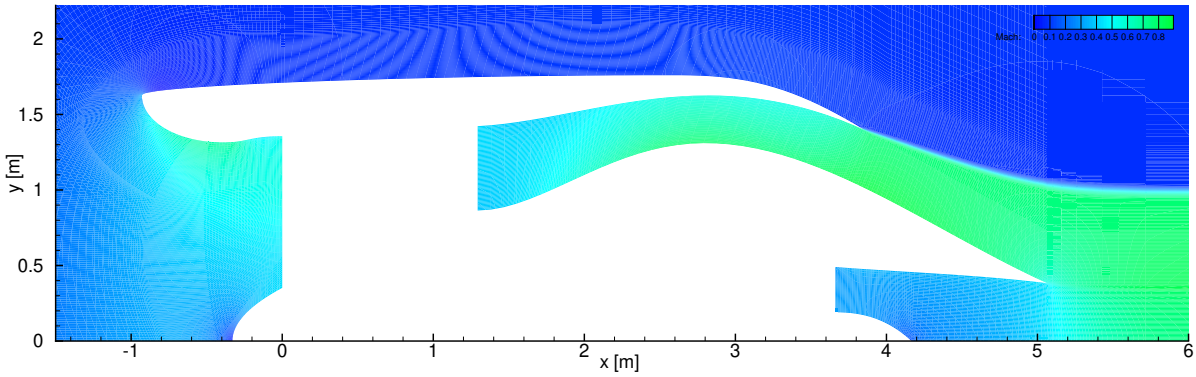

Figure 6.12 Mach contour plot for geometry GM1.3 in take-off conditions ($h = 0\ m$, $M = 0.1$)

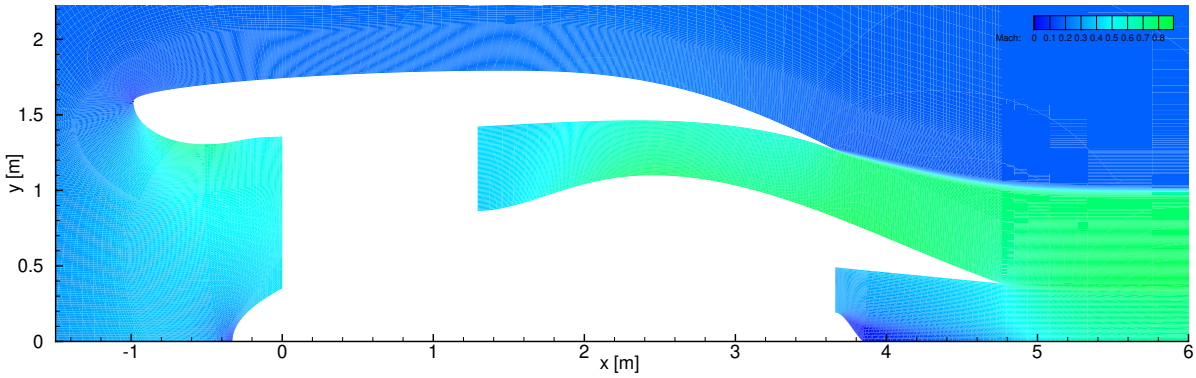

Figure 6.13 Mach contour plot for geometry GM3.3 in take-off conditions ($h = 0\ m$, $M = 0.2$)

– The bypass duct is CD and the core cowl offset and boattail angle has increased. The large boattail angle steepens the core cowls boattail. The increased offset will move the position of the maximum core cowl radius to the front but also increase the radius. Both changes create a long and steep core cowl boattail. The steeper core cowl actually worsens the bypass gross thrust as the axial velocity is reduced. Moreover, the friction drag increases due to the larger dynamic pressure and form factor. However, the CFD analysis for the CD duct gives a larger total pressure in response to the mass flow inlet boundary condition. This , partly, makes up for the loss in bypass thrust. The main advantage is the decrease in pressure drag. The pressure over the core cowl is higher than the freestream pressure. The steeper the core cowl, the more the pressure force is directed forward. Compared to GM4.1, which has a similar total pressure in the same take-off conditions, the pressure force is almost 2000 N higher. All these thrust and drag forces are shown in Table D.4.

It should be noted that the large MFR aggravates the cruise performance. The larger highlight area increases the ram drag considerably. This is countered by the lower pressure drag over the fan cowl. The sharp upper lip quickly increases the flow velocity. The velocity only increases due to the flat surface and aft maximum diameter position so that a large part of the cowl is supersonic. This is terminated by a strong shock. The large negative pressure creates a suction force in the forward direction. However, this result is only possible due to the inviscid Euler analysis. Such a large and strong shock would normally be terminated earlier and cause boundary layer separation. Thus, the actual cruise performance is probably worse than estimated. Moreover, the steeper core cowl creates a stronger shock in cruise compared to geometry GM4.1, which also has a CD bypass duct.

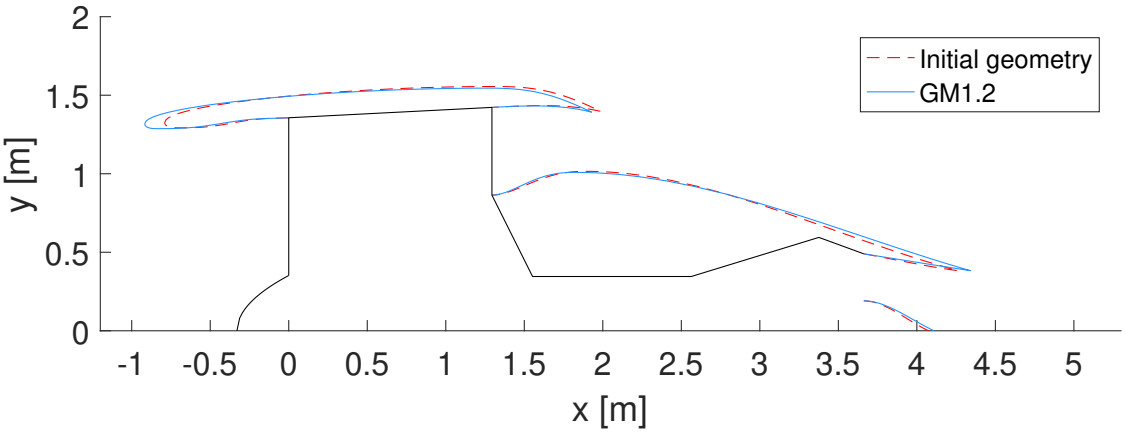

Figure 6.14 Difference in initial geometry and nacelle GM1.2

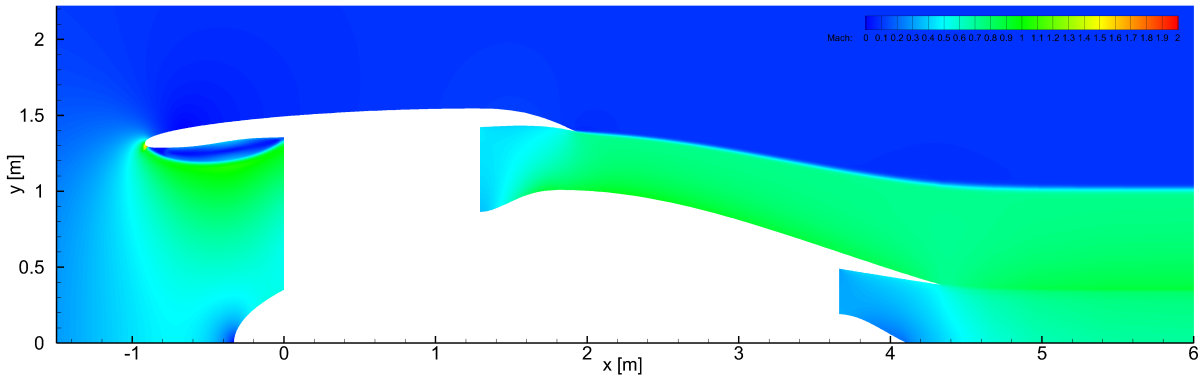

Figure 6.15 Mach contour plot for geometry GM1.2 in take-off conditions ($h = 0\ m$, $M = 0.1$)

The case 1 geometries are shown in blue in Figure 6.11. Geometry GM1.2 lies in the middle of the Pareto front and is a compromise between both objectives. It does not have the thicker and rounder fan cowl the improves the cruise performance of a convergent short-ducted nacelle. Instead its geometry remained very close to the initial geometry, except that the fan cowl is slightly thinner and longer. Both nacelles are plotted in Figure 6.14.

- The total drag in cruise is about the same for the initial geometry and GM1.2, with some minor differences in the separate drag components. The improvement in cruise NPF comes therefore from the gross thrust. The ram drag F_{G_1} is lowered by the increase in MFR. The higher MFR means that the highlight area is closer the captured freestream area, which lowers the pressure term $A(P_{s_1} - P_{s_\infty})$. The bypass and core gross thrust only improved marginally.
- In take-off, the lower highlight area worsens the nacelle's performance. In both cases, the sharp edge induced a high artificial vorticity that caused separation behind the shock in front of the throat. The resulting lower passage area increases the flow and friction drag over the hub, while the lower velocity at the separated inlet contour reduces the friction drag. Care should be taken when this geometry is further analysed as the effect of the separated flow on the fan is not incorporated. It could lower the surge limit and mass flow through the engine and thereby also reduce the thrust. When this does not occur, then the results for the exhaust remain accurate. In which case the largest improvement with respect to the initial geometry comes from the bypass gross thrust. However, the this improvement again seems to stem from a higher total pressure. This is almost 500 Pa higher than the initial geometry. It is unsure why the mass flow inlet boundary condition fluctuates this much, especially since the geometries are so similar.

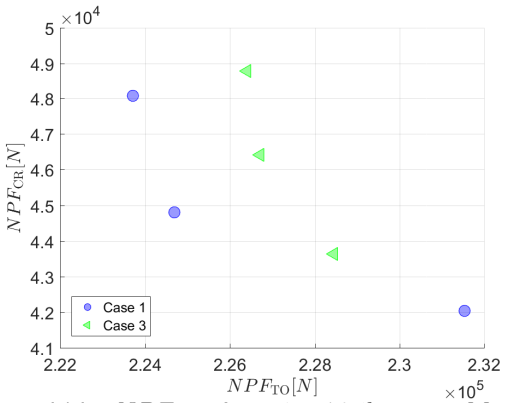

Figure 6.16 NPF_{TO} of case 1 and 3 ($h = 0\ m$, $M = 0.1$)

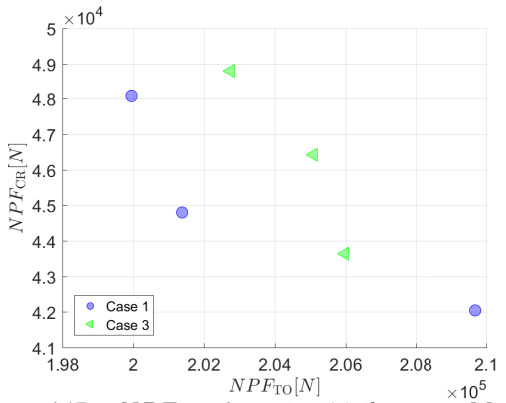

Figure 6.17 NPF_{TO} of case 1 and 3 ($h = 0\ m$, $M = 0.2$)

The performance of these nacelles can only be accurately compared if they are analysed in the same take-off conditions. The three selected geometries are therefore analysed in the other take-off condition. Figures 6.16 and 6.17 show the Pareto front. Their resulting thrust and drag forces are included in Tables D.4 and D.3. It seems that all case 1 geometries, except GM1.3, perform worse than the case 3 geometries for both take-off conditions. Even though the take-off results of case 3 are better, it might not be due to the Mach number settings. The differences in cruise are small and the take-off performance improvement is less than 1.3%. Both cases showed a similar trend in geometry in cruise and take-off. It is therefore expected that the differences in the Pareto front would diminish if the program is run for a longer time. Thus, changing only the Mach number has little effect on the Pareto front.

6.4 Effect of Altitude on Geometry

The other take-off condition that is analysed, is the hot and high condition. This condition refers to take-off on a high altitude during a hot day. This reduces the density and mass flow through the engine. This take-off condition is analysed in case 4 and will be compared to the ISA sea-level take-off condition in case 1 to determine if a different off-design point influences the geometry and convergence of the program. The design vector of the three case 4 geometries that will be discussed, are included in Table 6.4. Figure 6.18 depicts their nacelle contours.

Table 6.4 Final design variables for the nacelle geometries in case 4

	Inlet variables							Nozzle specification	
Parameters	$\frac{a}{b}$	n	MFR	CR	ϕ_i	P_i	$\frac{A_{\mathrm{fan}}}{A_{\mathrm{max}}}$	Duct type	Exit type
Unit	–	–	–	–	°	–	–	–	–
GM 4.1	2.47	2.51	0.89	1.06	4.98	0.50	0.73	1	2
GM 4.2	2.47	2.51	0.89	1.06	4.98	0.50	0.73	1	2
GM 4.3	2.49	2.28	0.84	1.05	5.14	0.48	0.70	1	2

	Nozzle variables							
Parameters	$\frac{L_{\mathrm{p}}}{D_{\mathrm{ti}}}$	β_{fc}	β_{cc}	β_{p}	α_{fc}	α_{cc}	$\theta_{\mathrm{c_{cone}}}$	$\mathrm{Offset_{cc}}$
Unit	–	°	°	°	°	°	°	–
GM 4.1	0.71	24.4	14.0	26.1	19.3	7.94	10.3	0.21
GM 4.2	0.70	24.5	14.0	26.1	19.3	7.90	10.6	0.21
GM 4.3	1.40	27.8	16.2	28.0	18.7	5.53	9.8	0.21

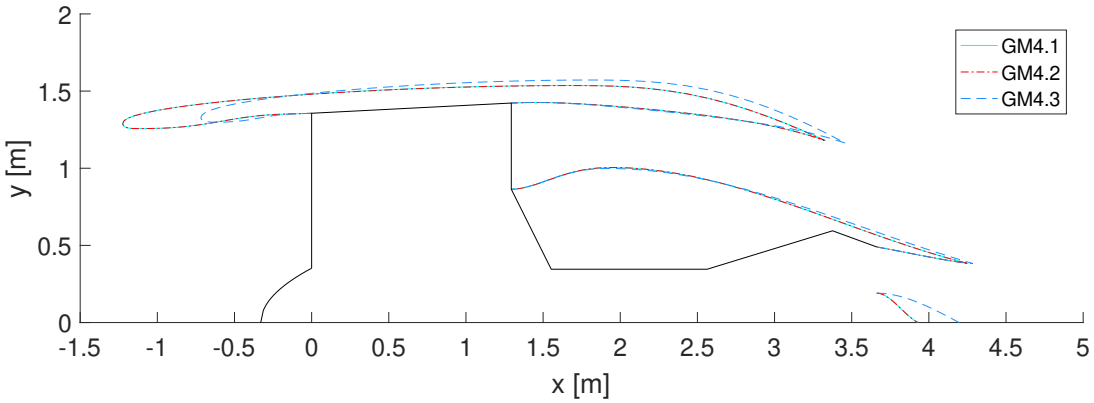

Figure 6.18 Nacelle geometries of case 4

The case 4 take-off condition is more constricting than case 1 or 3. The mass flow, pressure and density have decreased. It means that, for the same Mach number, the actual flow velocity increases. And with it, the influences of the geometry on the pressure drag and gross thrust decreases in take-off. Geometry changes that would quickly reduce the pressure drag in sea-level take-off have less effect in the hot and high condition take-off. This is also visible in the convergence of case 4. The first few generations give a widely spread front. The cruise objective varied from 0.92 to 1.33, but hardly any individual showed improvement in the take-off objective. By the 9th generation, all take-off objectives were in the range of 0.982-1. The cruise objectives of the convergent short-ducted nacelles showed little improvement from the initial geometry and they were quickly replaced. All nacelles in the last generation have a CD duct. Figure 6.1 shows the largest improvement in the cruise objective, but also that the Pareto front is narrow. Especially GM4.1 and GM4.2 have nearly the same propulsive characteristics. The cruise performance of these geometries is discussed in Section 6.2. This section will therefore focus on the take-off performance.

– Again, the lower MFR causes some improvement in ram drag during take-off. This difference is enlarged by the shock induced separation. Geometry GM4.1 and GM4.2 both have a longer inlet and a lower highlight area. It increases the separation bubble in the inlet and lowers the actual passage area further. Both the hub and inlet friction drag are therefore higher. Figures 6.19 and 6.20 show the Mach contour plots for these geometries. The difference in flow velocity at the wall is also captured in Figure 6.21.
– The maximum diameter is slightly increased for GM4.3 in response to the increased highlight area. In fact, the ratio $\frac{R_{\mathrm{HL}}}{R_{max}}$ has been kept the same: 0.84 to 0.846 for geometry GM4.1 and GM4.3 respectively.

Figure 6.19 Mach contour plot for nacelle GM4.1 in take-off conditions ($h = 1655\ m$, $M = 0.1$, $\Delta T_{\mathrm{s_{ISA}}} = 26\ ^{\circ}C$)

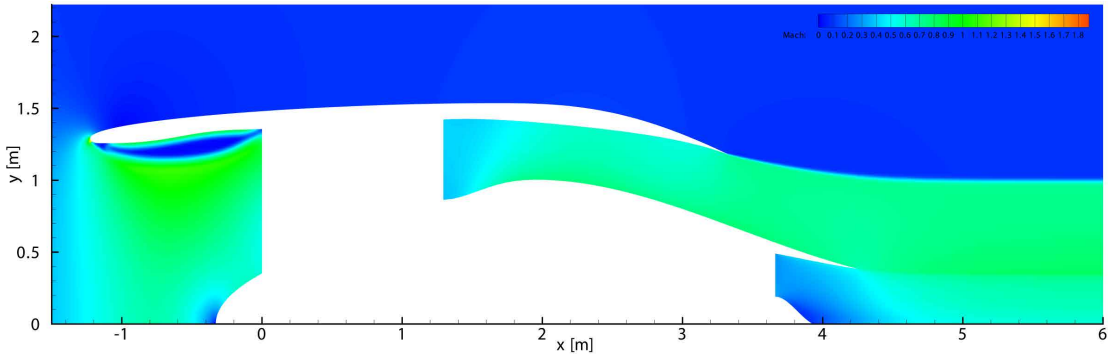

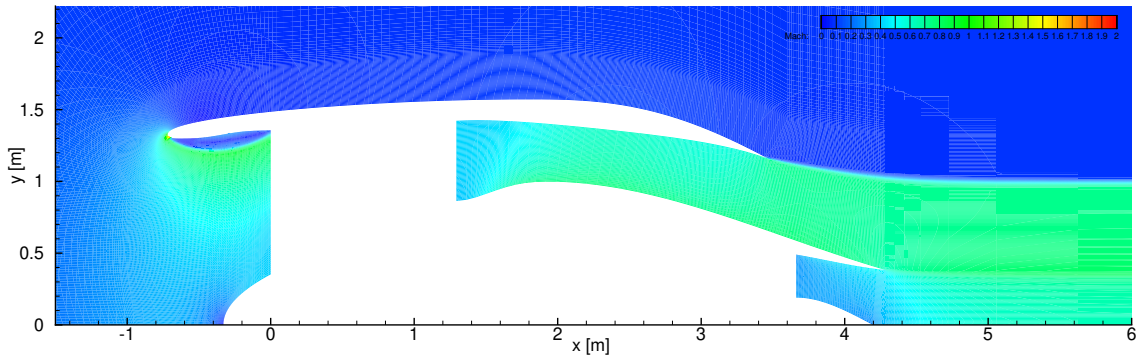

Figure 6.20 Mach contour plot for nacelle GM4.3 in take-off conditions ($h = 1655m$, $M = 0.1$, $\Delta T_{s_{\mathrm{ISA}}} = 26\ ^{\circ}C$)

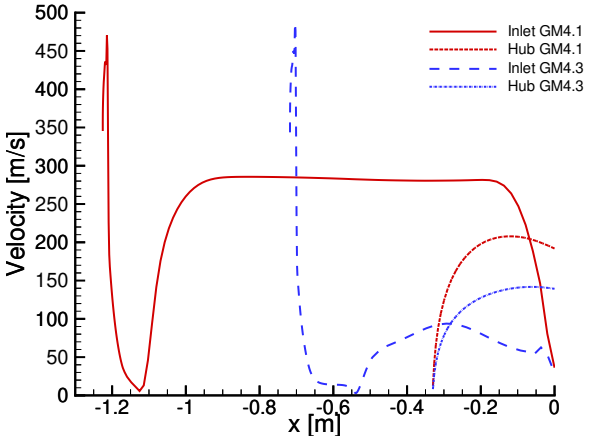

Figure 6.21 Velocity magnitude over the inlet and hub for GM4.1 and GM4.3 ($h = 1655m$, $M = 0.1$)

These three nacelles are analysed in the take-off condition of case 1 to compare the performance. Figures 6.22 and 6.23 show the different Pareto fronts. The case 4 geometries perform better in both conditions than the case 1 nacelles. They even perform better than the case 3 geometries when looking at the plot in Figure 6.16. From all these results, several conclusions can be deducted:

1. A CD duct lowers the flow velocity over the core cowl. It improves the pressure drag more than gross thrust reduces. The same thing applies to the geometries in take-off. GM1.1 and GM1.2 have a higher velocity and pressure drag over the core cowl in take-off than the case 4 geometries.

2. As long as the pressure over the core cowl is positive, the core cowl pressure drag in take-off improves with a higher core cowl offset and boattail angle. It will turn the pressure force in a thrust component. This only holds for a CD duct, since a higher offset for a convergent bypass duct increases the velocity and thus the pressure drag. In contrast, the fan cowl pressure drag worsens. A larger core cowl boattail angle will decrease the boattail's radius of curvature and move the maximum diameter aft. This can be seen when comparing geometry GM4.3 and GM3.3 in Table D.4. Both have a CD duct, but with a big difference in boattail angle and offset. The summation of both pressure drags does not differ much between these geometries. Moreover, the core cowl friction increases and the bypass gross thrust lowers with a steeper cowl. The actual improvement is minimal in take-off.

3. The inlet of GM1.1 and GM1.3 still performs better in take-off than the case 4 geometries due to their rounder nose. However, the nozzle of GM1.1 is slightly worse for the reasons mentioned above. It can be concluded that both cases have geometries with some better aspects which could improve the Pareto front. Case 4 has therefore converged to a local Pareto front as there is little difference in the design vectors.

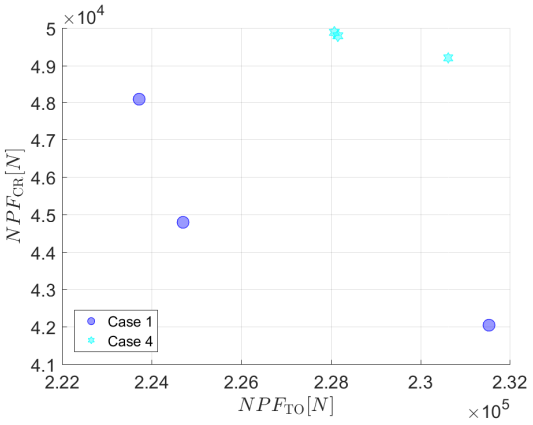

Figure 6.22 NPF of case 1 and 4 for the take-off condition $h = 0\ m$, $M = 0.1$

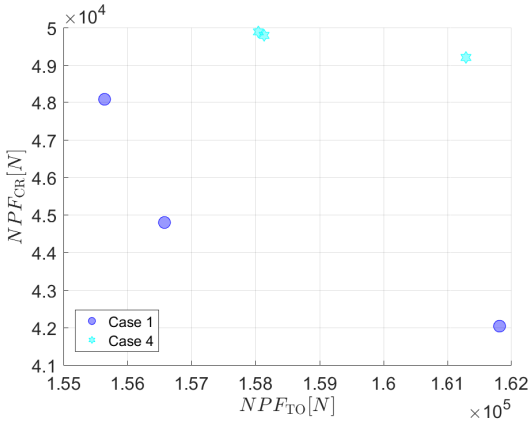

Figure 6.23 NPF of case 1 and 4 for the take-off condition $h = 1655\ m$, $M = 0.1$, $\Delta T_{s_{ISA}} = 25.86\ K$

6.5 Effect of Duct type on Geometry

A long-ducted nacelle is not a logical choice for a high bypass turbofan. The weight of a long-ducted nacelle would counteract any improvement in thrust. It is still analysed from a purely aerodynamic perspective to ensure that the program works appropriately for different duct types. A long-ducted nacelle can be analysed during the same run as a short-ducted nacelle by allowing the integer specifying the duct type to vary. However, it was decided to run them separately for two reasons. Firstly, running the duct types separate allows for a direct comparison between nacelles with nearly the same propulsive forces. Secondly, the initial starting point of the long-ducted nacelle had a much higher cruise NPF. It could cause premature convergence to one of the duct types for the low mutation and population size settings used in this report. As mentioned previously, [44] has shown that an optimised short-ducted nacelle can achieve a thrust specific fuel consumption close (about 0.5%) to that of a free mixer configuration with less than 20% mixing. With an Euler analysis, mixing of the flow would not occur because there is no friction present between the two flow streams. The Pareto front in Figure 6.1 shows the same results, where the optimum cruise geometry for a short-ducted nacelle has nearly the same propulsive characteristics as a long-ducted nacelle. However, due to the different starting points, the short-ducted nacelle needed more generations to converge to this point. The design vectors for the analysed three geometries in this section are included in Table 6.5. Their geometry is shown in Figure 6.24.

Figure 6.24 Nacelle geometries of case 2

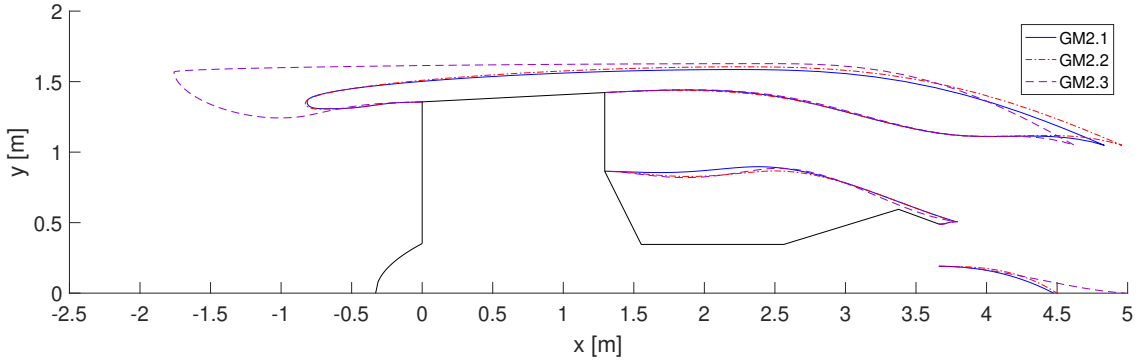

Table 6.5 Final design variables for the nacelle geometries in case 2

	Inlet variables							Nozzle specification	
Parameters	$\frac{a}{b}$	n	MFR	CR	ϕ_i	P_i	$\frac{A_{\text{fan}}}{A_{\max}}$	Duct type	Exit type
Unit	–	–	–	–	°	–	–	–	–
GM 2.1	2.47	2.94	0.80	1.08	4.07	0.50	0.68	2	1
GM 2.2	2.45	2.30	0.82	1.07	4.06	0.50	0.67	2	1
GM 2.3	2.23	1.76	0.60	1.59	6.29	0.28	0.65	2	1

	Nozzle variables									
Parameters	$\frac{L_{\text{p}}}{D_{\text{ti}}}$	β_{fc}	β_{cc}	β_{p}	α_{fc}	α_{cc}	$\theta_{\text{c}_{\text{cone}}}$	Offset_{p}	$\text{Offset}_{\text{cc}}$	$\frac{L_{\text{mxd}}}{D_{\text{mxd}}}$
Unit	–	°	°	°	°	°	°	–		
GM 2.1	2.14	23.3	16.8	27.4	17.5	6.83	7.94	-	0.030	0.46
GM 2.2	2.20	23.3	17.0	32.8	17.7	2.81	9.07	-	0.002	0.52
GM 2.3	3.47	29.5	6.62	3.8	19.2	0.87	7.00	0.05	0.017	0.35

– All nacelles in case 2 are convergent. Fluent's mass flow inlet boundary condition predicts a higher total pressure for a convergent duct than for a CD duct. For example, changing GM2.1 to a CD duct lowers the average total pressure with 2586 Pa. The lower total pressure chokes only the bypass flow as the two exhaust flows don't mix. All in all, the increasing flow velocity from the choked bypass flow is not enough to overcome the higher total pressure of a convergent duct. The gross thrust is 4899 N lower. Moreover, a CD duct for a long-ducted nacelle does not effect the pressure drag, in contrast to a CD bypass duct for short-ducted nacelle. Thus, case 2 converged to a convergent duct to increase the gross thrust.

– Note that the core cowl is very short for all nacelles. It is an effect of the high bypass ratio. The mass flow through the core duct is low, which results in an area at the mixing plane that is only slightly larger than the area after the turbine. Moreover, the core cowl is wrapped tightly around the turbine mount by lowering both the offset and boattail angle. This restrains the core cowls radius and ensures that the fan cowl remains thick enough. As mentioned previously, the thickness constraint $C_{nl}(4)$ can be violated behind the fan casing for very curved bypass ducts.

– The wall angle α_{fc} is close to the expected 15° angle from Figures 3.2 and 3.3. This variable also influences the fan cowl due to the linear constraint on the boattail angles. A larger α_{fc} also results in a larger boattail angle β_{fc}. It can be observed that the design optimisation for the long-ducted nacelle GM2.1 and GM2.2 is very different from GM1.1. The maximum diameter is nearly the same, but its position is further aft and the MFR has increased for the long-ducted nacelle. These three variables create a steeper boattail and flatter fan cowl. Figure 6.25 shows that this causes supervelocities over the upper lip and the boattail in cruise. Especially the higher velocity over the boattail curvature will increase the pressure drag although the total pressure force is still in the forward direction.

The design methodology from [30, 72] is harder to apply to a long-ducted nacelle. Both α_{fc} and β_{fc} have to be lowered to move the maximum diameter to the front. It does improve the pressure drag, but less than this change would on a short-ducted nacelle. Both the curvature and adverse pressure gradient are lower on a long-ducted nacelle due to the longer boattail. Thus, a larger part of the cowl has a high flow velocity even after the forward maximum diameter position. These changes also negatively affect the gross thrust due to the lower α_{fc}. Figure 6.26 shows the Mach contour plot for the changes made to geometry GM2.1. This geometry has the same inlet variables and boattail angles as GM1.1 to move the diameter to the front. The NPF for this geometry is 1.3 kN and 3.4 kN lower than GM2.1 in cruise and take-off respectively.

– The inlet lip of GM2.1 and GM2.2 is long and flat due to the high $\frac{a}{b}$ value and low CR value. This is partly due to the boattail geometry. The aft position of the maximum diameter does not allow for the rounder nose of GM1.1 and GM1.3. Instead, the lip is flatter to reduce the velocity and friction over the inlet wall during cruise. The increase in MFR further improves the ram drag of these geometries in cruise.

  GM2.3 shows the same trend for the inlet as GM1.3 and GM3.3. The MFR is lower to improve the ram drag in take-off whereas the lip is thicker to prevent flow separation. The fan cowl is even flatter than GM1.3, which slightly reduces the pressure drag in take-off compared to GM1.3. It also lowers the pressure drag in cruise significantly as the velocity over the cowl increases. However, the strong shocks due to the flat fan cowl are far from realistic in a viscous flow as it would cause separation. Either a geometry further from the Pareto boundary has to be selected or an additional nonlinear constraint has to be included to constrict the design space more.

– Another difference is that the plug extends out of the tailpipe for GM2.3. The exhaust plane is placed under an angle which increases the static pressure. The gross thrust is higher than GM2.1 and GM2.2, in both cruise and take-off.

Figure 6.25 Mach contour plot for GM2.1 in cruise conditions ($h = 10670\ m$, $M = 0.8$)

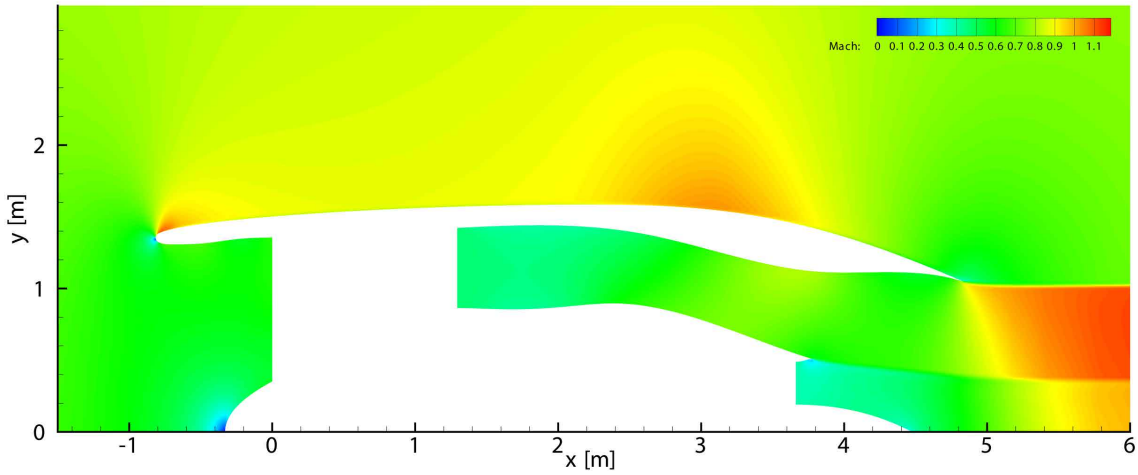

Figure 6.26 Mach contour plot for GM2.1 with adapted inlet variables and boattail angles in cruise ($h = 10670\ m$, $M = 0.8$)

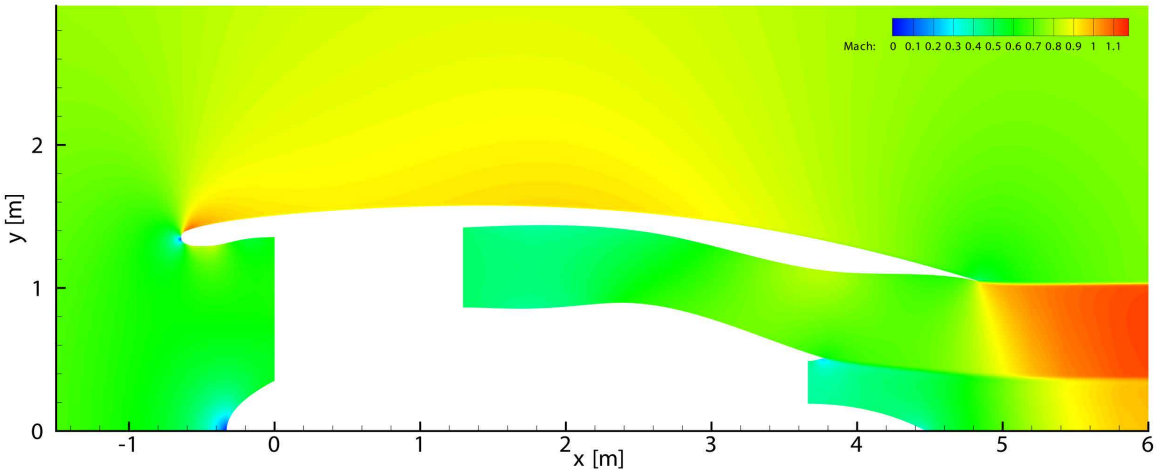

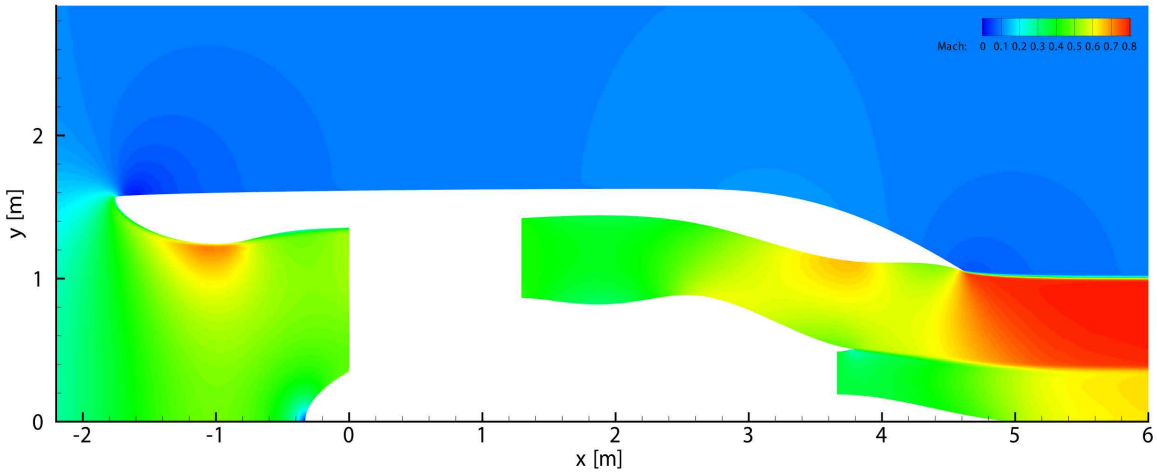

Figure 6.27 Mach contour plot for GM2.3 in take-off conditions ($h = 0\ m$, $M = 0.1$)

7 CONCLUSIONS AND RECOMMENDATIONS

7.1 Conclusions

The nacelle design is a difficult task because it has to meet various requirements. It must be structurally durable and have enough space to contain the engine systems while minimising the impact on the aerodynamic design. The aerodynamic design is time-consuming and is therefore often not extensively analysed with CFD until the last project stages. However, this limits the changes that can be made to the nacelle contour. This report presented a preliminary design method using CFD. A nacelle contour is created with few variables which are then optimised with respect to two objectives using CFD analyses. The objectives were the optimisation of the net propulsive force in cruise and take-off. The resulting Pareto front gives the designer insight into which variables affect performance in different flow conditions. Moreover, the designer retains the possibility to choose the nacelle and determine the importance of one objective over the other.

The little experimental data and nacelle contours available complicated the project. Furthermore, the CFD analysis is limited to a 2D axisymmetric Euler analysis to reduce computational time. A semi-empirical relation approximates the viscous drag using the dynamic pressure obtained from the CFD analysis. It has little influence on the Pareto front because all geometries have the same limitations. Four separate cases were analysed to be able to say more about the behaviour of the optimisation program. Three cases were for a short-ducted nacelle with different take-off conditions. The last case included a long-ducted nacelle. Every case was time-restricted to two days so that 700 geometries were analysed for each case. The nacelle contours are constructed with polynomials and restricted by multiple linear and non-linear constraints to meet the safety, engine, structural and internal spacing requirements. Several conclusions could be made on the nacelle contours:

- The inlet design corresponds with the literature sources. A larger highlight area and smaller inlet lip reduce the ram drag and friction drag during cruise. However, this is unfavourable in the take-off condition as it causes shock induced boundary layer separation. A rounder lip would improve take-off performance. This is achieved by lowering the MFR and $\frac{a}{b}$ and increasing the CR. These differences are reflected in the Pareto front. However, the most optimal take-off condition had such a low MFR that it flattened the fan cowl. This creates strong shocks in cruise, which would normally lead to boundary layer separation. The cruise performance of these geometries is probably even worse than predicted by the Euler analysis.
- The influence of specific nozzle variables is difficult to estimate as they are interdependent. For nacelles with a very short fan cowl, it was beneficial to increase the maximum diameter and position it more forward. This creates a shock over the upper lip but reduces the shock's strength. The thicker upper lip also improves take-off performance. The core cowl can then be flattened to reduce the shock strength over the afterbody. Another option is to extend the fan cowl and create a convergent-divergent bypass duct. The lower exhaust velocity decreases the shock's strength and pressure drag to the extent that it overcame the loss in gross thrust. A convergent-divergent duct also improved take-off performance. Although this was accompanied by a large and steep core cowl to reduce the pressure drag in take-off which would increase the pressure drag in cruise.

– The long-ducted nacelle design differed from the short-ducted nacelle. The actual benefits of this nacelle and a CD short-ducted nacelle, remain to be seen as their increasing weight is not taken into account during this analysis. Furthermore, it is impossible to analyse the thrust increase due to mixing with 2D Euler analyses. The design is limited to free-mixer configurations. The boattail angles had a large influence on the geometry. The resulting nacelles had an inner wall angle in between 12°-15° to increase the gross thrust. This is consistent with the data found from literature. However, this also resulted in a steeper boattail and aft maximum diameter position what increased the flow velocity over the fan cowl. The final Pareto front for this case is identical to the Pareto front found for the short-ducted nacelle. When also the weight is compared, it can be concluded that a short-ducted nacelle performs better for the high bypass ratio engine analysed in this report.

Two sea-level take-off conditions with a Mach number of 0.1 and 0.2 were analysed. The latter had a slightly better Pareto front although this was at most by 1.3% in the take-off net propulsive force. Moreover, the nacelles found for both cases were similar. Increasing the Mach number of the take-off conditions seems to have little effect on the convergence and geometry of the optimisation. The last case analysed was the hot and high take-off condition. This condition was the most constricting due to the mass flow and density decrease. The nacelles found for this condition performed better than those of the other cases. However, this condition also caused it to converge to a local Pareto front where the other cases did not. Either the optimisation settings for this case will have to be adapted or it is recommended to run the former cases for a longer time to let the Pareto front improve.

7.2 Recommendations

The results of this project were limited to the design of a 2D asymmetrical nacelle. With these restrictions, it was possible to obtain a preliminary nacelle design within a short amount of time. However, several nacelle contours or variables have been simplified and need to be included in future analysis. An example is the drooping and scarfing of the inlet to improve the engine performance under higher angles of attack. Also, the installation of the engine has to be analysed in more detail as the interference effect from the pylon and wing would drastically affect the flow around the nacelle. It would be interesting to see how much the geometry changes from the optimum axisymmetric contour when these effects are included.

However, the current optimisation program also has some points to address. The program allows for a simple and quick optimisation of the nacelle. The running time was limited to 2 days in this project. Within this time, the net propulsive force in cruise showed a maximum improvement of 10-14% to the initial nacelle for the three short-ducted nacelle cases. This is less in take-off, only 2-4%. However, the Pareto front found it not yet the completely optimised front. Only 5-7 non-dominated individuals are located on the front and the program still finds several new geometries every generation. Multiple actions are recommended to improve the convergence rate in future analyses:

– The first few geometries are generated randomly by the program if only one geometry is specified as a starting point. The most effective method to improve the converge rate is to define more nacelles to start the optimisation. If more data on nacelles is available, it is even possible to specify all the nacelle geometries in the initial generation. Another option would be to run the program for a longer time, but the former would be more effective and less time-consuming.
– The optimisation is also influenced by the crossover and mutation settings. The mutation was limited, as crossover is the most effective and the run time was limited. However, this is prone to converge to a local Pareto front such as occurred in the hot and high take-off condition. If more time is available or if the initial generation is improved, it is recommended to lower the crossover and/or the mutation operators to prevent the convergence to a local Pareto front.

Bibliography

[1] Parsons School of Design, "My TWA drawing circa 1976," *Figure*, Trans World Airlines, 1976, https://prorepmaster.wordpress.com/2011/09/08/my-twa-drawing-circa-1976/ [Cited on 15 March 2018].

[2] Copperstate Turbine Engine Company, "Honeywell Turbofan Engine Applications," *Webpage*, https://copperstateturbineengineco.aero/honeywell-turbofan-engine-applications/ [Cited on 23 March 2018].

[3] Air Charter Service, "Bombardier Challenger 600 601," *Figure*, http://www.aircharterservice.com/aircraft-guide/private/bombardier-canada/bombardierchallenger600601 [Cited on 23 March 2018].

[4] Pingstone, A., "Eurowings British Aerospace 146-300," *Figure*, 2008, https://commons.wikimedia.org/wiki/File:Eurowings_bae146-300_d-aqua_arp.jpg [Cited on 23 March 2018].

[5] European commission, "Paris Agreement," *Webpage*, 2015, https://ec.europa.eu/clima/policies/international/negotiations/paris_en [Cited on 27 May 2020].

[6] ICAO, "Aircraft Engine Emissions," *Webpage*, 2007, https://www.icao.int/environmental-protection/Pages/aircraft-engine-emissions.aspx [Cited on 24 March 2018].

[7] Torenbeek, E., *Synthesis of Subsonic Airplane Design*, Springer, Dordrecht, Netherlands, 1st ed., 1982, chap. 4.

[8] Savelyeva, A., Zlenko, N., Matyash, E., Mikhaylov, S., and Shenkin, A., "Optimal Design and Installation of Ultra High Bypass Ratio Turbofan Nacelle," *AIAA Journal*, Vol. 24, No. 11, 1986, pp. 1872–1873.

[9] Obert, E., *Aerodynamic Design of Transport Aircraft*, IOS Press BV, Delft, Netherlands, 1st ed., 2009, chap. 37.

[10] Raymer, D. P., *Aircraft Design: A Conceptual Approach*, AIAA, Washington, DC, 2nd ed., 1992, chap. 13.

[11] Dirkzwager, A. M., *An Intake/Nacelle/Exhaust Design Method for Application to Turbofan and Turboprop Engines Operating upto High-Subsonic Freestream Machnumbers*, Master's thesis, Technical University of Delft, Delft, November 1989, Unpublished.

[12] Farokhi, S., *Aircraft propulsion*, John Wiley & Sons, Incorporated, Kansas, USA, 2nd ed., 2014, chap. 3, Retrieved from https://ebookcentral-proquest-com.tudelft.idm.oclc.org on 15 September 2019.

[13] da Conceição, B. S., "Design optimization of the A320 engine inlet cowl," Universidade de Lisboa, Portugal, November 2016, https://fenix.tecnico.ulisboa.pt/downloadFile/1407770020545215/Bruno_Conceicao_64957_Extended_Abstract.pdf [Cited on 23 March 2018].

[14] Tyacke, J. C., Naqavi, I. Z., and Tucker, P. G., "Body Force Modelling of Internal Geometry for Jet Noise Prediction," *Advances in Simulation of Wing and Nacelle Stall–Results of the Closing Symposium of the DFG*

Research Unit FOR 1066, edited by R. Radespiel et al, Springer International Publishing, Braunschweig, Germany, Vol. 131, November 2014, pp. 97–108.

[15] Otting, M., "Survey of Nacelle Design Methods for Turbofan Engines: An Aerodynamic Perspective," Literature review.

[16] El-Sayed, A. F., *Fundamentals of Aircraft and Rocket Propulsion*, Springer, London, England, 1st ed., 2016, chap. 6.

[17] Reddy, D. R., Reddy, E. S., and Moody, R. E., "Aerodynamic Shape Optimization of a Subsonic Inlet Using Three-Dimensional Euler Computation," *Journal of Propulsion and Power*, Vol. 14, No. 2, 1998, pp. 225–233.

[18] Mason, J. G., Farquhar, B. W., Booker, A. J., and Moody, R. E., "Inlet Design Using a Blend of Experimental and Computational Techniques," *Proceedings of the 18th Congress of ICAS*, AIAA, Beijing, China, Vol. 1, 1992, pp. 445–454.

[19] Nangia, R. K. and Palmer, M. E., "Inlet with negative scarf for acoustic reduction, aerodynamic assessment at transonic speed," *18th Applied Aerodynamics Conference*, Denver,CO,USA, Vol. 1, 2000, pp. 692–702.

[20] Crum, T. S., Yates, D. E., Andrew, T. L., and Stockman, N. O., "Low Speed Test Results of Subsonic, Turbofan Scarf Inlets," *29th Joint Propulsion Conference and Exhibit*, Cincinnati, Ohio, Vol. 93–2301, 1993, pp. 692–702.

[21] Federal Aviation Administration, "Design Considerations Minimizing Hazards Caused by Uncontained Turbine Engine and Auxiliary Power Unit Rotor Failure," Advisory Circular 20–128A, FAA, 1997, https://www.faa.gov/documentLibrary/media/Advisory_Circular/AC_20-128A.pdf [Cited on 29 August 2018].

[22] MIDAP study group, "Guide to In-Flight Thrust Measurement of Turbojets and Fan Engines," Tech. rep., Arnold Engineering Development Center, United Kingdom, AGARD AG-237, 1979.

[23] Advisory group for aerospace research and development , "Report of the Working Group on Aerodynamics of Aircraft Afterbody," Tech. rep., AGARD, Neuilly-Sur-Seine, France, AD-A172341, 1986.

[24] Torenbeek, E., *Advanced Aircraft Design: Conceptual design, analysis and optimization of subsonic civil airplanes*, John Wiley & Sons Ltd, Delft University of Technology, Netherlands, 1st ed., 2013, chap. 3.

[25] Trapp, L. G. and Argentieri, H. G., "Evaluation of nacelle drag using Computational Fluid Dynamics," *Journal of Aerospace Technology and Management*, Vol. 2, No. 2, May 2010, pp. 145–154.

[26] ANSYS, Inc., *Ansys Fluent Theory Guide*, SAS IP, Inc., Canonsburg, PA 15317, 17th ed., 2016, chap. 12, 18, 20.

[27] Glasgow, E. R., Divita, J. S., Everling, P. C., and Laughrey, J. A., "Analytical and experimental evaluation of performance prediction methods applicable to exhaust nozzles," *7th Joint Propulsion Conference*, American Institute of Aeronautics and Astronautics, Salt Lake City, UT, USA, Jun 1971, p. 719.

[28] Fujino, M. and Kawamura, Y., "Wave-Drag Characteristics of an Over-the-Wing Nacelle Business-Jet Configuration," *Journal of Aircraft*, Vol. 40, No. 6, 2003, pp. 1177–1184.

[29] Young, A. D. and Paterson, J. H., "Aircraft Excrescence Drag," Tech. rep., AGARD, Neuilly-Sur-Seine, France, AD-A106030, 1981.

[30] Wittenberg, H., *Voortstuwing van vliegtuigen deel 1*, Dictaat 130, Technische Hogeschool Delft, Delft, 1986, chap. 3,4.

[31] Hoerner, S. F., *Fluid-Dynamic Drag: Practical information on aerodynamic drag and hydrodynamic resistance*, Hoerner Fluid Dynamics, Bakersfield, CA, 2nd ed., 1965, chap. 2,5,8,16.

[32] Desktop Aeronautics, Inc, *Aircraft Design: Synthesis and Analysis*, Desktop Aeronautics, Inc, Stanford, CA 94309, 0th ed., 2001, chap. 4, Retrieved from http://rahauav.com/Library/Design-performance/Aircraft%20Design,%20synthesis%20and%20analysis.pdf on 7 January 2020.

[33] Petit, J. and Scholey, M., "STOL Transport Thrust Reverser/Vectoring Program: Volume I," Tech. rep., Boeing Company, Ohio, USA, AFAPL-TR-72-109, 1972.

[34] Ball, W., "Propulsion System Installation Corrections Volume IV: Bookkeeping Definition-Data Correlations," Tech. rep., The Boeing Company, Ohio, USA, AFFDL-TR-72-147-Vol.IV, 1972.

[35] Samareh, J. A., "Survey of Shape Parameterization Techniques for High-Fidelity Multidisciplinary Shape Optimisation," *AIAA Journal*, Vol. 39, No. 5, 2001, pp. 877–884.

[36] Saxena, A. and Sahay, B., *Computer Aided Engineering Design*, Springer, Kanpur, India, 1st ed., 2005, chap. 4,5.

[37] Kulfan, B. M. and Bussoletti, J. E., ""Fundamental" Parametric Geometry Representations for Aircraft Component Shapes," *11th AIAA/ISSMO Multidisciplinary Analysis and Optimization Conference*, AIAA, Vol. 6948, September 2006, pp. 157–176.

[38] Kowe, D. C. and Wynosky, T. A., "Energy Efficient Engine Program: Advanced Turbofan Nacelle Definition Study," NASA CR-174942, NASA, May 1985, https://ntrs.nasa.gov/archive/nasa/casi.ntrs.nasa.gov/19900019244.pdf [Cited on 1 April 2018].

[39] GmbH, G., Software Packagetype, Aachen, Germany, address, version, "GasTurb," . 2019.

[40] Cousins, W. and Davis, M. W., "Evaluating Complex Inlet Distortion With a Parallel Compressor Model: Part 1–Concepts, Theory, Extensions, and Limitations," *Proceedings of the ASME Turbo Expo: Power for Land, Sea, and Air*, ASME, Vancouver, Canada, Vol. 1, 2011, pp. 1–12.

[41] Mehdi, A., *Effect of swirl distortion on gas turbine operability*, Master's thesis, Cranfield University, May 2014, https://dspace.lib.cranfield.ac.uk/bitstream/handle/1826/12129/Mehdi_A_2014.pdf?sequence=1&isAllowed=y [Cited on 31 August 2018].

[42] Lei, Z., Zhang, Y., Zhu, Z., and Zhu, J., "Numerical research on the mixing mechanism of lobed mixer with inlet swirl in linear radial distribution," *Proceedings of the Institution of Mechanical Engineers*, Vol. 229, No. 3, 2015, pp. 280–297.

[43] Lei, Z., Mahallati, A., Cunningham, M., and Germain, P. D., "Effects of Core Flow Swirl on the Flow Characteristics of a Scalloped Forced Mixer," *Proceedings of ASME Turbo Expo: Turbine Technical Conference and Exposition*, ASME, Vol. 134, June 2011, pp. 451–463.

[44] Kozlowski, H. and Larkin, M., "Energy Efficient Engine Exhaust Mixer Model Technology Report," NASA CR-165459, NASA, March 1982, https://ntrs.nasa.gov/archive/nasa/casi.ntrs.nasa.gov/19820014390.pdf [Cited on 8 February 2020].

[45] Douglass, W. M., "Aerodynamic Installation of High-Bypass-Ratio Fan Engines," *National Aeronautic and Space Engineering and Manufacturing Meeting*, SAE International, SAE Technical Paper 660732, feb 1966.

[46] Masure, B., "Problems de mesure sur maquette de la poussee d'un arriere-corps d'avion supersonique tuyeres de reference," *Inlets and Nozzles for Aerospace Engines*, AGARD, Advanced Marine Vehicles Conferences, Dec 1971, pp. 4.1–4.15.

[47] Albers, J. A. and Miller, B. A., "Effect of Subsonic Inlet Geometry on Predicted Surface and Flow Mach Number Distributions," Tech. rep., NASA, Ohio, USA, NASA TN D-7446, 1973.

[48] Miller, B. A., Dastoli, B. J., and Wesoky, H. L., "Effect of Entry-Lip Design on Aerodynamics and Acoustics of High-Throat-Mach-Number Inlets for the Quiet, Clean, Short-haul Experimental Engine," NASA TM X-3222, NASA, May 1975, https://ntrs.nasa.gov/search.jsp?R=19750014206 [Cited on 1 April 2018].

[49] Albers, J. A. and Felderman, E. J., "Boundary-Layer Analysis of Subsonic Inlet Diffuser Geometries for Engine Nacelles," Tech. rep., NASA, Ohio, USA, NASA TN D-7520, 1974.

[50] Payne, P. R., "Afterbody Drag Volume 1: Drag of Conical and Circular Arc Afterbodies without Jet Flow," Tech. rep., Defense Technical Information Center, Annapolis, Maryland, AD-A087514, 1980.

[51] Stańkowski, T. P., MacManus, D. G., Sheaf, C. T., and Christie, R., "Aerodynamics of aero-engine installation," *Proceedings of the Institution of Mechanical Engineers, Part G: Journal of Aerospace Engineering*, Vol. 230, No. 14, 2016, pp. 2673–2692.

[52] Peters, A., Spakovszky, Z. S., Lord, W. K., and Rose, B., "Ultrashort Nacelles for Low Fan Pressure Ratio Propulsors," *Journal of Turbomachinery*, Vol. 137, No. 2: 021001, Sept 2014.

[53] Hirsch, C., *Numerical Computation of Internal and External Flows: The Fundamentals of Computational Fluid Dynamics*, Elsevier Butterworth-Heinemann, Amsterdam, 2nd ed., 2007, chap. 6.

[54] Petrusson, A., *Aerodynamic Evaluation of Nacelles for Engines with Ultra High Bypass Ratio*, Master's thesis, Chalmers University of Technology, Februari 2017, http://publications.lib.chalmers.se/records/fulltext/247917/247917.pdf [Cited on 6 May 2020].

[55] Du, K.-L. and Swamy, M. N. S., *Search and Optimization by Metaheuristics: Techniques and Algorithms Inspired by Nature*, Springer International Publishing, Montreal, Canada, 2016, chap. 2,3,4,6.

[56] Deb, K., Pratap, A., Agarwal, S., and Meyarivan, T., "A fast and elitist multiobjective genetic algorithm: NSGA-II," *IEEE Transactions on Evolutionary Computation*, Vol. 6, No. 2, 2002, pp. 182–197.

[57] Weather Spark, "Average Weather at Denver International Airport," *Webpage*, 2020, https://weatherspark.com/y/145689/Average-Weather-at-Denver-International-Airport-Colorado-United-States-Year-Round#Sections-Temperature [Cited on 4 June 2020].

[58] Gray, D. E. and Gardner, W. B., "Energy Efficient Engine Program: Technology Benefit/Cost Study, volume 2," NASA-CR-174766-VOL-2, NASA, Oct 1983, https://ntrs.nasa.gov/archive/nasa/casi.ntrs.nasa.gov/19900019249.pdf [Cited on 9 April 2020].

[59] The Boeing Company, "Study and development of turbofan nacelle modifications to minimize fan-compressor noise radiation. Volume 4 - Flightworthy nacelle development," NASA CR-1714, NASA, Jan 1971, https://ntrs.nasa.gov/archive/nasa/casi.ntrs.nasa.gov/19710008193.pdf [Cited on 20 April 2020].

[60] Bielak, G. W., Premo, J. W., and Hersh, A. S., "Advanced Turbofan Duct Liner Concepts," NASA/CR-1999-209002, NASA, Feb 1999, https://ntrs.nasa.gov/archive/nasa/casi.ntrs.nasa.gov/19990028621.pdf [Cited on 20 April 2020].

[61] Maddock, I., Harby, A., Kemp, P., and Wood, P. J., *Ecohydraulics : An Integrated Approach*, John Wiley & Sons, Incorporated, Hoboken, United Kingdom, 1st ed., 2013, chap. 3.

[62] ANSYS, Inc., "Ansys Fluent User's Guide," *Webpage*, Ansys, Inc., 2009.

[63] Schaffer, J., Caruana, R., Eshelman, L., and Das, R., "A Study of Control Parameters Affecting Online Performance of Genetic Algorithms for Function Optimization," *Proceedings of the 3rd international conference on genetic algorithms*, Morgan Kaufmann Publishers Inc., San Mateo, California, USA, June 1989, pp. 51–60.

[64] Mills, K. L., Filliben, J. J., and Haines, A. L., "Determining Relative Importance and Effective Settings for Genetic Algorithm Control Parameters," *Evolutionary Computation*, Vol. 23, No. 2, 2015, pp. 309–342.

[65] Matlab, "gamultiobj," *Webpage*, 2020, p. 1, https://nl.mathworks.com/help/gads/gamultiobj.html#bvf79ug-2 [Cited on 18 May 2020].

[66] Jane's Group UK, "Aero-Engines – Turbofan," *Jane's aero engines*, IHS Markit, 2020, https://janes.ihs.com/AeroEngines [Retrieved on 16 June 2020].

[67] Pratt & Whitney, "Commercial Engines," Raytheon Technologies Corporation, 2020, https://prattwhitney.com/products-and-services/products/commercial-engines/ [Retrieved on 16 June 2020].

[68] EASA, "Type Certificate data sheet for Engine LEAP-1A & LEAP-1C series engines," *EASA*, Vol. E.110, No. 2, 2016, pp. 1–11, https://www.easa.europa.eu/sites/default/files/dfu/EASA%20E%20110%20TCDS%20Issue%202%20LEAP-1A_1C_20161103_1.0.pdf [Cited on 16 June 2020].

[69] EASA, "Type Certificate data sheet for RB211 Trent 900 series engines," *EASA*, Vol. E.012, No. 10, 2019, pp. 1–20, https://www.easa.europa.eu/sites/default/files/dfu/TCDS%20E.012_Issue%2010.pdf [Cited on 16 June 2020].

[70] Daggett, D. L., Brown, S. T., and Kawai, R. T., "Ultra-Efficient Engine Diameter Study," NASA CR–2003-212309, NASA, May 2003, https://ntrs.nasa.gov/search.jsp?R=20030061085 [Cited on 20 June 2020].

[71] Hancock, J. P. and Hinson, B. L., "Inlet Development for the L-500," *5th Propulsion Joint Specialist Conference*, AIAA, Colorado, USA, Vol. 69–448, June 1969, pp. 1–12.

[72] Langley, M. L., "The Design of Axisymmetric Cowls for Podded Nacelles for High By-pass Ratio Turbofan Engines," *Aeronautical Research Council, Reports & Memoranda*, Vol. 2, No. 3846, 1979, pp. 1–81.

APPENDIX A

CUSTOM MATLAB CROSSOVER FUNCTION

```
%%%%%%%%%%%%%%%%%%%%%%%%%%%%%%%%%%%%%%%%%%%%%%%%
% This function uses crossover to create the new population of the
% multiobjective GA, taking integers and bounds into account.
% reference: Kalyanmoy Deb, Amrit Pratap, Sameer Agarwal, and T. Meyarivan,
%            " A Fast and Elitist Multiobjective Genetic Algorithm: NSGA-II",
%            IEEE TRANSACTIONS ON EVOLUTIONARY COMPUTATION, VOL. 6, No. 2,
%            APRIL 2002.).
% Input:  GA options structure, number of variables, integer index, and the
%         current population.
% Output: children matrix
%%%%%%%%%%%%%%%%%%%%%%%%%%%%%%%%%%%%%%%%%%%%%%%%
function xoverKids  = int_crossoverarithmetic(parents,options,GenomeLength,...
                                              FitnessFcn,unused,thisPopulation)
%% SBX cross over operation incorporating boundary constraint
global IntCon etac
N         = length(parents)            ; % Number of children to produce
xl        = options.PopInitRange(1,:)' ; % Lower bound
xu        = options.PopInitRange(2,:)' ; % Upper bound
Aineq_mat = options.LinearConstr.Aineq ; % Linear inequality constraint matrix
bineq     = options.LinearConstr.bineq ; % Linear inequality

% allocate space to matrix
xoverKids = zeros(N/2,GenomeLength); %every row is one child, variables by column

for i=1:(N/4)
    %get two parents for crossover from the tournament selection
    parent1 = thisPopulation(parents(2*i-1),:);
    parent2 = thisPopulation(parents(2*i),:);

    if (isequal(parent1,parent2))==1
        %mutate parents instead for next generation
        mutationChildren   = int_mutation([parents(2*i-1),parents(2*i)], ...
                             options, GenomeLength, 0, 0, 0, thisPopulation);
        xoverKids(2*i-1,:) = mutationChildren(1,:); %child 1
        xoverKids(2*i,:)   = mutationChildren(2,:); %child 2
```

```
    else
        for j = 1: GenomeLength
            %calculate the spread factor betaq. >1 expanding, <1 contracting
            if parent1(j)<parent2(j)
               beta(j) = 1+(2/(parent2(j)-parent1(j)))*...
                         (min((parent1(j)-xl(j)),(xu(j)-parent2(j))));
            else
               beta(j) = 1+(2/(parent1(j)-parent2(j)))*...
                         (min((parent2(j)-xl(j)),(xu(j)-parent1(j))));
            end
        end
        u                  = rand(1,GenomeLength); %random vector
        alpha              = 2-beta.^-(etac+1)   ;
        alpha(isnan(alpha))= 2                   ; % set to 0 due for integers
        betaq              = (u<=(1./alpha)).*(u.*alpha).^(1/(etac+1))+...
                             (u>(1./alpha)).*(1./(2 - u.*alpha)).^(1/(etac+1));

        xoverKids(2*i-1,:) = 0.5*(((1 + betaq).*parent1) +...
                             (1 - betaq).*parent2); %child 1
        xoverKids(2*i,:)   = 0.5*(((1 - betaq).*parent1) +...
                             (1 + betaq).*parent2); %child 2

        % Satisfy inequality constriants
        Constineq = Aineq_mat*xoverKids(2*i-1:2*i,:)'-bineq; % Constraint values
        [Violated_row,Violated_col] = find(Constineq>0) ; % violated constraints
        for k=1:length(Violated_row)
            % adapt constraints one by one
            viol_const        = Constineq(Violated_row(k),Violated_col(k));
            Aineq_nonzero_col = find(Aineq_mat(Violated_row(k),:)~=0);
            failsafe_loop     = 1.;
            while viol_const >=0 && failsafe_loop<=100
              %generate new random numbers untill constraint are satisfied
              u                  = rand(1,length(Aineq_nonzero_col));
              alpha              = 2-beta(Aineq_nonzero_col).^-(etac+1)   ;
              alpha(isnan(alpha))= 2        ;
              betaq              = (u<=(1./alpha)).*(u.*alpha).^(1/(etac+1))+...
                                   (u>(1./alpha)).*(1./(2 - u.*alpha)).^(1/(etac+1));

              xoverKids(2*i-(2-Violated_col(k)),Aineq_nonzero_col) =...
                        0.5*(((1 +(-1)^(Violated_col(k)+1)*betaq).*...
                        parent1(Aineq_nonzero_col)) + (1 +(-1)^...
                        (Violated_col(k))* betaq).*parent2(Aineq_nonzero_col));
              viol_const    = Aineq_mat(Violated_row(k),:)*xoverKids(2*i-...
                              (2-Violated_col(k)),:)'-bineq(Violated_row(k));
              failsafe_loop = failsafe_loop+1;
            end
        end
    end
end
% Satisfy integers
xoverKids(:,IntCon) = round(xoverKids(:,IntCon));
end
```

APPENDIX B

CUSTOM MATLAB MUTATION FUNCTION

```
%%%%%%%%%%%%%%%%%%%%%%%%%%%%%%%%%%%%%%%%%%%%%%%%%%%%
% This function applies mutation to the parents to create
% the new population of the multiobjective GA, taking integers and bounds
% into account.
% reference: Kalyanmoy Deb, Amrit Pratap, Sameer Agarwal, and T. Meyarivan,
%            " A Fast and Elitist Multiobjective Genetic Algorithm: NSGA-II",
%            IEEE TRANSACTIONS ON EVOLUTIONARY COMPUTATION, VOL. 6, No. 2,
%            APRIL 2002.).
% Input:  GA options structure, number of variables, integer index, index
%         of selected parents. Parents have been randomly selected from a
%         group of the previous population by matlab's built-in
%         tournament selection function.
% Output: mutated child
%%%%%%%%%%%%%%%%%%%%%%%%%%%%%%%%%%%%%%%%%%%%%%%%%%%%

function mutationChildren = int_mutation(parents, options, GenomeLength, ...
    ~, ~, ~, thisPopulation)

%% Input variables
global IntCon etam
N         = length(parents)           ; % Number of children to produce
xl        = options.PopInitRange(1,:) ; % Lower bound
xu        = options.PopInitRange(2,:) ; % Upper bound
Aineq_mat = options.LinearConstr.Aineq; % Linear inequality constraint matrix
bineq     = options.LinearConstr.bineq; % Linear inequality

%% Polynomial mutation including boundary constraint
mutationChildren = zeros(N,GenomeLength)       ; % Allocate space for matrix

for i=1:N
    Parent       = thisPopulation(parents(i),:); % parent used for mutation
    u            = rand(1,GenomeLength)        ; % Random vector for mutation
    mut_dec_var  = min((Parent-xl),(xu-Parent))./...
                   (xu-xl)                     ; % mutation variable
    mut_dec_var(IntCon(:))=0.0                 ; % No mutation for integer values
```

```
    delq = (u<=0.5).*((((2*u)+((1-2*u).*((1-mut_dec_var).^(etam+1) ))).^...
        (1/(etam+1)))-1) + ...
        (u>0.5).*(1-((2*(1-u))+(2*(u-0.5).*((1-mut_dec_var).^(etam+1))))).^...
        (1/(etam+1)))                                ; % mutation factor

    mutationChildren(i,:) = Parent + delq.*(xu-xl) ; % mutated child


    %Get the linear inequality constraint values:
    Constineq = Aineq_mat*(mutationChildren(i,:)')-bineq;% Constraint values
    [Violated_row,~] = find(Constineq>0)                ;% violated constraints

    for k=1:length(Violated_row)
        % adapt constraints one by one
        viol_const = Constineq(Violated_row(k));
        Aineq_nonzero_col = find(Aineq_mat(Violated_row(k),:)~=0);
        mut_dec_var_ineq  = mut_dec_var(Aineq_nonzero_col); % mutation variable
        failsafe_loop = 1;
        while viol_const >=0 && failsafe_loop<=100
            %generate new random numbers for the variables that violate the
            %constraints untill statisfied
            u             = rand(1,length(Aineq_nonzero_col)) ;
            delq(Aineq_nonzero_col) = (u<=0.5).*((((2*u)+((1-2*u).*...
                   ((1-mut_dec_var_ineq).^(etam+1) ))).^(1/(etam+1)))-1) + ...
                   (u>0.5).*(1-((2*(1-u))+(2*(u-0.5).*((1-mut_dec_var_ineq)...
                   .^(etam+1))))).^(1/(etam+1))) ;

            mutationChildren(i,:) = Parent + delq.*(xu-xl) ;
            viol_const = Aineq_mat(Violated_row(k),:)*(mutationChildren(i,:)')...
                         -bineq(Violated_row(k));
            failsafe_loop = failsafe_loop+1;
        end
    end
end

% Satisfy integers
mutationChildren(:,IntCon) = round(mutationChildren(:,IntCon));
end
```

APPENDIX C
ENGINE CYCLE DATA

C.1 Design input to GasTurb 12

Ambient conditions			Nozzle data		
Altitude	m	10670	Core Nozzle Thrust Coeff		1
Delta T from ISA	K	0	Bypass Nozzle Thrust Coeff		1
Relative Humidity	$\%$	0	Design Core Nozzle Angle	°	10.13
Mach Number		0.8	Design Bypass Nozzle Angle	°	11.8
Basic data			**Secondary Air system**		
Intake Pressure Ratio		1	Rel. Handling Bleed to Bypass		0
Inner Fan Pressure Ratio		1.53	Rel. HP Leakage to Bypass		0
Outer Fan Pressure Ratio		2.7775	Rel. Overboard Bleed W_Bld/W25		0.01
Compr. Interduct Press. Ratio		1	Rel. Enthalpy of Overb. Bleed		1
HP Compressor Pressure Ratio		22.9844	Bleed Recirculating to		0
Bypass Duct Pressure Ratio		1	Number of HP Turbine stages		2
Turb. Interd. Ref. Press. Ratio		1	HPT NGV Cooling Air /W25		0.029
Design Bypass Ratio		12.8	HPT Rotor 1 Cooling Air / W25		0.0135
Burner Exit Temperature	K	1602.15	HPT NGV Cooling Air /W25		0.0085
Burner Design Efficiency		0.995	HPT Rotor 2 Cooling Air / W25		0.02162
Burner Partload Constant		1.6	HPT Cool Air Pumping diameter	m	0
Fuel Heating Value	$\frac{MJ}{kg}$	43.124	Number of LP Turbine stages		5
Overboard Bleed	$\frac{kg}{s}$	0	LPT Rotor cooling Air W_Cl/W25		0.00249
Power Offtake	kW	55.29	Rel. Enth. of LPT Cooling Air		0.6
HP Spool Mech. Efficiency		1	Rel.HP Leakage to LPT exit		0
LP Spool Mech. Efficiency		1	Rel. Fan Overb.Bleed W_Bld/W13		0
Burner Pressure Ratio		0.95251	Core-Byp Heat Transf Effectiveness		0
Turbine Exit Duct Press Ratio		0.995	Coolg Air Cooling Effectiveness		0
Mass Flow Corr. W2Rstd	$\frac{kg}{s}$	11083.632	Bleed Air Cooling Effectiveness		0

Compressor and turbine data					
Polytr.Inner LPC Efficiency		0.912	Polytr.HPC Efficiency		0.93094
Polytr.Outer LPC Efficiency		0.922	HPC Tip Speed	$\frac{m}{s}$	440
LPC Tip Speed	$\frac{m}{s}$	356	HPC Inlet Radius Ratio		0.49
LPC Inlet Radius Ratio		0.26	HPC Inlet Mach Number		0.46
LPC Inlet Mach Number		0.59	min HPC Hub Diameter	m	0
Engine Inl/Fan Tip Diam Ratio		1	Isentr.HPT Efficiency		0.927
min LPC Hub Diameter	m	0.7053	Isentr.LPT Efficiency		0.944

C.2 GasTurb output at cruise condition

Station	W kg/s	T K	P kPa	WRstd kg/s
amb		218.79	23.835	
1	419.918	246.86	36.343	
2	419.918	246.86	36.343	1083.632
13	389.489	281.67	55.604	701.723
21	30.429	339.87	100.943	33.172
25	30.429	339.87	100.943	33.172
3	30.353	856.82	2320.120	2.286
31	27.839	856.82	2320.120	
4	28.464	1602.15	2209.937	3.077
41	29.681	1573.82	2209.937	3.180
43	29.681	1121.64	447.150	
44	30.673	1113.58	447.150	
45	30.673	1113.58	447.150	13.664
49	30.673	646.93	43.100	
5	30.749	646.95	43.100	108.316
8	30.749	646.95	43.100	108.316
18	389.489	281.67	55.604	701.723
Bleed	0.304	856.82	2320.122	

Efficiencies:	isentr	polytr	RNI	P/P
Outer LPC	0.9176	0.9224	0.430	1.530
Inner LPC	0.8991	0.9124	0.430	2.778
HP Compressor	0.8982	0.9309	0.819	22.984
Burner	0.9950			0.953
HP Turbine	0.9270	0.9129	3.003	4.942
LP Turbine	0.9440	0.9251	0.903	10.375

HP Spool mech Eff	1.0000	Nom Spd	14665 rpm
LP Spool mech Eff	1.0000	Nom Spd	2506 rpm

hum [%]	war0	FHV	Fuel
0.0	0.00000	43.124	Generic

FN	=	50.34	kN
TSFC	=	12.4061	g/(kN*s)
WF	=	0.62455	kg/s
BPR	=	12.8000	
s NOx	=	1.1941	
Core Eff	=	0.6167	
Prop Eff	=	0.7987	
P3/P2	=	63.84	
P2/P1	=	1.0000	
P16/P13	=	1.0000	
P25/P21	=	1.0000	
P45/P44	=	1.0000	
P6/P5	=	1.0000	
A8	=	0.46347	m^2
A18	=	2.97864	m^2
P8/Pamb	=	1.80828	
P18/Pamb	=	2.33290	
WBld/W25	=	0.01000	
CD8	=	0.97827	
CD18	=	0.97640	
XM8	=	0.96868	
XM18	=	1.00000	
V18/V8,id	=	0.77276	
Loading	=	100.00	%
e444 th	=	0.91113	
PWX	=	55.29	kW
WCHN/W25	=	0.04000	
WCHR/W25	=	0.03262	
WLcl/W25	=	0.00249	

Composed Values:
1: P16q6 = 1.29012

C.3 GasTurb output at take-off condition (M = 0.1 & h = 0 m)

Station	W kg/s	T K	P kPa	WRstd kg/s
amb		288.15	101.325	
1	977.401	288.73	102.036	
2	977.401	288.73	102.036	971.561
13	906.753	323.65	149.024	653.398
21	70.648	383.97	259.627	31.828
25	70.345	383.97	259.627	31.692
3	70.17	933.74	5578.862	2.294
31	64.358	933.74	5578.862	
4	65.928	1726.5	5311.984	3.078
41	68.742	1696.61	5311.984	3.182
43	68.742	1218.82	1087.942	
44	71.037	1210.18	1087.942	
45	71.037	1210.18	1087.942	13.558
49	71.037	747.06	129.689	
5	71.212	747	129.689	89.581
8	71.212	747	129.689	89.581
18	906.753	323.65	149.024	653.398
Bleed	0.703	933.74	5578.853	

Efficiencies:	isentr	polytr	RNI	P/P
Outer LPC	0.9432	0.9461	1.005	1.461
Inner LPC	0.9242	0.9334	1.005	2.544
HP Compressor	0.908	0.9369	1.82	21.488
Burner	0.999			0.952
HP Turbine	0.9257	0.9117	6.617	4.883
LP Turbine	0.9416	0.9246	1.998	8.389

HP Spool mech Eff	1.0000	Nom Spd	15072 rpm
LP Spool mech Eff	1.0000	Nom Spd	2441 rpm

hum [%]	war0	FHV	Fuel
0.0	0.00000	43.124	Generic

FN	=	225.83	kN
TSFC	=	6.9528	g/(kN*s)
WF	=	1.57017	kg/s
BPR	=	12.8349	
s NOx	=	2.5194	
Core Eff	=	0.5536	
Prop Eff	=	0.2277	
P3/P2	=	1.271	
P2/P1	=	1	
P16/P13	=	1	
P25/P21	=	1	
P45/P44	=	1	
P6/P5	=	1	
A8	=	0.46347	m^2
A18	=	2.97864	m^2
P8/Pamb	=	1.27993	
P18/Pamb	=	1.47076	
WBld/W25	=	0.01	
CD8	=	0.95418	
CD18	=	0.95985	
XM8	=	0.61442	
XM18	=	0.76338	
V18/V8,id	=	0.81345	
Loading	=	36.88	%
e444 th	=	0.90965	
PWX	=	55.29	kW
WCHN/W25	=	0.04	
WCHR/W25	=	0.03262	
WLcl/W25	=	0.00249	

Iteration Variables:
1: Burner Temperature ZT4 (1602...1755) = 1726.5

Iteration Targets:
1: FN Net Thrust = 255.83

C.4 GasTurb output at take-off condition (M = 0.2 & h = 0 m)

Station	W kg/s	T K	P kPa	WRstd kg/s
amb		288.15	101.325	
1	995.906	290.46	104.191	
2	995.906	290.46	104.191	972.385
13	925.428	324.77	151.089	658.880
21	70.479	384.35	261.481	31.542
25	70.479	384.35	261.481	31.542
3	70.303	932.91	5583.925	2.295
31	64.480	932.92	5583.925	
4	66.048	1723.50	5316.512	3.079
41	68.867	1693.67	5316.512	3.182
43	68.867	1216.75	1088.904	
44	71.166	1208.15	1088.904	
45	71.166	1208.15	1088.904	13.560
49	71.166	745.49	129.677	
5	71.342	745.33	129.677	89.658
8	71.342	745.33	129.677	89.658
18	925.428	324.77	151.089	658.880
Bleed	0.705	932.91	5583.916	

Efficiencies:	isentr	polytr	RNI	P/P
Outer LPC	0.9463	0.9490	1.019	1.450
Inner LPC	0.9272	0.9360	1.019	2.510
HP Compressor	0.9082	0.9370	1.831	21.355
Burner	0.9990			0.952
HP Turbine	0.9254	0.9113	6.636	4.882
LP Turbine	0.9416	0.9245	2.004	8.397

HP Spool mech Eff	1.0000	Nom Spd	15034 rpm
LP Spool mech Eff	1.0000	Nom Spd	2436 rpm

hum [%]	war0	FHV	Fuel
0.0	0.00000	43.124	Generic

FN	=	200.64	kN
TSFC	=	7.8147	g/(kN*s)
WF	=	1.56797	kg/s
BPR	=	13.1306	
s NOx	=	2.5097	
Core Eff	=	0.5540	
Prop Eff	=	0.4035	
P3/P2	=	1.2446	
P2/P1	=	1.0000	
P16/P13	=	1.0000	
P25/P21	=	1.0000	
P45/P44	=	1.0000	
P6/P5	=	1.0000	
A8	=	0.46347	m^2
A18	=	2.97864	m^2
P8/Pamb	=	1.27981	
P18/Pamb	=	1.49114	
WBld/W25	=	0.01000	
CD8	=	0.95425	
CD18	=	0.96112	
XM8	=	0.61426	
XM18	=	0.77765	
V18/V8,id	=	0.82950	
Loading	=	36.99	%
e444 th	=	0.90931	
PWX	=	55.29	kW
WCHN/W25	=	0.04000	
WCHR/W25	=	0.03262	
WLcl/W25	=	0.00249	

Iteration Variables:
1: Burner Temperature ZT4 (1602...1755) = 1723.5

Iteration Targets:
1: FN Net Thrust = 200.5

C.5 GasTurb output at take-off condition (M = 0.1 & h = 1655 m)

Station	W kg/s	T K	P kPa	WRstd kg/s
amb		303.25	82.960	
1	720.933	303.85	83.542	
2	720.933	303.85	83.542	897.904
13	671.524	335.93	116.284	631.795
21	49.409	393.35	193.354	30.252
25	49.236	393.35	193.354	30.146
3	49.113	937.42	3902.280	2.300
31	45.046	937.42	3902.280	
4	46.140	1726.50	3714.630	3.081
41	48.110	1696.73	3714.630	3.184
43	48.110	1222.96	766.538	
44	49.716	1214.30	766.538	
45	49.716	1214.30	766.538	13.491
49	49.716	767.08	100.389	
5	49.839	766.98	100.389	82.069
8	49.839	766.98	100.389	82.069
18	671.524	335.94	116.284	631.796
Bleed	0.492	937.42	3902.269	

Efficiencies:	isentr	polytr	RNI	P/P
Outer LPC	0.9352	0.9381	0.774	1.392
Inner LPC	0.9164	0.9256	0.774	2.314
HP Compressor	0.9097	0.9376	1.317	20.182
Burner	0.9984			0.952
HP Turbine	0.9215	0.9069	4.627	4.846
LP Turbine	0.9401	0.9236	1.402	7.636

HP Spool mech Eff	1.0000	Nom Spd	14782 rpm
LP Spool mech Eff	1.0000	Nom Spd	2357 rpm

hum [%]	war0	FHV	Fuel
0.0	0.00000	43.124	Generic

FN	=	156.47	kN
TSFC	=	6.9973	g/(kN*s)
WF	=	1.09490	kg/s
BPR	=	13.5910	
s NOx	=	2.2256	
Core Eff	=	0.5326	
Prop Eff	=	0.2435	
P3/P2	=	1.2017	
P2/P1	=	1.0000	
P16/P13	=	1.0000	
P25/P21	=	1.0000	
P45/P44	=	1.0000	
P6/P5	=	1.0000	
A8	=	0.46347	m^2
A18	=	2.97864	m^2
P8/Pamb	=	1.21009	
P18/Pamb	=	1.40169	
WBld/W25	=	0.01000	
CD8	=	0.94907	
CD18	=	0.95526	
XM8	=	0.53875	
XM18	=	0.71182	
V18/V8,id	=	0.87043	
Loading	=	48.51	%
e444 th	=	0.90547	
PWX	=	55.29	kW
WCHN/W25	=	0.04000	
WCHR/W25	=	0.03262	
WLcl/W25	=	0.00249	

APPENDIX D
NACELLE THRUST AND DRAG COMPONENTS

Table D.1 Thrust and drag forces in cruise

	Thrust forces [N]			Pressure drag [N]			Friction drag [N]							
	F_{G_1}	$F_{G_{19}}$	F_{G_9}	D_{p_p}	$D_{p_{AB}}$	$D_{p_{cowl}}$	D_{inlet}	D_{hub}	D_{fco}	D_{fci}	D_{cco}	D_{cci}	D_p	NPF_{CR}
Initial	102838.2	137124.5	16640	-	-449.8	2823.5	294.8	1115.5	1429.2	227.2	1547.5	98.2	7.7	43832.6
GM1.1	107936.1	137289.7	16005.0	-	-557.3	-6918.0	322.3	1109.8	1576.4	248.5	1368.3	117.5	10.5	48080.6
GM1.2	102424.4	137359.1	16874.6	-	-354.3	2593.5	315.7	1109.1	1400.5	210.4	1632.5	96.5	9.4	44795.8
GM1.3	126585.0	130859.9	18775.5	-	-21206.8	-4731.5	591.8	1015.9	1839.5	844.5	2539.7	104.5	11.5	42041.3
GM2.1	104724.0	153486.8		-	-	-4253.8	301.9	1103.6	1953.6	1044.2	550	10.1	17.7	48035.5
GM2.2	104352.2	153529.5		-	-	-3338.9	294.5	1102.9	2171.7	1055.4	475.8	9.9	21.4	47384.6
GM2.3	122566.1	154898.1		-358.2	-	-11268.4	822	1150.8	1896.8	956.7	449	12.1	21.2	38650.1
GM3.1	105023.8	138095.1	15396.4	-	-1466.3	-3459.5	310.3	1127.5	1599.7	283.6	1140.8	130.6	3.2	48797.9
GM3.2	130700.7	131855.4	18221.7	-	-17888.2	-15272.4	545.4	922.5	1659.2	776.9	2101.6	109.7	4.6	46417
GM3.3	123351.8	132207.4	17509.4	-	-12897.5	-10253.847	588.7	1063.1	1556.2	922.6	1633.5	110.6	2.6	43639.1
GM4.1	101325.8	133548.3	16872.0	-	-9737.4	3269.2	394.9	1122.4	1821.4	908.4	1333.4	97.3	4.2	49880.7
GM4.2	101376.4	133542.6	16873.9	-	-9740.9	3299.4	394.7	1121.1	1816.2	905.5	1344.3	97.3	5.3	49797.1
GM4.3	103002.0	133897.7	17172.8	-	-9251.2	2418.4	267.8	1120.5	1906.2	963.9	1325.3	97	12.9	49207.6

Table D.2 Thrust and drag forces in their respective take-off conditions

	Thrust forces [N]			Pressure drag [N]			Friction drag [N]							
	F_{G_1}	$F_{G_{19}}$	F_{G_9}	D_{p_p}	$D_{p_{AB}}$	$D_{p_{cowl}}$	D_{inlet}	D_{hub}	D_{fco}	D_{fci}	D_{cco}	D_{cci}	D_p	NPF_{TO}
Initial	43197.7	237806.8	29266.9	-	378.8	-7474.6	219.3	2767.7	108.1	495.7	3442.2	206.1	14.0	223718.7
GM1.1	41751.2	238764.6	27522.4	-	193.2	-6447.1	1459.6	1880.5	98.1	554.6	2818.4	239.1	19.3	223720.1
GM1.2	43180.4	239228.4	29639.7	-	562.7	-7410.0	246	3210	107.2	457.4	3602.9	201.4	14.9	224695.2
GM1.3	35710	229882.5	32831.4	-	-16541.4	634.0	1461	1961.2	134.9	1897.8	5671.9	217.6	20.2	231546.7
GM2.1	43181.9	267735.8		-	-	-5681.3	190.5	2390.5	140.3	2305.8	1223.5	19.3	35.1	223930.2
GM2.2	41542.9	267843.4		-	-	-7132.8	146.1	2478.6	147.7	2335.9	1053.8	19	42.9	227209.4
GM2.3	33844.7	270302.5		-364.5	-	165.2	863.6	2479.3	137.0	2138.4	1005.8	23.5	40.5	229969.1
GM3.1	69360	252228.2	26338	-	-852.8	607.5	964	2148.4	316.7	659.8	2344.1	258.6	5.4	202754.6
GM3.2	66901.5	239561	32029.4	-	-13265.4	3148.0	613.2	1779.6	540.2	1766.2	4743.3	227.3	8.6	205091.9
GM3.3	66190.2	242838.6	30647.8	-	-12278.5	3380.4	1494.5	2170.9	547.6	2086.6	3688	227.4	4.7	205974.6
GM4.1	32400.7	167919.0	19024.0	-	-6567.9	-4996.5	1064.3	3179.4	107.2	1431.4	2135.3	136.8	5.2	158047.2
GM4.2	32241.6	167859.7	19028.6	-	-6552.6	-4980.8	1051.6	3158.9	107.0	1425.7	2153.7	136.8	6.6	158139.8
GM4.3	31821.0	168093.2	19381.0	-	-5890.4	-5402.9	143.4	1577.5	107.4	1522.1	2138.9	136.1	16.7	161304.6

Table D.3 Thrust and drag forces of the nacelle geometries for the take-off condition $h = 0m, M = 0.1$

	Thrust forces [N]			Pressure drag [N]			Friction drag [N]							
	F_{G_1}	$F_{G_{19}}$	F_{G_9}	D_{p_p}	$D_{p_{AB}}$	$D_{p_{cowl}}$	D_{inlet}	D_{hub}	D_{fco}	D_{fci}	D_{cco}	D_{cci}	D_p	NPF_{TO}
GM1.1	41751.2	238764.6	27522.4	-	193.2	-6447.1	1459.6	1880.5	98.1	554.6	2818.4	239.1	19.3	223720.1
GM1.2	43180.4	239228.4	29639.7	-	562.7	-7410.0	246	3210	107.2	457.4	3602.9	201.4	14.9	224695.2
GM1.3	35710	229882.5	32831.4	-	-16541.4	634.0	1461	1961.2	134.9	1897.8	5671.9	217.6	20.2	231546.7
GM2.1	43181.9	267735.8		-	-	-5681.3	190.5	2390.5	140.3	2305.8	1223.5	19.3	35.1	223930.2
GM2.2	41542.9	267843.4		-	-	-7132.8	146.1	2478.6	147.7	2335.9	1053.8	19	42.9	227209.4
GM2.3	33844.7	270302.5		-364.5	-	165.2	863.6	2479.3	137.0	2138.4	1005.8	23.5	40.5	229969.1
GM3.1	43008.4	241776.4	26253	-	-476.2	-6958.9	407.9	2379.2	102.6	641.4	2254.5	261.3	5.4	226403.9
GM3.2	35243.3	229536.5	31635.7	-	-11137.8	559.9	1457.6	1659.7	128.8	1713.2	4599.2	230.8	8.8	226708.7
GM3.3	36051.8	232659.5	30341.2	-	-10644.5	-492.6	1590	2078.4	134.5	2026.1	3579.6	230.6	4.8	228441.9
GM4.1	43199.8	235599.3	29154.2	-	-9261.8	-7055.3	309.4	4214.5	127.9	1992.4	2939.3	208.5	7.6	228071.2
GM4.2	42987.3	235527.7	29159.2	-	-9239	-7026.9	308.8	4209.3	127.7	1984.9	2964.1	208.6	9.6	228152.6
GM4.3	42382	235806.5	29622	-	-8320	-7453	188.7	2578.7	127.7	2119.4	2943.1	208	25	230628.9

Table D.4 Thrust and drag forces of the nacelle geometries in case 1 and 3 for the take-off condition $h = 0m, M = 0.2$

	Thrust forces [N]			Pressure drag [N]			Friction drag [N]							
	F_{G_1}	$F_{G_{19}}$	F_{G_9}	D_{p_p}	$D_{p_{AB}}$	$D_{p_{cowl}}$	D_{inlet}	D_{hub}	D_{fco}	D_{fci}	D_{cco}	D_{cci}	D_p	NPF_{TO}
GM1.1	68219.8	249131.2	27652.6	-	-120	1164.4	1480.9	2032.9	310.4	571.1	2925.2	236.5	16	199946.6
GM1.2	71068.3	249788.8	29830	-	201.3	-804.4	259.2	2767.7	323.8	471.1	3730	199.1	17.2	201385.4
GM1.3	66712	239780	33267.9	-	-19067.4	3602.8	1479.6	2051	558.9	1955.2	5841.7	214.2	22.7	209677.3
GM3.1	69360	252228.2	26338	-	-852.8	607.5	964	2148.4	316.7	659.8	2344.1	258.6	5.4	202754.6
GM3.2	66901.5	239561	32029.4	-	-13265.4	3148.0	613.2	1779.6	540.2	1766.2	4743.3	227.3	8.6	205091.9
GM3.3	66190.2	242838.6	30647.8	-	-12278.5	3380.4	1494.5	2170.9	547.6	2086.6	3688	227.4	4.7	205974.6
GM4.1	71230.3	245752.9	29348.5	-	-10360.8	-526.3	241.1	3450.6	412	2053	3028	206.1	7.5	205359.9
GM4.2	71102.8	245680.5	29353.7	-	-10340.6	-516.8	243.1	3449.5	411.2	2045.3	3053.5	206.2	9.5	205370.4
GM4.3	70631.5	246135.2	29871.9	-	-9392.4	-670.2	158	2312.9	413.6	2181.9	3029.8	205.3	24.7	207112

Table D.5 Thrust and drag forces of the nacelle geometries in case 1 and 4 for the take-off condition $h = 1655m, M = 0.1, \Delta T_{s_{ISA}} = 25.86K$

	Thrust forces [N]			Pressure drag [N]			Friction drag [N]							
	F_{G_1}	$F_{G_{19}}$	F_{G_9}	D_{p_p}	$D_{p_{AB}}$	$D_{p_{cowl}}$	D_{inlet}	D_{hub}	D_{fco}	D_{fci}	D_{cco}	D_{cci}	D_p	NPF_{TO}
GM1.1	30868.4	169710.4	17836.3	-	128.7	-4161.7	1112.2	1272.4	80	400.9	2032	155.7	13.1	155645.1
GM1.2	32404.3	170047.1	19358.7	-	401.4	-5326.6	202.5	1961.8	89.2	328.3	2619.4	132	11.9	156581.6
GM1.3	26581.4	163635.6	21773.8	-	-11779.8	657.6	1021.7	1331.3	115.9	1366	4126.2	145.9	15.8	161827.5
GM4.1	32400.7	167919.0	19024.0	-	-6567.9	-4996.5	1064.3	3179.4	107.2	1431.4	2135.3	136.8	5.2	158047.2
GM4.2	32241.6	167859.7	19028.6	-	-6552.6	-4980.8	1051.6	3158.9	107.0	1425.7	2153.7	136.8	6.6	158139.8
GM4.3	31821.0	168093.2	19381.0	-	-5890.4	-5402.9	143.4	1577.5	107.4	1522.1	2138.9	136.1	16.7	161304.6